2023

PHYSICAL, OPTICAL, AND CHEMICAL PROPERTIES OF LIGHT ABSORBING AEROSOLS AND THEIR CLIMATIC IMPACTS

Susan Mathai
Michigan Technological University, smathai@mtu.edu

PHYSICAL, OPTICAL, AND CHEMICAL PROPERTIES OF LIGHT ABSORBING AEROSOLS AND THEIR CLIMATIC IMPACTS

By

Susan Mathai

A DISSERTATION

Submitted in partial fulfillment of the requirements for the degree of

DOCTOR OF PHILOSOPHY

In Atmospheric Sciences

MICHIGAN TECHNOLOGICAL UNIVERSITY

2023

This dissertation has been approved in partial fulfillment of the requirements for the Degree of DOCTOR OF PHILOSOPHY in Atmospheric Sciences.

Department of Physics

Dissertation Advisor: *Dr. Claudio Mazzoleni*

Committee Member: *Dr. Swarup China*

Committee Member: *Dr. Nancy French*

Committee Member: *Dr. Simon Carn*

Committee Member: *Dr. Will Cantrell*

Department Chair: *Dr. Jacek Borysow*

Table of Contents

List of Figures

List of Tables

Author Contribution Statement

This dissertation consists of content that was or will be published in peer reviewed journals. Chapter 2 is based on a manuscript that we plan to submit to the Environmental Science and Technology Journal. Chapter 3 is based on an article published in the Environmental Science and Technology Journal (Mathai et al. 2023). The research article was written by me with inputs from my internship mentor Dr. Swarup China and my advisor Dr. Claudio Mazzoleni as well as several other collaborators at different institutions. I also analyzed the data and interpreted them. The documentation for the permission to use the published material is attached in Appendix section C. Chapter 4 will be revised after getting feedback from co-authors and submitted to a peer reviewed journal.

Acknowledgements

I extend my sincere gratitude to my research advisor, Dr. Claudio Mazzoleni, for his encouragement, support, and guidance. I am grateful for the opportunity to work with him. His encouragement to ask questions and share ideas made our weekly meetings both enjoyable and productive. It was a valuable opportunity to learn instrumentation skills from him that will be beneficial for my career.

I also extend my deepest gratitude to my internship mentor, Dr. Swarup China, for his motivation, support, guidance, and enthusiasm in conducting research. Working with him was a great opportunity, and his guidance helped me acquire various skills. I consider the opportunity to work with him a milestone in my career. I am also grateful to him for involving me in several projects that allowed me to interact with various researchers and gain exposure to ongoing research projects.

I would like to thank my committee members, Dr. Will Cantrell, Dr. Nancy French, Dr. Swarup China, and Dr. Simon Carn, for their time and hard work in helping me complete my dissertation with their valuable inputs.

Special thanks to all the financial support from the Michigan Technological University Physics Department that enabled me to complete my projects on time. I also thank all other institutions that supported the projects, including the Environmental Molecular Sciences Laboratory, Pacific Northwest National Laboratory, Atmospheric System Research, Advanced Light Source, Climate Research Facility, from the US Department of Energy, as well as the pan-European Aerosol, Clouds and Trace Gases Research Infrastructure (ACTRIS).

I also thank my research team at Michigan Tech and Pacific Northwest National Laboratory for the excellent discussions and their helpful attitude. Special thanks to Libor Kovarik from PNNL for helping me with data collection and analysis from the electron energy loss spectroscopy. I'm extremely grateful for the hard work and dedication of all our collaborators who were involved in sample and data collection. Specifically, I would like

to thank Dr. Angela Marinoni and Dr. Silvia Bucci for their timely responses and input to the projects.

I extend my gratitude to all the funds that covered the travel expenses to attend conferences. Special thanks to Dr. Jacek Borysow for funding the travel through the Henes Fellowship. I also thank the Graduate Student Government for the partial funds that helped in covering the travel expenses.

I would like to express my sincere gratitude to Pruthwiraj Santhosh for his love, care, and support through difficult times. His encouragement motivated me to fight through challenging moments. I would also like to thank my parents and brother, who were my pillars of support. Without their care and love, this wouldn’t have been possible. I also thank my friends for cheering me up and celebrating my success. Their presence filled my life with colors.

Abstract

Aerosols are particles suspended in the atmosphere; they are emitted during natural phenomena such as dust storms, wildfires, and volcanic eruptions, and during anthropogenic activities like household wood burning, vehicles operations, and industrial productions, or they can form in the atmosphere from gas to particle partition. Aerosols impact earth's weather and climate by absorbing and scattering the incoming solar and the outgoing earth thermal radiation and interacting with clouds. The optical properties of aerosols evolve as the chemical and physical properties vary during their residence in the atmosphere. In addition, the aerosols' properties strongly depend on the vertical distribution in the atmosphere. Due to the dynamic and heterogenous nature of the aerosol properties, their optical characteristics are still highly uncertain and hence, it is essential to quantify their ability to absorb and scatter light. To address this knowledge gap, we studied atmospheric particles in three different regions of the world with different environmental conditions and particle compositions.

To investigate the details of aerosols as a function of height, we studied how their optical properties vary vertically using a tethered balloon system at the U.S. Department of Energy Atmospheric Radiation Measurement Southern Great Plains site in Oklahoma. We also estimated the top of the atmosphere radiative forcing using Lorentz-Mie simulations and the Santa Barbara Disort Atmospheric Radiative Transfer (SBDART) model. In a second study, we collected aerosol samples at a mountaintop site in Italy to study aerosols transported over long ranges. In the samples, we found an abundance of tar balls which are a kind of particles often detected in biomass-burning plumes (e.g., wildfire smoke). Tar balls absorb light at shorter wavelengths falling within the particle category often referred to as brown carbon; however, the reported complex refractive indices in the literature are highly variable. Therefore, we estimated the refractive index (RI) and optical properties of single tar balls using electron energy loss spectroscopy. We also estimated their radiative forcing to understand their potential impacts on climate and weather systems. In a third study on aerosol processing in haze conditions, we used microscopy and mass spectrometry techniques to observe the abundance of organosulfates formed through multiphase chemical reactions between organic and sulfate particles collected in the Indo-Gangetic

region. The formation of organosulfates was recently shown to increase the light absorption by organic particles in the ultraviolet and visible spectral range. Finally, we classified aerosols based on their chemical composition and phase state which also affect the aerosol optical properties in complex manners.

My thesis discusses the chemical, physical, and optical properties of atmospheric aerosols providing data that can be used in climate and weather models to reduce uncertainties and enhance their predictability skills.

1 Introduction

Aerosols are particles suspended in the atmosphere after being emitted from various natural and anthropogenic sources such as wildfires, industrial activities, sea sprays, or that they form in the atmosphere from gas condensation. They impact climate by altering Earth's radiation balance through absorbing and scattering incident solar as well as outgoing Earth's radiation and by interacting with clouds. The light absorption and scattering by aerosols depend on the mixing state of individual particles and their phase state. This dissertation focuses on the optical (scattering, absorption, etc.) and, physical (phase state) properties, and chemical composition of aerosols collected from three different geographical locations and discusses the impacts on the climate by calculating their radiative forcing.

1.1 Research motivation

The magnitude of light absorption and scattering by aerosols depend on several factors such as chemical composition [1], atmospheric aging due to their residence time in the atmosphere [2], size [3], and shape [4]. Radiative forcing (RF) values are used to quantify the perturbations in the net flux of energy in the climate system due to anthropogenic activities and natural factors. The RF depends on the aerosol properties as well as the albedo of the surface underneath and the presence of clouds. Aerosol properties that affect the RF are (1) single scattering albedo (SSA, the ratio of light scattering to the total extinction equal to scattering plus absorption), (2) the hemispheric upscatter fraction, often approximated with the asymmetry parameter g (that provide a measure of how much light is scattered back to space vs. what is scattered toward Earth), in addition to the vertical distribution of the aerosol concentration [5-8]. Aerosols that mostly absorb light, such as black carbon (BC) emitted from wildfires and household cooking can have a positive RF [9-11] and can warm the climate whereas aerosols that do not absorb or absorb very weakly, such as sulfates have a negative RF [10, 12] and cools the climate. RF values of spherically symmetric aerosols are determined using the size distribution and refractive index. The chemical composition of aerosols determines the water uptake of aerosols which in turn affects the refractive index and their optical properties.

Depending on the source, aerosols have different chemical compositions. For instance, aerosols emitted from wildfires are composed primarily of organic material and, BC or elemental carbon (EC) with small fractions of sulfates, nitrate, ammonium, chlorine, and mineral dust [13] ; whereas sea sprays will generate aerosols rich in sea salt and smaller fractions of biological aerosols [14]. As the particles are transported in the atmosphere they mix and undergo chemical reactions with each other and low-volatility gaseous species changing their chemical composition, physical and optical properties [15, 16]. Although, a major fraction of aerosols is present within the boundary layer, aerosols also reach higher altitudes due to convection [17], topography [18], volcanic eruptions [19], wildfires [20], etc. Large wildfire events can transport aerosol plumes to even higher altitudes into the free troposphere or even to the lower stratosphere by pyroconvection [21-24]. The plumes are transported in the atmosphere for several days (up to two weeks) reaching distant places around the globe and different heights [25, 26].

The vertical variability of aerosols is determined by several environmental factors. In a recent study, Lei et al. 2021 observed four different types of vertical profiles of aerosols over an urban environment: Type 1 showed a uniform distribution of $PM_{2.5}$ with minimal vertical variability associated with strong vertical convection and a relatively large temperature lapse rate, Type 2 had elevated concentration of aerosols at higher altitudes due to temperature inversions and changes in wind direction, Type 3 showed decreasing trends in aerosol concentration with height which occurred during clean periods with high mixed layer height further indicating that convection and dilution are the main drivers of vertical changes, and Type 4 was characterized by a significant drop in the aerosol concentration at specific heights during haze events, often due to cleaning events of aerosols caused by changes in wind direction associated with drop in relative humidity (from 75% to 30%) when different air masses overlapped and formed a strong temperature inversion [27].

Differences in the aerosol composition and concentration with respect to altitude also lead to changes in the optical properties of the aerosol column altering the RF values. In a recent study by Li et al. 2022 [28], they observed an increase in SSA with altitude even though the

scattering coefficient decreased by 17% linearly up to a height of 240 m from the ground. They attributed this trend to an increased fraction of secondary inorganic aerosols at higher altitudes. Similarly in a different profile, they also observed a slight decrease in SSA despite an increase in nitrate concentrations due to a decrease in scattering from sulfate and an increase in absorbing BC and brown carbon (BrC) concentrations [28]. In another study by Sun et al. 2015 [29] , they observed variations in sulfate and nitrate composition between different profiles from the ground up to 260 meters. Interestingly, they observed a rapid decrease in sulfate and nitrate within one hour at 260 m altitude whereas the cleaning process due to change in wind direction at the ground took approximately 3 hours. A strong temperature inversion below 50 m associated with higher relative humidity (RH) and lower wind speed led to the formation of a stable layer below 50 m causing the observed delay in the cleaning of air pollutants at the ground due to change in wind direction [29]. Hence, depending on meteorological parameters and chemical compositions, the optical properties of aerosols are typically different at different altitudes.

In addition to affecting the vertical distribution of aerosols by pyroconvection, wildfires impact climate, visibility, and atmospheric chemistry by emitting large amounts of trace gases and aerosol species [30-32]. Organic aerosols and BC are major constituents emitted during wildfires [33, 34]. A type of light absorbing organic aerosol, commonly referred to as brown carbon (BrC), is also an important contributor to the aerosol RF [35]. Previous studies have shown that including the absorption of BrC in climate models can improve the accuracy of the assessment of aerosol climatic effects [36-38]. On the contrary to purely scattering organic aerosols, the absorption by BrC can induce a warming effect, for example, Fang et al. reported a RF by BrC of 0.11 Wm^{-2} at the top of the atmosphere [39].

One major cause for the uncertainty in determining the impact of BrC is the lack of understanding in the relationship between emission sources and optical properties [40]. The wavelength dependence of the optical parameters of BrC is often approximated by a power law relationship as [41]:

$$MAE = C.\lambda^{-AAE}$$

Where, the mass absorption efficiency (MAE, the ratio of the absorption cross section to the mass of a particle) is measured in cm^2g^{-1}, C is a constant, AAE is absorption Ångström exponent [42, 43]. A previous study by Martinsson et al. 2015 reported that the AAE value for BC emitted from fossil fuel combustion is about 1 which indicates that the wavelength dependence of MAC is weak as compared to that of BrC emitted from incomplete biomass burning which has a wider range for AAE from 1 to 3 [44]. Secondary BrC is produced from aging of BrC due to rapid photobleaching [45, 46]. Photobleaching alters the absorption characteristics of BrC aerosols and has a notable impact on the radiative forcing of the atmosphere [47]. Furthermore, secondary BrC formed from the photo-oxidation of biomass burning emissions has AAE value ranging from 3 to 7 [48] which shows that the AAE value is closely related to the source. The variation in molecular composition of BrC under different burning conditions, are influenced by factors such as combustion temperature, oxygen content, and relative humidity [49], along with the mixing state of secondary BrC and can lead to changes in the amount of radiation absorbed [42, 50, 51].

The phase characteristics of BrC particles vary from low viscosity or liquid like to high viscosity or solid like particles such as tarballs (TBs) [52, 53]. TBs are identified through electron microscopy due to their spherical, amorphous nature with high resistance to the electron beam [54, 55]. TBs are formed during smoldering phase of combustion [54]. Previous research indicates that the proportion of TBs in freshly emitted smoke is approximately 15% increasing to around 80% in aged plumes [56]. The mechanism leading to TBs formation are not well understood, but a recent study revealed that low viscosity organic aerosols transform into TBs within a few hours of emission due to the addition of O- and N-containing compounds such as carboxylic acids and other organonitrate compounds [57]. Moreover, the imaginary part of the refractive index reported from previous studies for TBs ranges from 0.002 at 532 nm [58] to 0.27 at 550 nm [59]. The reported variability of about 10 times in the imaginary RI of TBs impacts the retrieved RF values of TBs at different locations.

When inorganic sulfates are coated by organic shells, the shell can modulate the hygroscopicity of the particles which also significantly impacts their optical properties, RF,

reactivity and lifetime [60]. Solar radiation can also modify the viscosity of the organic aerosol [61] impacting its ability to form cloud condensation nuclei [62] and ice nuclei [63]. The viscosity of organic aerosol determines its growth rate and evaporation [64-66]. Organic aerosols with low viscosity will grow with increase in relative humidity whereas, highly viscous particles will have slow diffusion rates of pollutants [67]. High relative humidity plays a key role in the formation of a type of BrC called organosulfates (OS) [68, 69].

OS are formed through the mixing of biogenic and anthropogenic aerosols through multiphase reactions with organic compounds and acidic sulfate particles [70]. Organic sulfate containing compounds along with inorganic sulfates impact the physicochemical processes that the aerosols undergo in the atmosphere [70-72]. Depending on the organic fraction, it was observed that the errors in estimating the aerosol SSA ranged from 0.6% for higher organic mass fraction (45 to 65%) to 6% for lower organic mass fraction (less than 45%) when assuming a constant hygroscopic parameter [73]. A reason for the impact on the optical properties of organic and inorganic mixed aerosols is phase separation. When there is a core shell morphology, the light scattering at the liquid-liquid boundary leads to changes in the optical properties [74]. Li et al. 2021 reported that in their study particle with equivalent sphere diameter greater than 100 nm have a secondary inorganic aerosol core with organic coating [75]. However, only a few studies have reported phase separation observed in ambient samples [75].

1.2 Research objectives

The objectives of this dissertation are to improve our understanding of the physical, chemical, and optical properties of atmospheric aerosols with a focus on light absorbing aerosols. We will discuss three studies on the physical, chemical, and optical properties of aerosols collected from three different locations. The data such as refractive index, radiative forcing and phase of internally mixed aerosols studied will help to improve climate and weather models. With these goals in mind, here we investigate the following topics:

1. Vertical profiles of absorbing particles measured using a tethered balloon system in the Southern Great Plains site of the Department of Energy Atmospheric

Radiation Measurement (ARM) program. We also link the observed optical parameters with the chemical composition of the samples determined by computer-controlled scanning electron microscopy. Finally, radiative forcing values are estimated to show the effect of chemical composition and physical properties of the aerosols in impacting the climate.

2. Optical properties of a type of highly viscous BrC aerosols known as tar balls that were collected from the free troposphere. In this study we used electron energy loss spectroscopy to estimate the refractive index of tar balls. We also compared the refractive index values from our study to previously reported values and highlight and discuss the effects of the large differences in the reported imaginary refractive index. Using values of refractive indices of tar balls from three different studies in the literature (including ours), we calculate the radiative forcing, we calculate the radiative forcing and highlight the need for further research to accurately estimate the impact of these aerosols on climate.
3. To study the haze processing of aerosols during wintertime in the Indo-Gangetic Plain, we investigate the impact of the mixing of inorganic aerosols with organic material in high humid conditions. We observed phase separation of aerosols during high humidity periods and its impact on the viscosity of aerosols, which is a key parameter to understanding the optical properties of these core-shell mixed particles. We also identified organosulfates and determined their molecular formulae using mass spectrometry.

1.3 References

1. Andreae, M. O.; Schmid, O.; Yang, H.; Chand, D.; Zhen Yu, J.; Zeng, L.-M.; Zhang, Y.-H., Optical properties and chemical composition of the atmospheric aerosol in urban Guangzhou, China. *Atmospheric Environment* **2008,** *42*, (25), 6335-6350.
2. Liu, J.; Lin, P.; Laskin, A.; Laskin, J.; Kathmann, S. M.; Wise, M.; Caylor, R.; Imholt, F.; Selimovic, V.; Shilling, J. E., Optical properties and aging of light-absorbing secondary organic aerosol. *Atmos. Chem. Phys.* **2016,** *16*, (19), 12815-12827.
3. Ysard, N.; Jones, A.; Demyk, K.; Boutéraon, T.; Koehler, M., The optical properties of dust: the effects of composition, size, and structure. *Astronomy & Astrophysics* **2018,** *617*, A124.
4. Mishra, S. K.; Tripathi, S., Modeling optical properties of mineral dust over the Indian Desert. *Journal of Geophysical Research: Atmospheres* **2008,** *113*, (D23).

5. Chylek, P.; Wong, J., Effect of absorbing aerosols on global radiation budget. *Geophysical Research Letters* **1995,** *22*, (8), 929-931.
6. Haywood, J.; Boucher, O., Estimates of the direct and indirect radiative forcing due to tropospheric aerosols: A review. *Reviews of geophysics* **2000,** *38*, (4), 513-543.
7. Lenoble, J.; Tanre, D.; Deschamps, P. Y.; Herman, M., A simple method to compute the change in earth-atmosphere radiative balance due to a stratospheric aerosol layer. *Journal of the Atmospheric Sciences* **1982,** *39*, (11), 2565-2576.
8. Hassan, T.; Moosmüller, H.; Chung, C. E., Coefficients of an analytical aerosol forcing equation determined with a Monte-Carlo radiation model. *Journal of Quantitative Spectroscopy and Radiative Transfer* **2015,** *164*, 129-136.
9. Haywood, J. M.; Shine, K. P., The effect of anthropogenic sulfate and soot aerosol on the clear sky planetary radiation budget. *Geophysical Research Letters* **1995,** *22*, (5), 603-606.
10. Haywood, J. M.; Ramaswamy, V., Global sensitivity studies of the direct radiative forcing due to anthropogenic sulfate and black carbon aerosols. **1998,** *103*, (D6), 6043-6058.
11. Chung, S. H.; Seinfeld, J. H., Global distribution and climate forcing of carbonaceous aerosols. *Journal of Geophysical Research: Atmospheres* **2002,** *107*, (D19), AAC 14-1-AAC 14-33.
12. Kim, D.; Wang, C.; Ekman, A. M. L.; Barth, M. C.; Rasch, P. J., Distribution and direct radiative forcing of carbonaceous and sulfate aerosols in an interactive size-resolving aerosol–climate model. *Journal of Geophysical Research: Atmospheres* **2008,** *113*, (D16).
13. Garofalo, L. A.; Pothier, M. A.; Levin, E. J. T.; Campos, T.; Kreidenweis, S. M.; Farmer, D. K., Emission and Evolution of Submicron Organic Aerosol in Smoke from Wildfires in the Western United States. *ACS Earth and Space Chemistry* **2019,** *3*, (7), 1237-1247.
14. Quinn, P. K.; Collins, D. B.; Grassian, V. H.; Prather, K. A.; Bates, T. S., Chemistry and Related Properties of Freshly Emitted Sea Spray Aerosol. *Chemical Reviews* **2015,** *115*, (10), 4383-4399.
15. Aggarwal, S. G.; Kawamura, K., Carbonaceous and inorganic composition in long-range transported aerosols over northern Japan: Implication for aging of water-soluble organic fraction. *Atmospheric Environment* **2009,** *43*, (16), 2532-2540.
16. Song, C. H.; Carmichael, G. R., The aging process of naturally emitted aerosol (sea-salt and mineral aerosol) during long range transport. *Atmospheric Environment* **1999,** *33*, (14), 2203-2218.
17. Tsai, R., Aerosol particle transport in a natural convection flow onto a vertical flat plate. *International Journal of Heat and Mass Transfer* **2001,** *44*, (4), 867-870.
18. Collaud Coen, M.; Andrews, E.; Aliaga, D.; Andrade, M.; Angelov, H.; Bukowiecki, N.; Ealo, M.; Fialho, P.; Flentje, H.; Hallar, A. G.; Hooda, R.; Kalapov, I.; Krejci, R.; Lin, N. H.; Marinoni, A.; Ming, J.; Nguyen, N. A.; Pandolfi, M.; Pont, V.; Ries, L.; Rodríguez, S.; Schauer, G.; Sellegri, K.; Sharma, S.; Sun, J.; Tunved, P.; Velasquez, P.; Ruffieux, D., Identification of topographic features influencing aerosol observations at high altitude stations. *Atmos. Chem. Phys.* **2018,** *18*, (16), 12289-12313.

19. Vernier, J.-P.; Thomason, L. W.; Pommereau, J.-P.; Bourassa, A.; Pelon, J.; Garnier, A.; Hauchecorne, A.; Blanot, L.; Trepte, C.; Degenstein, D.; Vargas, F., Major influence of tropical volcanic eruptions on the stratospheric aerosol layer during the last decade. *Geophysical Research Letters* **2011,** *38*, (12).
20. Chen, Y.; Li, Q.; Randerson, J. T.; Lyons, E. A.; Kahn, R. A.; Nelson, D. L.; Diner, D. J., The sensitivity of CO and aerosol transport to the temporal and vertical distribution of North American boreal fire emissions. *Atmos. Chem. Phys.* **2009,** *9*, (17), 6559-6580.
21. Fromm, M.; Alfred, J.; Hoppel, K.; Hornstein, J.; Bevilacqua, R.; Shettle, E.; Servranckx, R.; Li, Z.; Stocks, B., Observations of boreal forest fire smoke in the stratosphere by POAM III, SAGE II, and lidar in 1998. *Geophysical Research Letters* **2000,** *27*, (9), 1407-1410.
22. Fromm, M.; Bevilacqua, R.; Servranckx, R.; Rosen, J.; Thayer, J. P.; Herman, J.; Larko, D., Pyro-cumulonimbus injection of smoke to the stratosphere: Observations and impact of a super blowup in northwestern Canada on 3–4 August 1998. *Journal of Geophysical Research: Atmospheres* **2005,** *110*, (D8).
23. Jost, H. J.; Drdla, K.; Stohl, A.; Pfister, L.; Loewenstein, M.; Lopez, J. P.; Hudson, P. K.; Murphy, D. M.; Cziczo, D. J.; Fromm, M., In-situ observations of mid-latitude forest fire plumes deep in the stratosphere. *Geophysical Research Letters* **2004,** *31*, (11).
24. Petzold, A.; Weinzierl, B.; Huntrieser, H.; Stohl, A.; Real, E.; Cozic, J.; Fiebig, M.; Hendricks, J.; Lauer, A.; Law, K.; Roiger, A.; Schlager, H.; Weingartner, E., Perturbation of the European free troposphere aerosol by North American forest fire plumes during the ICARTT-ITOP experiment in summer 2004. *Atmos. Chem. Phys.* **2007,** *7*, (19), 5105-5127.
25. Schum, S. K.; Zhang, B.; Džepina, K.; Fialho, P.; Mazzoleni, C.; Mazzoleni, L. R., Molecular and physical characteristics of aerosol at a remote free troposphere site: implications for atmospheric aging. *Atmos. Chem. Phys.* **2018,** *18*, (19), 14017-14036.
26. Müller, D.; Mattis, I.; Ansmann, A.; Wandinger, U.; Ritter, C.; Kaiser, D., Multiwavelength Raman lidar observations of particle growth during long-range transport of forest-fire smoke in the free troposphere. *Geophysical Research Letters* **2007,** *34*, (5).
27. Lei, L.; Sun, Y.; Ouyang, B.; Qiu, Y.; Xie, C.; Tang, G.; Zhou, W.; He, Y.; Wang, Q.; Cheng, X.; Fu, P.; Wang, Z., Vertical Distributions of Primary and Secondary Aerosols in Urban Boundary Layer: Insights into Sources, Chemistry, and Interaction with Meteorology. *Environmental Science & Technology* **2021,** *55*, (8), 4542-4552.
28. Li, Y.; Du, A.; Lei, L.; Sun, J.; Li, Z.; Zhang, Z.; Wang, Q.; Tang, G.; Song, S.; Wang, Z.; Wang, Z.; Sun, Y., Vertically Resolved Aerosol Chemistry in the Low Boundary Layer of Beijing in Summer. *Environmental Science & Technology* **2022,** *56*, (13), 9312-9324.
29. Sun, Y.; Du, W.; Wang, Q.; Zhang, Q.; Chen, C.; Chen, Y.; Chen, Z.; Fu, P.; Wang, Z.; Gao, Z.; Worsnop, D. R., Real-Time Characterization of Aerosol Particle Composition above the Urban Canopy in Beijing: Insights into the Interactions between the Atmospheric Boundary Layer and Aerosol Chemistry. *Environmental Science & Technology* **2015,** *49*, (19), 11340-11347.

30. Andreae, M. O.; Merlet, P., Emission of trace gases and aerosols from biomass burning. *Global biogeochemical cycles* **2001,** *15*, (4), 955-966.
31. Yokelson, R. J.; Urbanski, S.; Atlas, E.; Toohey, D.; Alvarado, E. C.; Crounse, J.; Wennberg, P.; Fisher, M.; Wold, C.; Campos, T., Emissions from forest fires near Mexico City. *Atmospheric Chemistry and Physics* **2007,** *7*, (21), 5569-5584.
32. Alves, C.; Vicente, A.; Nunes, T.; Gonçalves, C.; Fernandes, A. P.; Mirante, F.; Tarelho, L.; Sánchez de la Campa, A. M.; Querol, X.; Caseiro, A.; Monteiro, C.; Evtyugina, M.; Pio, C., Summer 2009 wildfires in Portugal: Emission of trace gases and aerosol composition. *Atmospheric Environment* **2011,** *45*, (3), 641-649.
33. Bond, T. C.; Doherty, S. J.; Fahey, D. W.; Forster, P. M.; Berntsen, T.; DeAngelo, B. J.; Flanner, M. G.; Ghan, S.; Kärcher, B.; Koch, D.; Kinne, S.; Kondo, Y.; Quinn, P. K.; Sarofim, M. C.; Schultz, M. G.; Schulz, M.; Venkataraman, C.; Zhang, H.; Zhang, S.; Bellouin, N.; Guttikunda, S. K.; Hopke, P. K.; Jacobson, M. Z.; Kaiser, J. W.; Klimont, Z.; Lohmann, U.; Schwarz, J. P.; Shindell, D.; Storelvmo, T.; Warren, S. G.; Zender, C. S., Bounding the role of black carbon in the climate system: A scientific assessment. **2013,** *118*, (11), 5380-5552.
34. Sedlacek III, A. J.; Buseck, P. R.; Adachi, K.; Onasch, T. B.; Springston, S. R.; Kleinman, L., Formation and evolution of tar balls from northwestern US wildfires. *Atmospheric Chemistry and Physics* **2018,** *18*, (15), 11289-11301.
35. Li, C.; He, Q.; Hettiyadura, A. P. S.; Käfer, U.; Shmul, G.; Meidan, D.; Zimmermann, R.; Brown, S. S.; George, C.; Laskin, A.; Rudich, Y., Formation of Secondary Brown Carbon in Biomass Burning Aerosol Proxies through NO3 Radical Reactions. *Environmental Science & Technology* **2020,** *54*, (3), 1395-1405.
36. Chung, C. E.; Ramanathan, V.; Decremer, D., Observationally constrained estimates of carbonaceous aerosol radiative forcing. *Proceedings of the National Academy of Sciences* **2012,** *109*, (29), 11624-11629.
37. Hammer, M. S.; Martin, R. V.; van Donkelaar, A.; Buchard, V.; Torres, O.; Ridley, D. A.; Spurr, R. J. D., Interpreting the ultraviolet aerosol index observed with the OMI satellite instrument to understand absorption by organic aerosols: implications for atmospheric oxidation and direct radiative effects. *Atmos. Chem. Phys.* **2016,** *16*, (4), 2507-2523.
38. DeLessio, M. A.; Tsigaridis, K.; Bauer, S. E.; Chowdhary, J.; Schuster, G. L., Modeling atmospheric brown carbon in the GISS ModelE Earth system model. *EGUsphere* **2023,** *2023*, 1-50.
39. Feng, Y.; Ramanathan, V.; Kotamarthi, V. R., Brown carbon: a significant atmospheric absorber of solar radiation? *Atmos. Chem. Phys.* **2013,** *13*, (17), 8607-8621.
40. Yan, J.; Wang, X.; Gong, P.; Wang, C.; Cong, Z., Review of brown carbon aerosols: Recent progress and perspectives. *Science of The Total Environment* **2018,** *634*, 1475-1485.
41. Yuan, J. F.; Huang, X. F.; Cao, L. M.; Cui, J.; Zhu, Q.; Huang, C. N.; Lan, Z. J.; He, L. Y., Light absorption of brown carbon aerosol in the PRD region of China. *Atmos. Chem. Phys.* **2016,** *16*, (3), 1433-1443.
42. Bond, T. C.; Bergstrom, R. W., Light Absorption by Carbonaceous Particles: An Investigative Review. *Aerosol Science and Technology* **2006,** *40*, (1), 27-67.

43. Lack, D. A.; Langridge, J. M., On the attribution of black and brown carbon light absorption using the Ångström exponent. *Atmos. Chem. Phys.* **2013,** *13*, (20), 10535-10543.
44. Martinsson, J.; Eriksson, A. C.; Nielsen, I. E.; Malmborg, V. B.; Ahlberg, E.; Andersen, C.; Lindgren, R.; Nyström, R.; Nordin, E. Z.; Brune, W. H.; Svenningsson, B.; Swietlicki, E.; Boman, C.; Pagels, J. H., Impacts of Combustion Conditions and Photochemical Processing on the Light Absorption of Biomass Combustion Aerosol. *Environmental Science & Technology* **2015,** *49*, (24), 14663-14671.
45. Zhao, R.; Lee, A. K. Y.; Huang, L.; Li, X.; Yang, F.; Abbatt, J. P. D., Photochemical processing of aqueous atmospheric brown carbon. *Atmos. Chem. Phys.* **2015,** *15*, (11), 6087-6100.
46. Wong, J. P. S.; Nenes, A.; Weber, R. J., Changes in Light Absorptivity of Molecular Weight Separated Brown Carbon Due to Photolytic Aging. *Environmental Science & Technology* **2017,** *51*, (15), 8414-8421.
47. Lee, H. J.; Aiona, P. K.; Laskin, A.; Laskin, J.; Nizkorodov, S. A., Effect of Solar Radiation on the Optical Properties and Molecular Composition of Laboratory Proxies of Atmospheric Brown Carbon. *Environmental Science & Technology* **2014,** *48*, (17), 10217-10226.
48. Shen, Z.; Zhang, Q.; Cao, J.; Zhang, L.; Lei, Y.; Huang, Y.; Huang, R. J.; Gao, J.; Zhao, Z.; Zhu, C.; Yin, X.; Zheng, C.; Xu, H.; Liu, S., Optical properties and possible sources of brown carbon in PM2.5 over Xi'an, China. *Atmospheric Environment* **2017,** *150*, 322-330.
49. Bond, T. C., Spectral dependence of visible light absorption by carbonaceous particles emitted from coal combustion. **2001,** *28*, (21), 4075-4078.
50. Lack, D. A.; Langridge, J. M.; Bahreini, R.; Cappa, C. D.; Middlebrook, A. M.; Schwarz, J. P., Brown carbon and internal mixing in biomass burning particles. *Proceedings of the National Academy of Sciences* **2012,** *109*, (37), 14802-14807.
51. Zhong, M.; Jang, M., Dynamic light absorption of biomass-burning organic carbon photochemically aged under natural sunlight. *Atmos. Chem. Phys.* **2014,** *14*, (3), 1517-1525.
52. Zobrist, B.; Marcolli, C.; Pedernera, D. A.; Koop, T., Do atmospheric aerosols form glasses? *Atmos. Chem. Phys.* **2008,** *8*, (17), 5221-5244.
53. Virtanen, A.; Joutsensaari, J.; Koop, T.; Kannosto, J.; Yli-Pirilä, P.; Leskinen, J.; Mäkelä, J. M.; Holopainen, J. K.; Pöschl, U.; Kulmala, M., An amorphous solid state of biogenic secondary organic aerosol particles. *Nature* **2010,** *467*, (7317), 824-827.
54. Tóth, A.; Hoffer, A.; Nyirő-Kósa, I.; Pósfai, M.; Gelencsér, A., Atmospheric tar balls: aged primary droplets from biomass burning? *Atmos. Chem. Phys.* **2014,** *14*, (13), 6669-6675.
55. Pósfai, M.; Gelencsér, A.; Simonics, R.; Arató, K.; Li, J.; Hobbs, P. V.; Buseck, P. R., Atmospheric tar balls: Particles from biomass and biofuel burning. *Journal of Geophysical Research: Atmospheres* **2004,** *109*, (D6).
56. China, S.; Mazzoleni, C.; Gorkowski, K.; Aiken, A. C.; Dubey, M. K., Morphology and mixing state of individual freshly emitted wildfire carbonaceous particles. *Nature Communications* **2013,** *4*.

57. Adachi, K.; Sedlacek, A. J.; Kleinman, L.; Springston, S. R.; Wang, J.; Chand, D.; Hubbe, J. M.; Shilling, J. E.; Onasch, T. B.; Kinase, T.; Sakata, K.; Takahashi, Y.; Buseck, P. R., Spherical tarball particles form through rapid chemical and physical changes of organic matter in biomass-burning smoke. *Proceedings of the National Academy of Sciences* **2019,** *116*, (39), 19336-19341.
58. Chakrabarty, R. K.; Moosmüller, H.; Chen, L. W. A.; Lewis, K.; Arnott, W. P.; Mazzoleni, C.; Dubey, M. K.; Wold, C. E.; Hao, W. M.; Kreidenweis, S. M., Brown carbon in tar balls from smoldering biomass combustion. *Atmos. Chem. Phys.* **2010,** *10*, (13), 6363-6370.
59. Alexander, D. T. L.; Crozier, P. A.; Anderson, J. R., Brown Carbon Spheres in East Asian Outflow and Their Optical Properties. *Science* **2008,** *321*, (5890), 833-836.
60. Li, W.; Teng, X.; Chen, X.; Liu, L.; Xu, L.; Zhang, J.; Wang, Y.; Zhang, Y.; Shi, Z., Organic Coating Reduces Hygroscopic Growth of Phase-Separated Aerosol Particles. *Environmental Science & Technology* **2021,** *55*, (24), 16339-16346.
61. Baboomian, V. J.; Crescenzo, G. V.; Huang, Y.; Mahrt, F.; Shiraiwa, M.; Bertram, A. K.; Nizkorodov, S. A., Sunlight can convert atmospheric aerosols into a glassy solid state and modify their environmental impacts. *Proceedings of the National Academy of Sciences of the United States of America* **2022,** *119*.
62. Zaveri, R. A.; Wang, J.; Fan, J.; Zhang, Y.; Shilling, J. E.; Zelenyuk, A.; Mei, F.; Newsom, R.; Pekour, M.; Tomlinson, J., Rapid growth of anthropogenic organic nanoparticles greatly alters cloud life cycle in the Amazon rainforest. *Science Advances* **2022,** *8*, (2), eabj0329.
63. Wolf, M. J.; Zhang, Y.; Zawadowicz, M. A.; Goodell, M.; Froyd, K.; Freney, E.; Sellegri, K.; Rösch, M.; Cui, T.; Winter, M., A biogenic secondary organic aerosol source of cirrus ice nucleating particles. *Nature communications* **2020,** *11*, (1), 4834.
64. Maclean, A. M.; Butenhoff, C. L.; Grayson, J. W.; Barsanti, K.; Jimenez, J. L.; Bertram, A. K., Mixing times of organic molecules within secondary organic aerosol particles: a global planetary boundary layer perspective. *Atmospheric Chemistry and Physics* **2017,** *17*, (21), 13037-13048.
65. Shiraiwa, M.; Li, Y.; Tsimpidi, A. P.; Karydis, V. A.; Berkemeier, T.; Pandis, S. N.; Lelieveld, J.; Koop, T.; Pöschl, U., Global distribution of particle phase state in atmospheric secondary organic aerosols. *Nature communications* **2017,** *8*, (1), 15002.
66. Liu, P.; Li, Y. J.; Wang, Y.; Gilles, M. K.; Zaveri, R. A.; Bertram, A. K.; Martin, S. T., Lability of secondary organic particulate matter. *Proceedings of the National Academy of Sciences* **2016,** *113*, (45), 12643-12648.
67. Shiraiwa, M.; Zuend, A.; Bertram, A. K.; Seinfeld, J. H., Gas–particle partitioning of atmospheric aerosols: interplay of physical state, non-ideal mixing and morphology. *Physical Chemistry Chemical Physics* **2013,** *15*, (27), 11441-11453.
68. McNeill, V. F.; Woo, J. L.; Kim, D. D.; Schwier, A. N.; Wannell, N. J.; Sumner, A. J.; Barakat, J. M., Aqueous-phase secondary organic aerosol and organosulfate formation in atmospheric aerosols: a modeling study. *Environmental science & technology* **2012,** *46*, (15), 8075-8081.
69. McNeill, V. F., Aqueous organic chemistry in the atmosphere: Sources and chemical processing of organic aerosols. In ACS Publications: 2015.

70. Brüggemann, M.; Xu, R.; Tilgner, A.; Kwong, K. C.; Mutzel, A.; Poon, H. Y.; Otto, T.; Schaefer, T.; Poulain, L.; Chan, M. N., Organosulfates in ambient aerosol: state of knowledge and future research directions on formation, abundance, fate, and importance. *Environmental Science & Technology* **2020,** *54*, (7), 3767-3782.
71. Shakya, K. M.; Peltier, R. E., Investigating missing sources of sulfur at Fairbanks, Alaska. *Environmental science & technology* **2013,** *47*, (16), 9332-9338.
72. Shakya, K. M.; Peltier, R. E., Non-sulfate sulfur in fine aerosols across the United States: Insight for organosulfate prevalence. *Atmospheric Environment* **2015,** *100*, 159-166.
73. Nandy, L.; Yao, Y.; Zheng, Z.; Riemer, N., Water uptake and optical properties of mixed organic-inorganic particles. *Aerosol Science and Technology* **2021,** *55*, (12), 1398-1413.
74. Price, C. L.; Preston, T. C.; Davies, J. F., Hygroscopic Growth, Phase Morphology, and Optical Properties of Model Aqueous Brown Carbon Aerosol. *Environmental Science & Technology* **2022,** *56*, (7), 3941-3951.
75. Li, W.; Liu, L.; Zhang, J.; Xu, L.; Wang, Y.; Sun, Y.; Shi, Z., Microscopic Evidence for Phase Separation of Organic Species and Inorganic Salts in Fine Ambient Aerosol Particles. *Environmental Science & Technology* **2021,** *55*, (4), 2234-2242.

2 Vertical Profiles of Absorbing Aerosols Containing Particles Collected from the Southern Great Plains ARM Site

2.1 Abstract

Absorbing aerosols such as black carbon (BC) affect climate directly by efficiently absorbing solar radiation and indirectly by serving as cloud [1] and ice nuclei [2] as well as by altering surface albedo [3]. However, the light-absorption properties are highly variable with respect to altitude due to changes in concentrations, physiochemical properties, morphology, and mixing state, leading to large uncertainties in radiative forcing calculations [4]. In this study, we focus on the analysis of the vertical distribution of absorbing aerosols including their single particle mixing state using measurements and samples collected at the Atmospheric Radiation Measurement (ARM) Southern Great Plains (SGP) site [5]. Data and samples were collected during February and April 2022 by deploying instruments onboard an ARM tethered balloon system (TBS). On the TBS, we deployed a micro-aethalometer (MA200) to monitor the BC concentration at different altitudes, a condensation particle counter (CPC) for total particle concentration measurement, and a Portable Optical Particle Spectrometer (POPS, Handix scientific) to monitor the size distribution of the particles. We also deployed an automated Size and Time-resolved Aerosol Collector (STAC) to collect particles at different altitudes. Single particle measurements using multi-modal microscopy and spectroscopy techniques showed abundance of carbonaceous and sulfate particles during different events. We used the size distribution and particle concentration measurements from POPS and CPC and the MA200 to estimate the scattering and absorption coefficients at different altitudes. Then we calculated the top of the atmosphere radiative forcing using the Santa Barbara DISORT Atmospheric Radiative Transfer (SBDART) model [6]. This study improves our understanding of the mixing states at different altitudes of absorbing aerosols and their radiative forcing.

2.2 Introduction

Aerosols absorb and scatter incoming solar radiation affecting climate by warming or cooling the atmosphere [7, 8]. Aerosols that could contribute towards warming such as black carbon, dust, and brown carbon have a positive radiative forcing (RF) whereas sulfates, a few types of organics etc. contribute towards cooling the atmosphere and have a negative RF [9]. The warming and cooling effects of aerosols impact the thermal structure of the atmosphere and regional circulation systems [7].

Among other factors, the vertical distribution of the aerosol properties determines the net warming and cooling effect. In addition, the vertical variability of physical, chemical, and optical properties of aerosols is still poorly known which humper our understanding of their complex climate effects [10]. In addition, the vertical distribution of aerosols impact turbulence, convection and clouds by changing the stability and thermal structure of the atmosphere, which also affect regional climate and precipitation [11, 12]. . Liu et al. 2019, showed large variations in the sulfate to nitrate ratio and secondary organic aerosol to primary organic aerosol ratio with respect to altitude in China [13]. The radiative forcing of sulfate aerosols reported in the fifth assessment report of the IPCC ranges from -0.6 Wm^{-2} to -0.2 Wm^{-2} [14]. Whereas, for organic aerosols it ranges from -0.27 Wm^{-2} to 0.2 Wm^{-2}. Whereas, for organic aerosols it ranges from -0.27 Wm^{-2} to 0.2 Wm^{-2}. The uncertainty in the radiative forcing of these aerosols are due to limited knowledge in total atmospheric concentration, vertical distribution of the aerosol properties, and the treatment of relative humidity effects [15]. Hence, vertical measurements are essential to study the effect of aerosols on the climate [16, 17].

Different methods can be used to measure vertical profiles of atmospheric properties, including tethered balloons [18], unmanned aerial vehicles [16], lidars [19], aircrafts [20], towers [21], and sunphotometers [22]. Tethered balloon systems allow for continuous long-term measurements of physical, chemical, and optical properties of aerosols [23] ; however, payload limitations only allows for compact light weight instruments such as condensation particle counters, optical particle spectrometers, and microaethalometers [18].

We deployed a tethered balloon system (TBS) at the ARM Southern Great Plains site in Oklahoma. Here we present an analysis of data from three days. On the TBS we flew a CPC for total particle concentrations, a POPS to measure the particle size distribution, two aethalometers to measure the absorption coefficient, and a STAC to collect aerosol samples at different altitudes.

Due to payload constraints, there were no direct scattering measurements on board the TBS. Several previous TBS studies estimated scattering by applying Lorenz-Mie theory using the size distribution from an optical particle sizer while assuming negligible absorption [24-27]. However, Liu et al. 2000 showed that using the refractive index (RI) of latex spheres, that are typically used for optical particle sizers calibration, results in inaccurate size distribution measurements due to the fact that the latex spheres RI is higher than the RI of typical ambient aerosols [28]. To correct this issue, Liu et al. 2000 developed an algorithm by using a lower real part of the RI than that of PSL spheres to match the real RI of ambient samples [28]. In our study, we took an alternative approach, we used the real part of the RI of PSL (used for the instrument calibration) but employed the absorption coefficient measured by the microaethalometer to estimate a non-zero imaginary RI compensating for the underestimation of the size distribution due to absorption. Hence, using Lorenz-Mie theory and the estimated complex RI, we calculated the vertical distribution of optical properties such as the aerosol optical depth (AOD), the single scattering albedo (SSA), and the asymmetry factor (g). Then we used these parameters to calculate the top of the atmosphere RF (TOA RF) using SBDART.

2.3 Experimental Section and Methods

2.3.1 Sampling method

A TBS was used for sampling the vertical profile of aerosols at the ARM SGP site. The TBS consists of a balloon filled with helium, a tether, a winch system, and sensors/samplers [29]. The ARM SGP site has three facilities: the central facility (C1, 36.607 °N and 97.487 °W), and multiple extended facilities such as E13 (36.604 °N and 97.485°W) and E14 (36.605 °N and 97.487°W) that cover a 160 acres with cattle pasture and wheat fields [30]. For this study the TBS was operated at the central facility (C1). During each deployment,

the TBS ascends with the payload to reach certain altitudes of interest (below ~2000 m); then, at the end, it descends to the surface. The maximum payload weight that the TBS can handle varies from 10 to 25 Kg [30]. Samples were collected for three days: 25 February 2022, 18 April 2022, and 16 October 2022.

2.3.2 Instrumentation

The TBS carries a set of meteorological sensors such as InterMet iMet -1-RSB radiosondes, used to measure pressure in the range 2 to 1070 hPa with a resolution less than 0.01 and accuracy of ± 0.5, temperature in the range -95°C to 50°C with a resolution and accuracy of less than 0.01°C and ±0.2 °C respectively, relative humidity with a resolution less than 0.1% and accuracy ±5%, GPS altitude above mean sea level in the range from 0 to more than 30 km with an accuracy of ±15 meters, GPS wind velocity (m/s) with an accuracy of ± 1 m/s and GPS position (m) with an accuracy of ± 10 m [29]. The total particle concentrations were measured with a condensation particle counter (CPC – TSI model 3007) with a minimum size of 10 nm at a flow rate of 1.0 lpm over a concentration range from 0 to 10^4 #/cc [31] with an uncertainty of ± 20%. The size distribution of particles larger than 140 nm was measured using a 3D printed Handix portable optical particle spectrometer (POPS) that uses a laser with a wavelength of 405 nm to detect particles from 140 nm to 3.0 μm in optical diameter with a maximum particle concentration of 1250 #/cc [29]. POPS determines the size of a particle by measuring the scattering intensity for a collection angle of 38° to 142° [32]. The uncertainty in the estimation of size distribution by POPS is ±10% for a concentration of less than 1000 #/cc [32]. The light absorbing aerosol mass concentrations were measured with a filter-based microaethalometer (microAeth MA200) operating in single spot mode. The instrument was operating at 5 different wavelengths (880 nm, 625nm, 528nm, 470nm and 375nm). MA200 is equipped with miniature cartridges with 15 sampling locations that have PTFE filter material for collecting a 3 mm sample spot. The instrument advances the filter automatically when required by a fixed transmission threshold [33]. Aerosol samples were collected using a lightweight (7.5 kg) size and time resolved aerosol collector (STAC) platform loaded with an array of 4-stage cascade impactors. Particles were collected on different substrates (Ex: carbon B-films, carbon lacey and silicon nitride) for multi modal offline analysis to study

the particles' chemical composition, phase, mixing state, and morphology. The STAC platform pulls the sample using a 3 LPM pump and controls solenoid latched valves using a single board computer (Model X86 II ULTRA, UDOO) with an Arduino Leonardo powered by a 76 W h, 21.8 V Li-ion battery [23].

For our analysis, we also used ground-based measurements. Instruments used at the ground a TSI model 3653 nephelometer that measures scattering at three wavelengths: 450 nm, 500 nm, and 700 nm [34].The relative humidity inside the nephelometer was set to 40% to maintain a dry condition and avoid hygroscopic growth [35]. The absorption coefficient was measured at three wavelengths (470 nm, 528 nm, and 660 nm) using a Radiance Research particle soot absorption photometer after calibrating and quality control process using the method developed by Anderson et al. (1999) [36].

2.3.3 Aethalometer correction

The BC mass concentration (m_{BC}) by the MA200 when operated in single spot mode is calculated by the MA200 software using the following equation:

$$m_{BC} = \frac{\partial ATN}{\partial t} \times \frac{A}{V} \times \frac{1}{MAC_{BC,Aeth}} \qquad (1)$$

Where the attenuation (ATN) is the optical attenuation due to aerosol deposited on the sample spot which is measured using a reference portion of the filter with no aerosols. $\frac{\partial ATN}{\partial t}$ = ATN (t) – ATN (t - Δt) is the change of ATN for a time Δt. A is the area of the spot (7.07×10^{-6} m^2) and V is the total volume of aerosol that passes through the filter during each collection time calculated as: flow rate (set at 150 ml/min) times the collection time. $MAC_{BC,Aeth}$ is the mass absorption cross section (Table 2-1). The absorption coefficient b_{abs} is calculated as:

$$b_{abs} = \frac{m_{BC} \times MAC_{BC,Aeth}}{C} \qquad (2)$$

Where C is a correction factor accounting for the optical enhancement due to multiple scattering on the filter. For C, we used a constant value of 2.98 ± 0.05 [37, 38]. The total uncertainty reported by previous studies for an aethalometer due to increasing filter

loading, sample flow rate, filter spot area and detector response is 10% [39-41]. Hence, we propagate the uncertainty in the absorption calculation.

Table 2-1: Mass absorption cross section values for different wavelengths [42]

Color	Wavelength (nm)	$MAC_{BC, Aeth}$ (m^2/g)
IR	880	10.1
Red	625	14.9
Green	528	17.0
Blue	470	19.1
UV	375	24.1

An optimized noise reduction averaging (ONA) was done to reduce the erroneous estimation of BC concentration by extending the effective sampling time so that there is sufficient ATN. We used the ONA noise reduction algorithm tool that is available at the Aethlabs website [42]. The effective time base is determined using a user defined threshold on the change in the ATN value, which in our case was $\Delta ATN = 0.01$. For $\Delta ATN > 0.01$, the ONA reduction resulted in a very smooth curve which could hide some information about the vertical trends of aerosol properties. Hence, the effective time base is longer for low concentrations and shorter for high concentrations [43].

2.3.4 Estimating Scattering

The scattering coefficient was estimated using the PyMieScatt [44] Python package that uses Lorenz-Mie theory and the Bohren and Hoffman algorithm [45]. We used the Mie_SD () function for polydisperse size distributions of homogeneous spheres. The inputs for the function are: (a) the complex refractive index of the particles, (b) the wavelength of the incident light in nm, (c) the diameter bin midpoints of the size distribution in nm, (d) the number concentration of size distribution bins in number of particles per cubic cm, and (e) the refractive index of the surrounding medium (in our case air, with m=1.00 + 0i).

However, the complex refractive index m = n + ki, of the specific ambient particles measured during our study is unknown. Hence, we used the size distribution from POPS and absorption coefficient from MA200 to improve our estimate of the scattering using PyMieScatt. The POPS is calibrated using polystyrene latex (PSL) spheres with a refractive index of 1.65 + 0i at 405 nm [32]. Hence, the size distribution from the POPS can be underestimated or overestimated for ambient particles since the refractive index of PSL spheres is different from the refractive index of ambient aerosols, especially in terms of the imaginary part, k, which is non-zero when absorbing aerosols are present. Thus, to account for the absorption of the ambient particles we varied the k value keeping the n constant at 1.65 until the absorption coefficient from PyMieScatt matched the measured absorption coefficient to the second decimal place. Finally, we estimated the scattering coefficient using PyMieScatt as well. The flow chart of the method used is shown in figure 2-1.

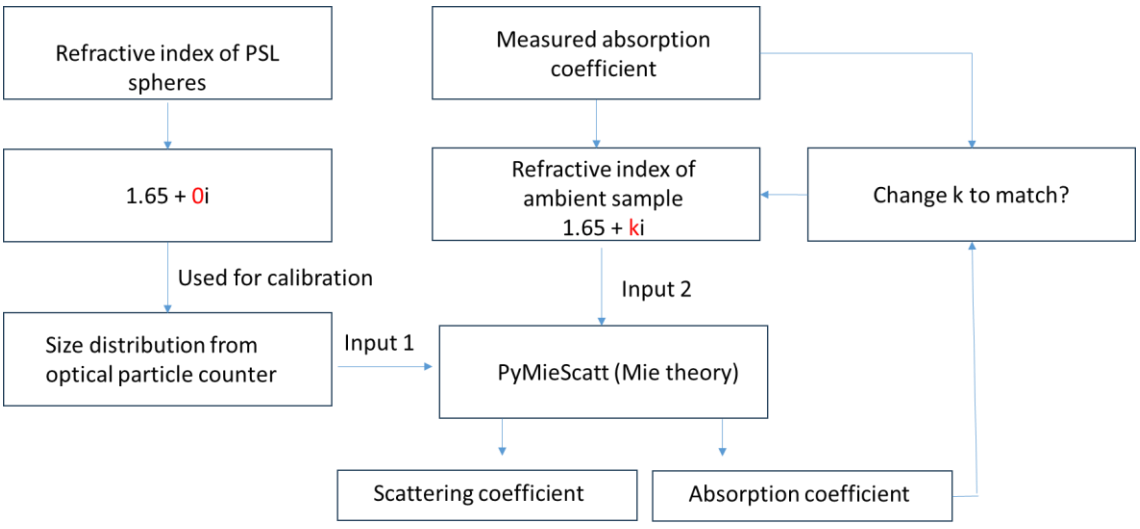

Figure 2-1: Flow chart showing the procedure for estimating scattering by using size distribution from POPS and ambient absorption coefficient measurement from MA200.

To test the goodness of the approach we compared the scattering measurements using a nephelometer at the ground site with the scattering estimated from our method during the periods of the flights when the TBS was loitering near the ground (within 10 to 50 m) (Figure 2-2). We see a good correlation between measured scattering coefficients (Figure 2-3). Only for 23 Feb, we used the measured absorption coefficient from the PSAP for 3

wavelengths (450 nm, 550 nm, and 700 nm) (as the Aethalometer data were noisy) and the size distribution from the POPS to estimate the scattering.

As a further measure of the goodness of the approach, we computed the scattering Ångström exponent (SAE). The SAE quantifies the wavelength dependence of scattering using a power-law fit and it mostly depends on the particle size distributions. From PyMieScatt on 23 Feb the calculated SAE is 1.60 and from the ground nephelometer is 1.79 giving a deviation of 11%. Also for 18 Apri, we see a good correlation with SAE from PyMieScatt equal to 2.42 and from Nephelometer equal to 2.72 with again an 11% deviation. Similarly, for 16 October the PyMieScatt SAE was 1.58 while that calculated from the nephelometer was 1.79 with again a deviation of about 11%.

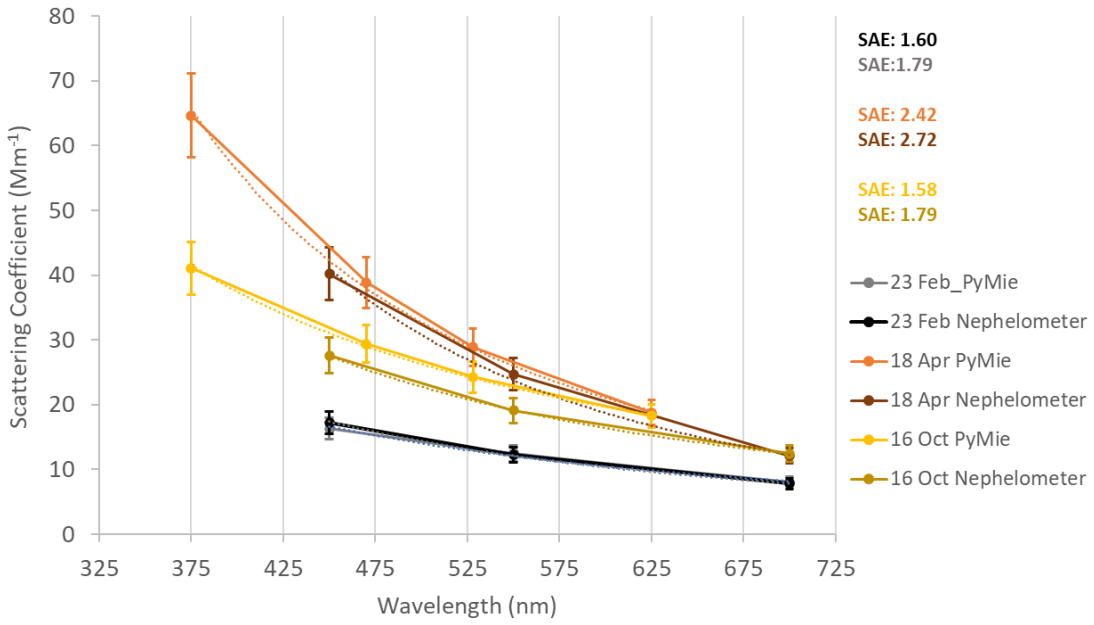

Figure 2-2: Comparison between the scattering measured using a nephelometer at the ground and the estimated scattering from PyMieScatt.

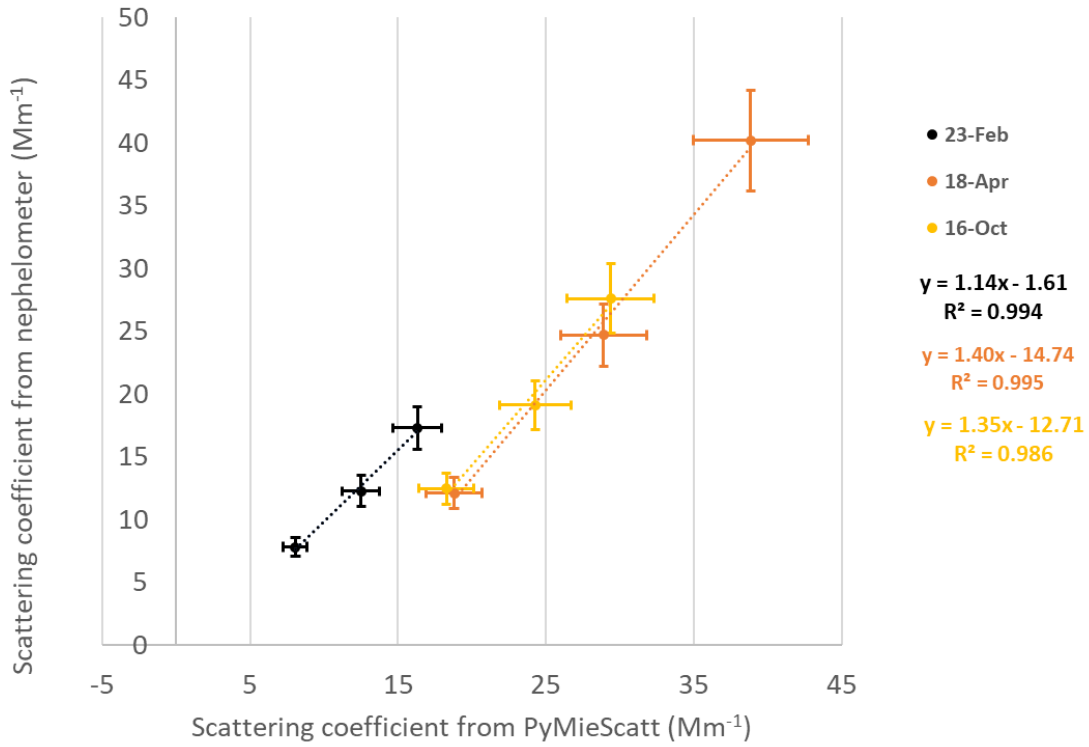

Figure 2-3**:** Comparison between the scattering measured using a nephelometer at the ground and the estimated scattering from PyMieScatt.

2.3.5 Chemical Composition

We determined the elemental composition and morphology of the particles for two samples one collected on 25 February and one on 18 April using computer-controlled scanning electron microscopy with energy dispersed X-ray analysis (CCSEM/EDX) [46]. An Environmental scanning electron microscope (FEI Quanta) was used to analyze the samples. The microscope uses an EDAX X-ray spectrometer with a Si (Li) detector with an active area of 10 mm^2 and an ATW2 window. The X-ray spectra acquired using the EDAX detector provided the elemental composition of the particles in the samples. The CCSEM/EDX was operated with a beam current of 500 pA and an accelerating voltage of 20 kV. Based on the elemental composition obtained from CCSEM/EDX, particles were classified into ten groups such as Na-rich, Na-rich sulfates, Si-rich sulfates, Carbonaceous sulfates, K-rich sulfates, Carbonaceous particles, Carbonaceous coated dust, Sulfate coated dust, Dust, and Others [47]. At least 1000 particles from each sample were analyzed.

2.3.6 Radiative Forcing

We estimated the TOA RF using the SBDART model which requires as aerosol inputs the SSA, asymmetry parameter (g), aerosol optical depth (AOD) and the elevation of the aerosol layer. g is the cosine-weighted average of the scattering phase function and theoretically ranges from -1 for perfect backwards scattering and +1 for complete forward scattering; in the atmosphere, g is typically positive and depends on the particles size. The SSA is the ratio of the scattering coefficient to the total extinction coefficient and ranges between 0 and 1, with 0 being for an ideal perfect absorber and 1 being the SSA value for a non-absorbing particle population. We calculated the SSA using the estimated scattering coefficient and the measured absorption coefficient along the profile. AOD was calculated integrating the extinction profile over the thickness of the aerosol layer as the entire profile altitude change. The instantaneous upwelling ($F^{\uparrow}$) and downwelling ($F^{\downarrow}$) radiation fluxes were calculated using SBDART for a wavelength range from 0.2 to 3μm. These instantaneous fluxes were averaged for 24 hours to calculate the TOA RF of the aerosols within the layer probed by the TBS using the following equation:

$$RF_{no\_aerosol} = F^{\downarrow}_{no\_aerosol} - F^{\uparrow}_{no\_aerosol}$$

$$RF_{total} = F^{\downarrow}_{total} - F^{\uparrow}_{total}$$

$$\text{TOA } RF_{aerosol} = RF_{total} - RF_{no\_aerosol}$$

Where $F^{\downarrow}_{no\_aerosol}$ and $F^{\uparrow}_{no\_aerosol}$ are the averaged (for 24 hours) downwelling and upwelling radiation fluxes for the case of no aerosol (i.e., clear sky), and $F^{\downarrow}_{total}$ and $F^{\uparrow}_{total}$ are the upwelling and downwelling radiation fluxes including an aerosol layer of thickness equal to the difference between the minimum and the maximum altitude of each flight.

2.4 Results and Discussion

2.4.1 Meteorological parameters, particle, and BC concentrations

The three profiles reported in this study were collected on 25 February, 18 April, and 16 October 2022 during different season of the year, winter, spring and fall respectively and hence there is significant variability in the meteorological parameters such as potential

temperature, and relative humidity (Figure 2-4). The potential temperature ranged from -5 °C to -2 °C on 25 Feb which gradually increased from ground to the maximum altitude of the profile (~ 700 m) indicating a stable atmosphere. On 18 April, the potential temperature remained constant at about 18 °C (up to the maximum altitude of ~500 m) with slight drop of ~ 0.5 °C around 300 m altitude leading to a moderately unstable condition with slight mixing. On 16 Oct we find a similar trend as on 25 Feb of the potential temperature increasing gradually from 19 °C to 21 °C to the maximum height of the flight (~ 300 m).

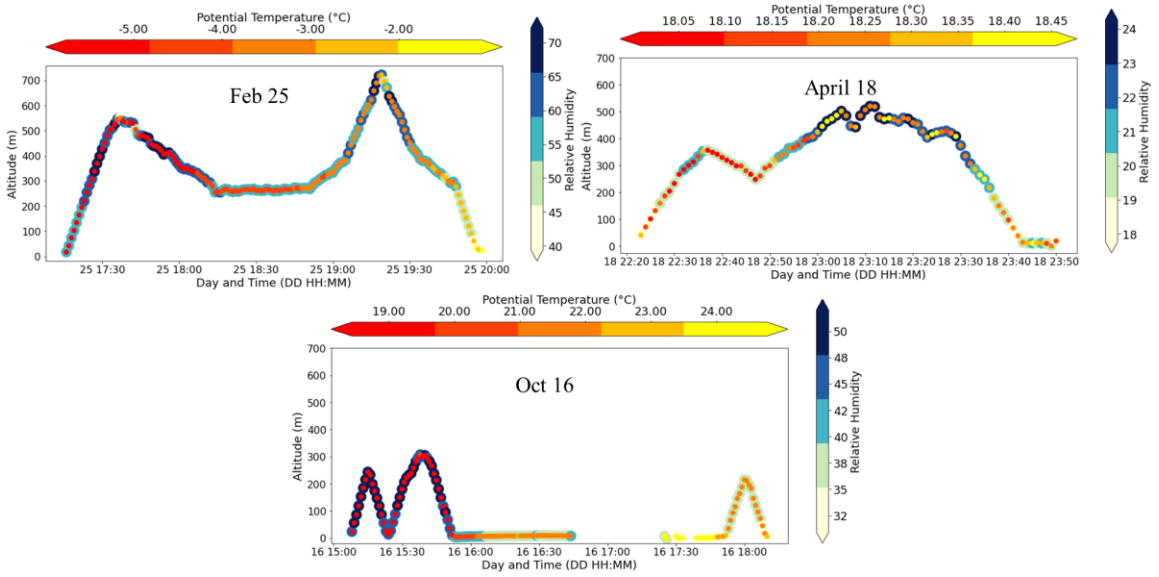

Figure 2-4: Flight profiles as a function of time for three days: 25 Feb 2022, 18 April 2022, and 16 Oct 2022. The potential temperature (°C) is indicated by the fill color of the markers, while the relative humidity (%) is indicated by the color of the markers' borderline.

The relative humidity was high on 25 Feb ranging from 40% to 70%. The driest day was 18 April with low relative humidity ranging from 18% to 24%. Whereas, on 16 Oct the relative humidity was moderate ranging from 32% to 50%.

The BC concentrations measured using the MA200 at the 375 nm wavelength (Figure 2-5(a)) were about 1.4 μgm^{-3} on 18 April with a sudden drop to ~ 0.8 μgm^{-3} at 300 m altitude. However, on 25 Feb and 16 Oct the BC concentrations were steady with respect to altitude with values ranging from ~ 0.1 to 0.2 μgm^{-3} and from ~ 0.3 to 0.5 μgm^{-3}, respectively.

The profiles that we discuss in this study are the descent portions of the flights that started from maximum height. For instance, on 25 Feb the maximum height was attained for the profile at 19:19 hrs. and the descent continued from then till 19:58 hrs., on 18 April the maximum height was reached at 23:30 hrs to 23:40 hrs. and on 16 October, the maximum height was reached at 15:41 hrs. and the descent continued till 15:54 hrs. The total particle concentration measured by the CPC on 25 Feb was the lowest (~2200 particles/cc on average) and there was only a slight variation with respect to altitude. The high relative humidity could have enhanced the chance for the growth of particle diameter through condensation or due to change in chemical composition through aqueous phase reaction because the chemical equilibria depend on the amount of absorbed water resulting in low particle concentration [48]. Whereas on the day with the lowest relative humidity (18 April) the CPC concentrations were the highest (~5500 particles/cc) among the 3 days (Figure 2-5(b)).

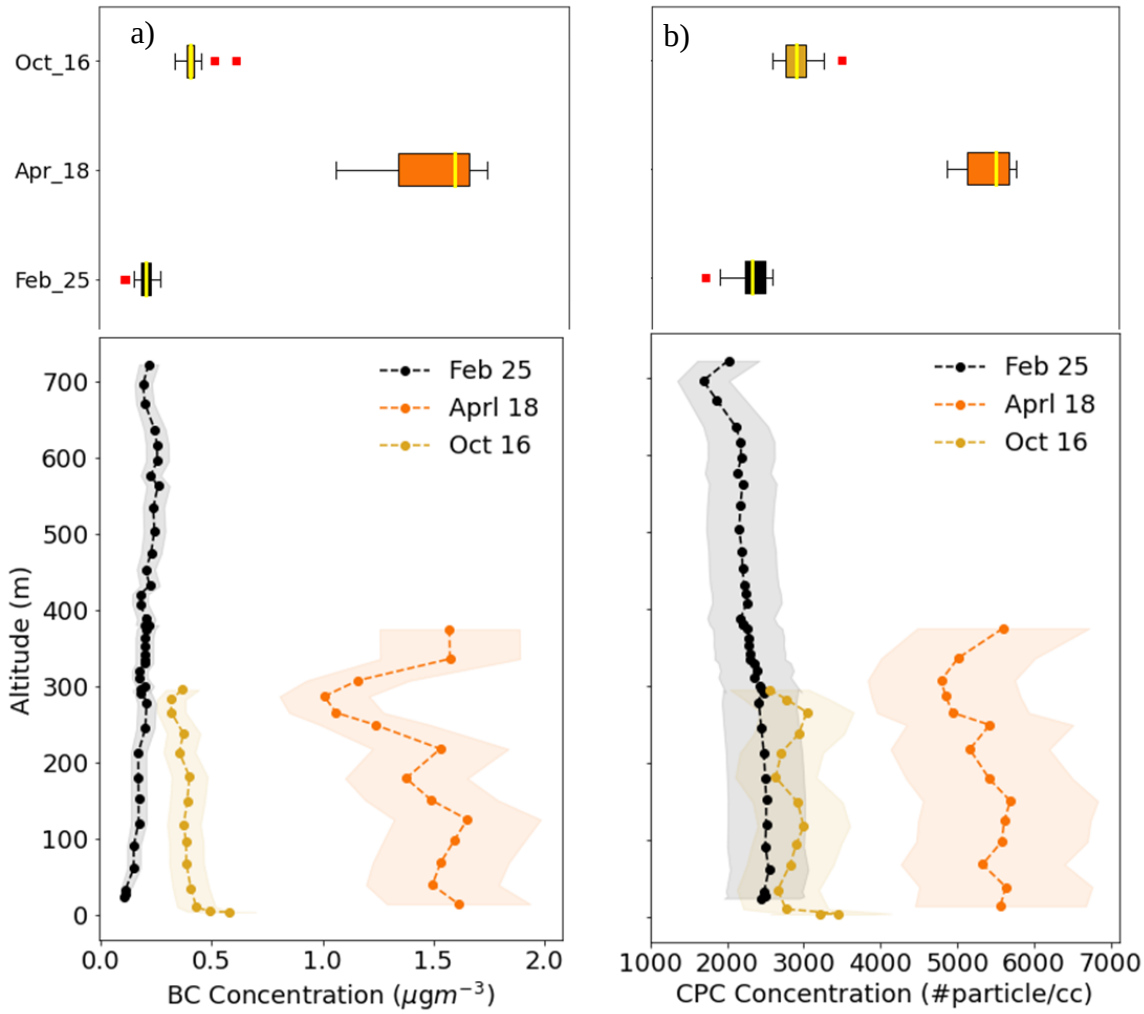

Figure 2-5**:** (a) Black carbon concentration was the highest on 18 April and the lowest on 25 February. (b) The total particle concentrations measured by the CPC measurement also exhibits a maximum of ~5500 #/cc on 18 April. The lowest concentrations were recorded on 25 February with ~2500 #/cc. The shaded bands represent ± 10% for BC concentration and ± 20% for CPC concentration. In the horizontal box plot above, the yellow line represents the median with the whiskers showing 1.5 times the interquartile range (colored box length). The colored regions show the lower and upper quartile, and the red dots are outliers (values greater than 1.5 times the interquartile range).

2.4.2 Optical Properties

The aerosol absorption coefficients for 4 wavelengths (375 nm, 470 nm, 528 nm, and 625 nm) are plotted in figure 2-5. On 25 Feb, the absorption coefficients were in the range of 1 to 3 Mm^{-1} at the ground which increased slightly to a range of 3 to 5 Mm^{-1} at about 700 m, were very low as compared to the other two days. Even though we observed a 26% decrease

in the total concentrations on 25 Feb with respect to the average total concentrations over the altitude in the Figure 2-5(b) from 600 m to 700 m, the decrease in the absorption coefficient with respect to the average over the same altitude was only ~ 2% indicating that the absorbing particles showed small variation throughout the 25 Feb. However, on 18 April, the absorption coefficient showed the highest value among the other days ranging from 5 (at 375 nm) to 13 (625 nm) Mm^{-1} from ground to 350 m. Although, the total particle concentration from CPC showed only a 10% decrease at about 300 m altitude with respect to the average total particle concentration of the profile, we observed a 29% decrease in the BC concentration (Figure 2-5) and 26% decrease in the absorption coefficient with respect to the average absorption coefficient of the profile at 300 m altitude which could indicate that there were higher fraction of absorbing aerosols at 300 m altitude. On 16 Oct, even though the total particle concentrations from CPC (average: 2800 particles/cc) was closer to the values observed on 25 Feb (average: 2200 particles/cc), the absorption coefficients were higher and closer to the absorption coefficients observed on 18 Apr with values ranging from 5 to 10 Mm^{-1} which could indicate that there were higher fraction of absorbing aerosols on 16 Oct as compared to 25 Feb.

The wavelength dependence of the absorption coefficients was small during the 25 Feb flight with an AAE of 1.27 indicating the presence of BC aerosols. However, on 18 April, there was a stronger wavelength dependence giving an AAE of 1.81 which indicates the presence of BrC aerosols. The absorption coefficient on 16 Oct also shows a moderately strong wavelength dependence with an AAE value of 1.54 indicating some presence of BrC.

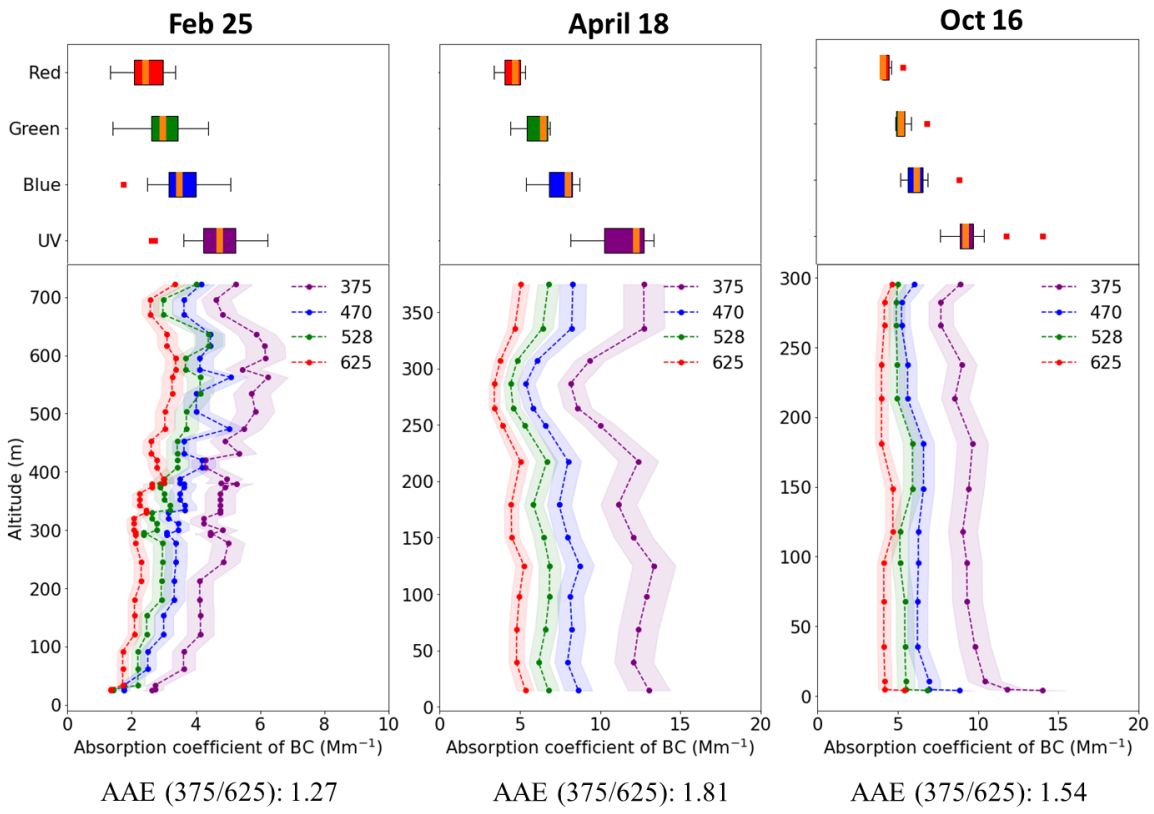

Figure 2-6: Absorption coefficients at 4 wavelengths (375 nm, 470 nm, 528 nm, and 625 nm) for 25 February, 18 April, and 16 October. The shaded region shows the error for absorption coefficients of ± 10% due to uncertainty in the Aethalometer measurements.

From Figure 2-7 we can see that the Scattering coefficients at 375 nm on 25 Feb had only slight variations from 36 to 40 Mm^{-1} below 700 m of altitude with a sharp decrease to about 25 Mm^{-1} (32% decrease) above. Hence, the 32% decrease in scattering coefficient corresponding to 26% decrease in total particle concentration (Figure 2-5 (b)) around 700 m altitude indicates that 25 Feb consists of aerosols that are mostly scattering. However, 18 April shows slightly larger scattering coefficients in the range from 30 to 51 Mm^{-1} from the ground up to an altitude of 400 m. While the absorption coefficients show a 26% drop at 300 m altitude, the scattering coefficients also drop by a significant fraction of 33% with the SSA value dropping to 0.72 at ~ 300 m altitude further showing the evidence for the presence of aerosols that are strongly absorbing. Similarly, on 16 October the SSA values range from 0.75 to 0.81 which is higher than the values reported on 25 Feb (0.85 to 0.93)

and similar to the range of SSA reported on 18 April (0.72 to 0.85) indicating the presence of strongly absorbing aerosols.

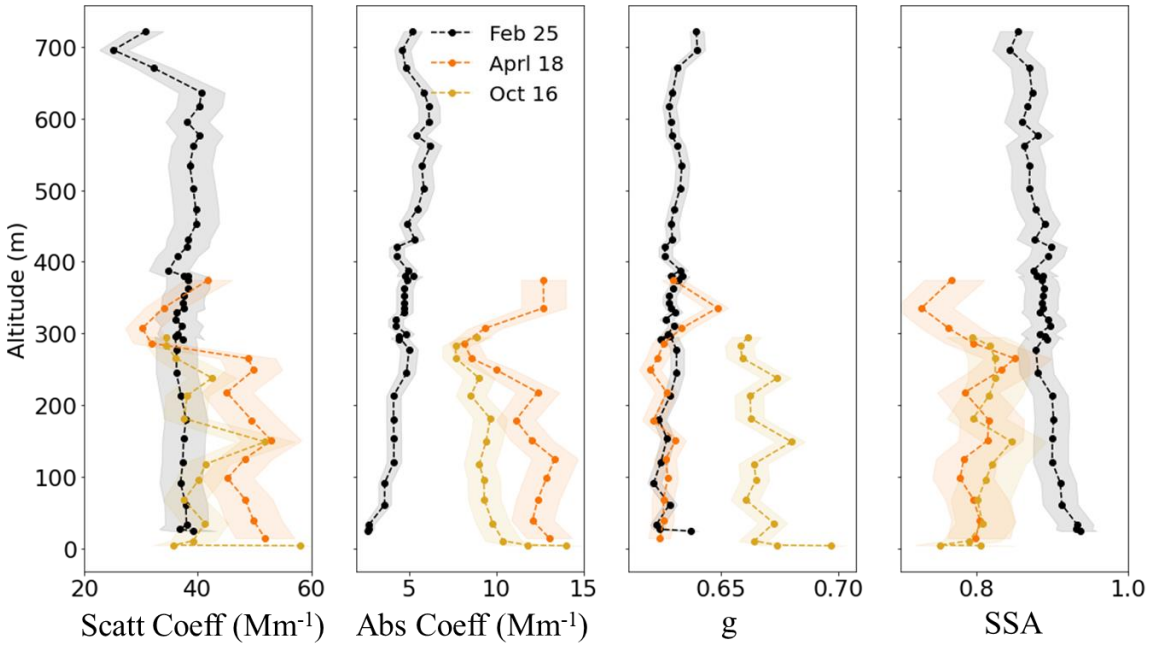

Figure 2-7: Scattering coefficients (Scatt Coeff), absorption coefficients (Abs Coeff), asymmetry parameter values, and single scattering albedo values for 375 nm. The shaded region shows the uncertainty range estimated by accounting for the 10% error in the measurement from POPS and 10% error for the measurement from Aethalometer.

The average g value (Figure 2-7) at 375 nm on 25 Feb and 18 April are the same equal to 0.63 which is typical on a humid day at SGP [49]. The ratio of the total particle concentrations to total POPS concentration on 25 Feb is 5 whereas, the ratio on 18 April is 7.7 which shows that the concentration of larger particles is higher on 25 Feb and 18 April. Hence, the asymmetry parameter on both days is same due to the presence of large sized particles on 25 Feb and 18 April. Similarly, the average g value is 0.67 on 16 Oct due to high humidity (~ 50%) [49] and lower CPC to POPS ratio of 6.

2.4.3 Chemical composition

The chemical composition estimated using the CCSEM on 25 Feb shows a high fraction of carbonaceous sulfates of about 80 to 90% by number for particles in the area equivalent

diameter range from 0.75 to 2 μm. For particles with size between 0.25 and 0.75 μm, the fraction of sulfates ranges from ~25% to 50%. The high humidity conditions on 25 Feb could have led to the dominant fraction of carbonaceous sulfates. Indeed, a recent study on the role of carbonaceous aerosols in the formation of sulfates showed that high humid conditions promote soot to catalyze sulfate production [50]. The fraction of carbonaceous aerosols is 40 to 45% for smaller sized particles with diameter less than 0.75 μm and for larger particles above 0.75 μm the fraction of carbonaceous aerosols is less than 20%. We also observe a small fraction (less than 5%) of other sulfates such as Si-rich sulfates, K-rich sulfates, and Na-rich sulfates. However, on 18 April the fraction of carbonaceous sulfates was only 10 to 20% with carbonaceous aerosols being the dominant species by a fraction of 40% for particles with area equivalent diameter ranging from 0.25 to 0.5 μm. Like for the case on 25 Feb, we observe only less than 5% of other types of aerosols such as Si-rich sulfates, K-rich sulfates, and sulfate coated dust.

The high SSA values (average at 375 nm: 0.89) (Figure 2-6) observed on 25 Feb is probably related to the abundance of sulfate aerosols along with high relative humidity. Other types of aerosols that could lead to larger scattering such dust, and Na-rich particles were present in small fractions (less than 5). Conversely, the lower SSA values (average at 375 nm: 0.79) measured on 18 April are consistent with the larger fraction of carbonaceous aerosols. From Figure 2-5 and 2-6, we also observe that there was high scattering and strong wavelength dependence in the absorption coefficient which indicates that most of the aerosols in the carbonaceous class could have been brown carbon.

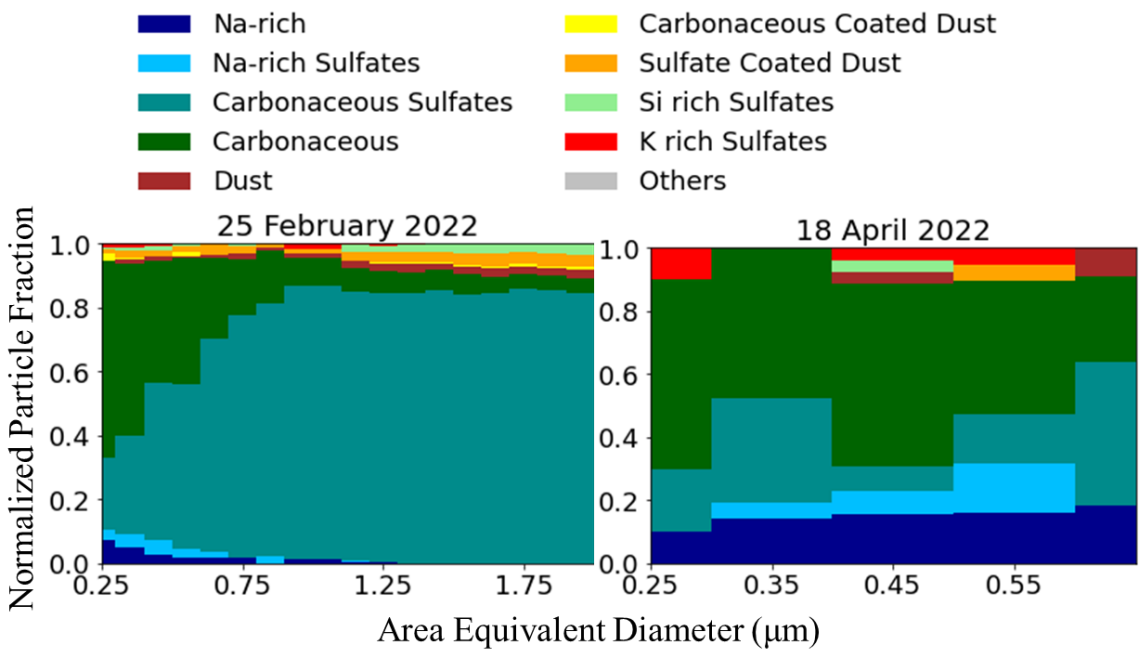

Figure 2-8: Chemical composition of samples collected on 25 Feb and 18 April.

2.5 Conclusions

Our results show the impact of chemical composition of atmospheric aerosols on their optical properties. On 25 Feb, when there was high sulfate fraction, we observed high scattering and low absorption giving a higher SSA as compared to 18 April. A larger fraction of carbonaceous particles on 18 April resulted in lower SSA with strong absorption. Furthermore, the stronger wavelength dependence of the absorption coefficients gives us an indication of the significant presence of brown carbon aerosols.

The aerosol TOA RF depends on the type of aerosols present in the atmosphere. For instance, sulfate aerosols have a cooling effect on the atmosphere with a reported TOA RF in the range from -0.6 to -0.2 Wm^{-2} with an average value of -0.4 Wm^{-2} [14] globally. The average value of RF that we calculated for 25 Feb is -0.3 Wm^{-2} with an uncertainty range of (-0.2 to -0.4 Wm^{-2}) with a surface albedo equal to that of vegetation (Figure 2-8) which is close to the global average value of sulfates reported in the fifth assessment report of IPCC [51]. The global RF of secondary organic aerosols reported in the same report ranges from -0.27 to 0.2 Wm^{-2} with an average value of -0.03 Wm^{-2}, in comparison, the average

RF we calculated for the 18 April was 0.08 Wm^{-2} with uncertainty range of 0.2 to -0.06 Wm^{-2}, for 16 Oct was -0.03 Wm^{-2} with an uncertainty range of 0.03 to -0.08 Wm^{-2}. Although we did not have the single particle chemical composition for 16 Oct, the larger AAE of 1.57 could indicate contributions from brown carbon aerosols. Considering the role of atmospheric aerosols in determining the RF of the atmosphere, there needs to be more field studies to report the real time variability in the RF value with changing chemical composition.

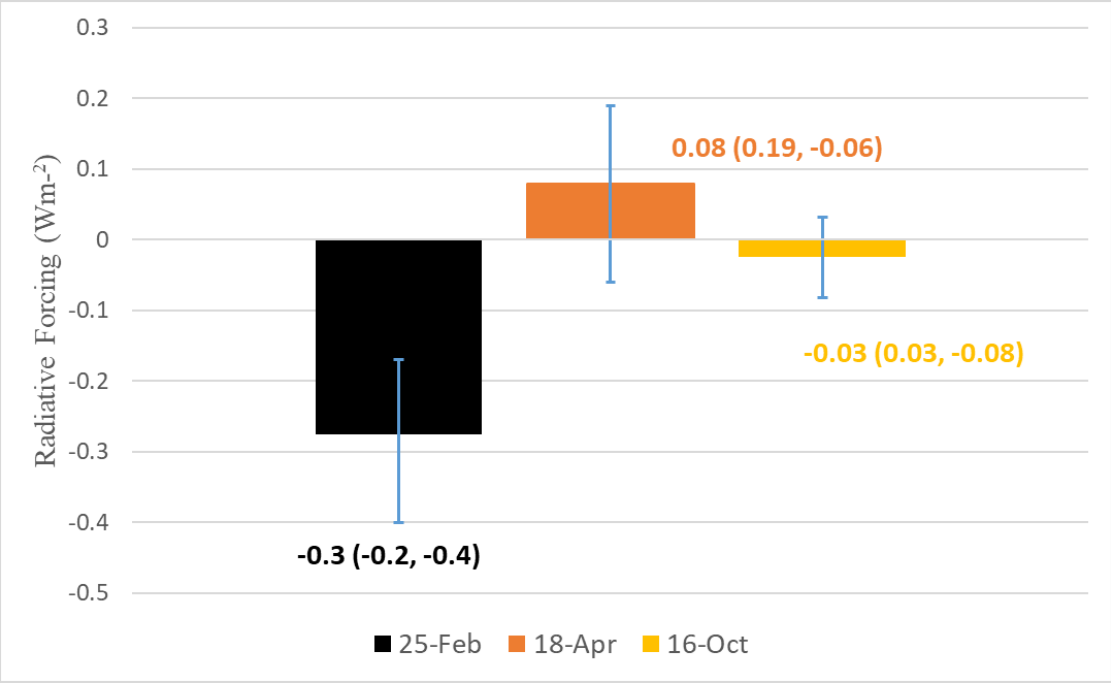

Figure 2-9: Top of the atmosphere RF values calculated using the retrieved optical parameters for the 3 days with vegetation as the surface type.

2.6 References:

1. Cherian, R.; Quaas, J.; Salzmann, M.; Tomassini, L., Black carbon indirect radiative effects in a climate model. *Tellus B: Chemical and Physical Meteorology* **2017,** *69*, (1), 1369342.
2. DeMott, P. J.; Chen, Y.; Kreidenweis, S. M.; Rogers, D. C.; Sherman, D. E., Ice formation by black carbon particles. *Geophysical Research Letters* **1999,** *26*, (16), 2429-2432.
3. Hadley, O. L.; Kirchstetter, T. W., Black-carbon reduction of snow albedo. *Nature Climate Change* **2012,** *2*, (6), 437-440.

4. Choi, J.-O.; Chung, C. E., Sensitivity of aerosol direct radiative forcing to aerosol vertical profile. *Tellus B: Chemical and Physical Meteorology* **2014,** *66*, (1), 24376.
5. Sisterson, D. L.; Peppler, R. A.; Cress, T. S.; Lamb, P. J.; Turner, D. D., The ARM Southern Great Plains (SGP) Site. *Meteorological Monographs* **2016,** *57*, 6.1-6.14.
6. Ricchiazzi, P.; Yang, S.; Gautier, C.; Sowle, D., SBDART: A Research and Teaching Software Tool for Plane-Parallel Radiative Transfer in the Earth's Atmosphere. *Bulletin of the American Meteorological Society* **1998,** *79*, (10), 2101-2114.
7. Ramanathan, V.; Feng, Y., Air pollution, greenhouse gases and climate change: Global and regional perspectives. *Atmospheric Environment* **2009,** *43*, (1), 37-50.
8. Li, J.; Carlson, B. E.; Yung, Y. L.; Lv, D.; Hansen, J.; Penner, J. E.; Liao, H.; Ramaswamy, V.; Kahn, R. A.; Zhang, P.; Dubovik, O.; Ding, A.; Lacis, A. A.; Zhang, L.; Dong, Y., Scattering and absorbing aerosols in the climate system. *Nature Reviews Earth & Environment* **2022,** *3*, (6), 363-379.
9. Ramanathan, V.; Carmichael, G., Global and regional climate changes due to black carbon. *Nature Geoscience* **2008,** *1*, 221.
10. Forster, P.; Ramasvamy, V.; Artaxo, P., IPCC, Climate Change 2007: The Physical Science Basis. Contribution of Working Group I to the Fourth Assessment Report of the Intergovernmental Panel on Climate Change, eds Solomon S, et al. In Cambridge Univ Press, Cambridge, UK, and New York, NY: 2007.
11. Satheesh, S.; Moorthy, K. K.; Babu, S. S.; Vinoj, V.; Dutt, C., Climate implications of large warming by elevated aerosol over India. *Geophysical Research Letters* **2008,** *35*, (19).
12. Li, J.; Jian, B.; Huang, J.; Hu, Y.; Zhao, C.; Kawamoto, K.; Liao, S.; Wu, M., Long-term variation of cloud droplet number concentrations from space-based Lidar. *Remote Sensing of Environment* **2018,** *213*, 144-161.
13. Liu, Q.; Quan, J.; Jia, X.; Sun, Z.; Li, X.; Gao, Y.; Liu, Y., Vertical profiles of aerosol composition over Beijing, China: Analysis of in situ aircraft measurements. *Journal of the Atmospheric Sciences* **2019,** *76*, (1), 231-245.
14. Ramaswamy, V.; Collins, W.; Haywood, J.; Lean, J.; Mahowald, N.; Myhre, G.; Naik, V.; Shine, K. P.; Soden, B.; Stenchikov, G.; Storelvmo, T., Radiative Forcing of Climate: The Historical Evolution of the Radiative Forcing Concept, the Forcing Agents and their Quantification, and Applications. *Meteorological Monographs* **2019,** *59*.
15. Haywood, J. M.; Ramaswamy, V., Global sensitivity studies of the direct radiative forcing due to anthropogenic sulfate and black carbon aerosols. **1998,** *103*, (D6), 6043-6058.
16. Corrigan, C. E.; Roberts, G. C.; Ramana, M. V.; Kim, D.; Ramanathan, V., Capturing vertical profiles of aerosols and black carbon over the Indian Ocean using autonomous unmanned aerial vehicles. *Atmos. Chem. Phys.* **2008,** *8*, (3), 737-747.
17. Ferrero, L.; Castelli, M.; Ferrini, B. S.; Moscatelli, M.; Perrone, M. G.; Sangiorgi, G.; D'Angelo, L.; Rovelli, G.; Moroni, B.; Scardazza, F.; Močnik, G.; Bolzacchini, E.; Petitta, M.; Cappelletti, D., Impact of black carbon aerosol over Italian basin valleys: high-resolution measurements along vertical profiles, radiative forcing and heating rate. *Atmos. Chem. Phys.* **2014,** *14*, (18), 9641-9664.
18. Ferrero, L.; Mocnik, G.; Ferrini, B. S.; Perrone, M. G.; Sangiorgi, G.; Bolzacchini, E., Vertical profiles of aerosol absorption coefficient from micro-

Aethalometer data and Mie calculation over Milan. *Science of The Total Environment* **2011,** *409*, (14), 2824-2837.
19. Kim, S.-W.; Yoon, S.-C.; Kim, J.; Kim, S.-Y., Seasonal and monthly variations of columnar aerosol optical properties over east Asia determined from multi-year MODIS, LIDAR, and AERONET Sun/sky radiometer measurements. *Atmospheric Environment* **2007,** *41*, (8), 1634-1651.
20. Taubman, B. F.; Hains, J. C.; Thompson, A. M.; Marufu, L. T.; Doddridge, B. G.; Stehr, J. W.; Piety, C. A.; Dickerson, R. R., Aircraft vertical profiles of trace gas and aerosol pollution over the mid-Atlantic United States: Statistics and meteorological cluster analysis. *Journal of Geophysical Research: Atmospheres* **2006,** *111*, (D10).
21. Wang, W.; Shao, L.; Mazzoleni, C.; Li, Y.; Kotthaus, S.; Grimmond, S.; Bhandari, J.; Xing, J.; Feng, X.; Zhang, M., Measurement report: Comparison of wintertime individual particles at ground level and above the mixed layer in urban Beijing. *Atmospheric Chemistry and Physics* **2021,** *21*, (7), 5301-5314.
22. Schuster, G. L.; Dubovik, O.; Holben, B. N.; Clothiaux, E. E., Inferring black carbon content and specific absorption from Aerosol Robotic Network (AERONET) aerosol retrievals. *Journal of Geophysical Research: Atmospheres* **2005,** *110*, (D10).
23. Cheng, Z.; Liyu, A.; Dexheimer, D.; Lata, N. N.; Kulkarni, G.; Longbottom, C. M.; Mei, F.; China, S., An Automated Size and Time-resolved Aerosol Collector Platform Integrated with Environmental Sensors to Study Vertical Profile of Aerosol. *Environmental Science: Atmospheres* **2022**.
24. Ensor, D. S.; Charlson, R. J.; Ahlquist, N. C.; Whitby, K. T.; Husar, R. B.; Liu, B. Y. H., Multiwavelength nephelometer measurements in Los Angeles smog aerosol. I. Comparison of calculated and measured light scattering. *Journal of Colloid and Interface Science* **1972,** *39*, (1), 242-251.
25. Hegg, D. A.; Hobbs, P. V.; Gassó, S.; Nance, J. D.; Rangno, A. L., Aerosol measurements in the Arctic relevant to direct and indirect radiative forcing. *Journal of Geophysical Research: Atmospheres* **1996,** *101*, (D18), 23349-23363.
26. Anderson, T.; Covert, D.; Marshall, S.; Laucks, M.; Charlson, R.; Waggoner, A.; Ogren, J.; Caldow, R.; Holm, R.; Quant, F., Performance characteristics of a high-sensitivity, three-wavelength, total scatter/backscatter nephelometer. *Journal of Atmospheric and Oceanic Technology* **1996,** *13*, (5), 967-986.
27. Quinn, P.; Anderson, T.; Bates, T.; Dlugi, R.; Heintzenberg, J.; von Hoyningen-Huene, W.; Kulmala, M.; Russell, P.; Swietlicki, E., Closure in tropospheric aerosol-climate research: A review and future needs for addressing aerosol direct shortwave radiative forcing. *Contributions to atmospheric physics* **1996,** *69*.
28. Liu, Y.; Daum, P. H., THE EFFECT OF REFRACTIVE INDEX ON SIZE DISTRIBUTIONS AND LIGHT SCATTERING COEFFICIENTS DERIVED FROM OPTICAL PARTICLE COUNTERS. *Journal of Aerosol Science* **2000,** *31*, (8), 945-957.
29. Dexheimer, D. *Tethered Balloon System (TBS) Instrument Handbook*; ARM Climate Research Facility: United States, 2018; p Medium: ED; Size: 39 p.
30. Mei, F.; Pekour, M. S.; Dexheimer, D.; de Boer, G.; Cook, R.; Tomlinson, J.; Schmid, B.; Goldberger, L. A.; Newsom, R.; Fast, J. D., Observational data from uncrewed systems over Southern Great Plains. *Earth Syst. Sci. Data* **2022,** *14*, (7), 3423-3438.

31. Kuang, C. *Condensation Particle Counter Instrument Handbook*; United States, 2016; p Medium: ED; Size: 22 p.
32. Scientific, H. Portable Optical Particle Spectrometer. https://handixscientific.com/pops/
33. microAeth MA Series MA200, MA300, MA350 Operating Manual. https://aethlabs.com/sites/all/content/microaeth/maX/MA200%20MA300%20MA350%20Operating%20Manual%20Rev%2003%20Dec%202018.pdf
34. Zheng, X.; Xi, B.; Dong, X.; Logan, T.; Wang, Y.; Wu, P., Investigation of aerosol–cloud interactions under different absorptive aerosol regimes using Atmospheric Radiation Measurement (ARM) southern Great Plains (SGP) ground-based measurements. *Atmos. Chem. Phys.* **2020,** *20*, (6), 3483-3501.
35. Jefferson, A. *Aerosol Observing System (AOS) Handbook*; PNNL; Richland, WA: United States, 2011; p Medium: ED.
36. Anderson, T.; Covert, D.; Wheeler, J.; Harris, J.; Perry, K.; Trost, B.; Jaffe, D.; Ogren, J., Aerosol backscatter fraction and single scattering albedo: Measured values and uncertainties at a coastal station in the Pacific Northwest. *Journal of Geophysical Research: Atmospheres* **1999,** *104*, (D21), 26793-26807.
37. Zhao, G.; Yu, Y.; Tian, P.; Li, J.; Guo, S.; Zhao, C., Evaluation and correction of the ambient particle spectral light absorption measured using a filter-based aethalometer. *Aerosol and Air Quality Research* **2020,** *20*, (8), 1833-1841.
38. Chang, L.; Li, J.; Chu, Y.; Dong, Y.; Tan, W.; Xu, X.; Ren, J.; Tian, X.; Li, C.; Liu, Z.; Zhao, G.; Li, C., Variability of surface aerosol properties at an urban site in Beijing based on two years of in-situ measurements. *Atmospheric Research* **2021,** *256*, 105562.
39. Rajesh, T. A.; Ramachandran, S., Black carbon aerosol mass concentration, absorption and single scattering albedo from single and dual spot aethalometers: Radiative implications. *Journal of Aerosol Science* **2018,** *119*, 77-90.
40. Ramachandran, S.; Kedia, S., Aerosol radiative effects over an urban location and a remote site in western India: seasonal variability. *Atmospheric environment* **2011,** *45*, (39), 7415-7422.
41. Ramachandran, S.; Kedia, S., Black carbon aerosols over an urban region: Radiative forcing and climate impact. *Journal of Geophysical Research: Atmospheres* **2010,** *115*, (D10).
42. Aethlabs https://aethlabs.com/
43. Liu, X.; Hadiatullah, H.; Zhang, X.; Hill, L. D.; White, A. H. A.; Schnelle-Kreis, J.; Bendl, J.; Jakobi, G.; Schloter-Hai, B.; Zimmermann, R., Analysis of mobile monitoring data from the microAeth® MA200 for measuring changes in black carbon on the roadside in Augsburg. *Atmos. Meas. Tech.* **2021,** *14*, (7), 5139-5151.
44. Sumlin, B. J.; Heinson, W. R.; Chakrabarty, R. K., Retrieving the aerosol complex refractive index using PyMieScatt: A Mie computational package with visualization capabilities. *Journal of Quantitative Spectroscopy and Radiative Transfer* **2018,** *205*, 127-134.
45. Bohren, C. F.; Huffman, D. R., *Absorption and scattering of light by small particles*. John Wiley & Sons: 2008.

46. Bondy, A. L.; Bonanno, D.; Moffet, R. C.; Wang, B.; Laskin, A.; Ault, A. P., The diverse chemical mixing state of aerosol particles in the southeastern United States. *Atmospheric chemistry and physics* **2018,** *18*, (16), 12595-12612.
47. Lata, N. N.; Cheng, Z.; Dexheimer, D.; Zhang, D.; Mei, F.; China, S., Vertical Gradient of Size-Resolved Aerosol Compositions over the Arctic Reveals Cloud Processed Aerosol in-Cloud and above Cloud. *Environmental Science & Technology* **2023,** *57*, (14), 5821-5830.
48. Winkler, P., The growth of atmospheric aerosol particles with relative humidity. *Physica Scripta* **1988,** *37*, (2), 223.
49. Ogren, J.; Andrews, E.; McComiskey, A.; Sheridan, P.; Jefferson, A.; Fiebig, M. In *New insights into aerosol asymmetry parameter*, Proceedings of the 16th ARM Science Team Meeting, Albuquerque, NM, USA, 2006; Citeseer: 2006; pp 27-31.
50. He, G.; Ma, J.; He, H., Role of Carbonaceous Aerosols in Catalyzing Sulfate Formation. *ACS Catalysis* **2018,** *8*, (5), 3825-3832.
51. Stocker, T. F.; Qin, D.; Plattner, G.-K.; Tignor, M. M.; Allen, S. K.; Boschung, J.; Nauels, A.; Xia, Y.; Bex, V.; Midgley, P. M., Climate Change 2013: The physical science basis. contribution of working group I to the fifth assessment report of IPCC the intergovernmental panel on climate change. **2014**.

3 Optical Properties of Individual Tar Balls in the Free Troposphere

3.1 Abstract

Tar balls are brown carbonaceous particles, highly viscous, spherical, amorphous, and light absorbing. They are believed to form in a biomass burning smoke plumes during transport in the troposphere. Tar balls are believed to have a significant impact on the Earth's radiative balance, but due to poorly characterized optical properties, this impact is highly uncertain. Here, we used two nighttime samples to investigate the chemical composition and optical properties of individual tar balls transported in the free troposphere to the Climate Observatory "Ottavio Vittori" on Mt. Cimone, Italy using multi-modal micro-spectroscopy. In our two samples, tar balls contributed 50% of carbonaceous particles by number. Of those tar balls, 16% were inhomogeneously mixed with other constituents. Using electron energy loss spectroscopy, we retrieved the complex refractive index for a wavelength range from 200 to 1200 nm for both inhomogeneously and homogeneously mixed tar balls. We found no significant difference in the average refractive index of inhomogeneously and homogenously mixed tar balls (1.40 - 0.03i, and 1.36 - 0.03i at 550 nm, respectively). Furthermore, we estimated the top of the atmosphere radiative forcing using the Santa Barbara DISORT Atmospheric Radiative Transfer model (SBDART) and found that a layer of only tar balls with an optical depth of 0.1 above vegetation would exert a positive radiative forcing ranging from 2.8 Wm^{-2} (on a clear sky day) to 9.5 Wm^{-2} (when clouds are below the aerosol layer). Understanding the optical properties of tar balls can help reduce uncertainties associated with the contribution of biomass-burning aerosol in current climate models.

3.2 Introduction

About 88% by mass of carbonaceous aerosol[1] present in the atmosphere is either directly emitted from biomass combustion or formed in biomass burning plumes, of which about 80% is emitted from the smoldering phase [2]. These carbonaceous aerosols are broadly classified as organic carbon (OC) and black carbon (BC). Bond et al. [1] estimated that the global annual emission of OC is 33.9 Tg/yr considering the emissions from fossil fuels,

biofuels, urban waste burning, and open biomass combustion (31 Tg/yr of OC is emitted just from biomass/biofuel combustion). While BC absorbs efficiently all visible and near infrared wavelengths, a type of OC, termed brown carbon (BrC), has a much steeper increase in absorption efficiency from the visible to the UV wavelength range. BrC is found to have varied compositions and phase states based on their source of formation in the atmosphere [3, 4]. The phase properties of BrC particles range from the low viscosity of some secondary organic aerosols to the high viscosity of tar balls (TBs) [5, 6]. BrC is often observed in the free troposphere and experiences atmospheric ageing during transport [7]. TBs are often formed during transport of smoke emitted in the smoldering phase of biomass burning [8] and are typically identified using electron microscopy as amorphous spherical carbonaceous particles with high resistance to the electron beam [8,9]. Previous studies show that the number fraction of TBs in freshly emitted smoke is only ~15% [10] and increases to ~80% in aged plumes [11]. The processes leading to the formation of TBs is not well understood but a recent study [12] found that low viscous organic particles are transformed into TBs within several hours of emission by the addition of O- and N-containing compounds such as carboxylic acid, and other organonitrates compounds.

For spherically symmetric particles, the absorption and scattering cross sections at a given wavelength can be calculated from their refractive indices (RI) and size using Lorentz-Mie theory. Previously published values for the real part, *m*, of the RI of TBs range from 1.56 [13] to 1.88 [14] at 550 nm. The imaginary part (k) varies over two orders of magnitude, ranging from 0.002 at 532 nm [15] to 0.27 at 550 nm [16]. For instance, an RI of 1.87-0.0056i was found for laboratory-generated TBs from smoldering combustion of Ponderosa pine duff [15]. Whereas in another laboratory study, Hoffer et al. generated TBs from droplets of wood tar and estimated an RI of 1.84 - 0.21i at 550 nm [17]. Alexander et al. reported a RI of 1.67 – 0.27i at 550 nm for TBs found in ambient samples collected above the Yellow sea [16]. Table S1, in the supplementary material, lists the reported values of RI for TBs from previous studies. A recent study highlights that the O/C of freshly emitted TBs increased from 0.24 to 0.38 after 6.7 atmospheric equivalent aging days of photochemical oxidation in a NO_x free atmosphere and, as a result, the RI decreased from

1.661 - 0.020i to 1.632 - 0.007i [18]. During long-range transportation in the atmosphere, TBs from wildfires or other biomass burning may undergo similar processes such as photochemical oxidation.

The RI of individual particles depends on their chemical composition; hence it is important to study single particle properties to understand the influence of atmospheric aging on the RI. In addition, even at the single particle level, aerosols can be inhomogeneously and homogeneously mixed [19]. Inhomogeneously mixed TBs could have different RI than homogeneously mixed TBs. However, the difference in RI for inhomogeneously and homogeneously mixed TBs has not been investigated yet.

Several previous studies [16, 20, 21] used scanning transmission electron microscopy coupled with electron energy loss spectroscopy (STEM/EELS) to investigate single particle properties and report the RI of different carbonaceous aerosols. In this study, we used a similar approach to study the optical properties of individual TBs. TEM lacey film grids were used for STEM/EELS analysis. Specifically, we analyzed 14 TBs collected in the free troposphere at the Climate Observatory "Ottavio Vittori" on Mt. Cimone, an elevated site in the Apennines in northern Italy. We probed individual particles to characterize their chemical composition and carbon functionalities using multi-modal micro-spectroscopy techniques. We applied STEM/EELS [16, 20] to retrieve the RI of individual TB particles in the 200-1200 nm wavelength range. We also compared the RI of inhomogeneously and homogeneously mixed TBs. Further, we applied Lorentz-Mie theory to calculate the scattering (Q_{sca}) and absorption (Q_{abs}) efficiencies, the asymmetry parameter (g), the absorption Ångström exponent (AAE), and the single scattering albedo (SSA). We conclude our discussion by presenting estimates of the potential radiative forcing of these particles using the Santa Barbara DISORT atmospheric radiative transfer model (SBDART).

3.3 Experimental Section

3.3.1 Sampling site, sample collection, and backward trajectory simulations

Samples were collected at the Climate Observatory "Ottavio Vittori" on Mt Cimone. The observatory is part of the GAW-WMO Station "Monte Cimone" (GAW ID: CMN) that sits

~2165 m above sea level [22]. The site is in the Italian Apennine Mountain ridge, southwest of the Po Valley, in the northern Mediterranean basin and south of continental Europe. Due to its altitude, the site is ideal to study aerosol properties in the free troposphere. Five aerosol samples were collected on July 20th, 2017, at 8:00 AM, 11:00 AM, 2:00 PM, 9:00 PM and 11:00 PM (local time), using a 4-stage cascade impactor (Sioutas Personal Cascade impactor, SKC) operated at a flow rate of 9 L/min. This study discusses samples collected on stages C and D (particle 50% cut-off aerodynamic diameters: stage C – 0.50 μm, and stage D –0.25 μm). Due to poor loadings on the substrate, both TEM B-film and lacey film grids were used for CCSEM-EDX analysis to obtain enough particles. Here we focus on the two nighttime samples because of the higher fraction of carbonaceous aerosols (~50% of the total 1500 particles) with respect to the daytime (~25%). To study the origin and transport paths of air masses that reached the site during the sampling periods, we performed backward trajectory analysis with the ERA5 re-analysis data from ECWMF using the Lagrangian Flexible Particle (FLEXPART) [23, 24] dispersion model (Figure A.3-1). The ERA5 global meteorological data were used for 137 vertical levels at a spatial resolution of 0.5 degrees. The analysis of the FLEXPART trajectories confirms that the air was mostly transported in the free troposphere. From Figure A.3-1 we observe that while the air was enriched with carbonaceous aerosol especially below the PBL, the air was subsequently lifted and transported in the free troposphere before arriving at the site location. The percentage of sea salt observed in the sample is related to the fraction of air masses that were affected by PBL air close to the site location and mixed with a still considerable fraction of air being advected in the free troposphere.

3.3.2 Single particle chemical imaging

We determined the chemical composition of individual particles using computer-controlled scanning electron microscopy (Thermo Fisher, model Quanta 3D) with energy dispersive x-ray spectroscopy (EDAX, Inc.) (CCSEM-EDX) [25]. The instrument was set to detect 15 commonly observed elements: C, N, O, Na, Mg, Al, Si, P, S, Cl, K, Ca, Mn, Fe, and Zn. From the relative atomic percentage of each element, we classified each particle into 6 groups: (1) sea salt, (2) sea salt and sulfate, (3) sulfate, (4) carbonaceous, (5) dust, and (6) others. Figure A.3-2 shows the threshold values of atomic percentage of elements for

particle classification. At least 500 particles were analyzed for each of the five samples. The instrument also provided a measurement of the projected area equivalent diameter of each particle, which ranged from 0.25 µm to 1.8 µm. High vacuum condition (~$2x10^{-6}$ Torr) within the SEM might lead to losses of volatile and semi volatile materials. In addition, we used scanning transmission electron microscopy (Thermo Fisher, model Titan 80-300) (STEM)/EDX (Oxford Instruments) to obtain maps of single TBs that were identified by their spherical morphology and high resistance to the electron beam [11]. We observed that some TBs contained elements such as K and S internally mixed within the particle (from here on referred to as inhomogeneous TBs), while others had only C and O homogeneously distributed throughout the particle (homogeneous TBs). Carbon functionalities of TBs were probed using synchrotron-based scanning transmission X-ray microscopy with near edge X-ray absorption fine structure spectroscopy (STXM/NEXAFS) at the beamline 5.3.2.2 of the Advanced Light Source facility located in the Lawrence Berkeley National Laboratory. The samples were raster scanned using the X-ray beam. The intensities of transmitted X-rays were recorded as 111 individual images each representing a fixed photon energy around the carbon K-edge. Carbon functionalities were identified based on the observed peaks at different energy values. For instance, the peaks at 285.1 eV, 286.6 eV, 288.6 eV, 289.5 eV and 287.7 eV represent C=C, C=O, COOH, C-OH and C-H functionalities, respectively [26].

3.3.3 Refractive index retrieval

An aberration corrected STEM/EELS with monochromatic beam was used to calculate the complex RI of individual TBs collected on the lacey carbon substrates from the 11:00 PM sample in the wavelength range from 200 to 1200 nm. A Gatan EELS spectrometer controlled by Digital Micrograph software was used to conduct the EELS measurements. The EELS monochromator generates a narrow beam with an energy dispersion of 0.025 eV/channel. The instrument was operated at 80 kV to reduce Cherenkov radiation effects and reduce damage to the particles from the electron beam [20, 27, 28]. Eight inhomogeneously mixed particles and six homogeneously mixed particles were analyzed for this study. Due to the limited number of samples in our study, we cannot assume that the reported RI values are valid in general for all free tropospheric TBs. The optimized thickness of a particle to

do EELS ranges from 50 to 150 nm to avoid excessive plural scattering [29]. We selected TBs in the size range of 50-200 nm. To remove plural scattering we used the deconvolution method as described in Egerton et al. [29] Hence, the few TBs that exceeded the size range mentioned above, we removed the plural scattering using the deconvolution method (Figure A.3-3). As a first step, the imaginary part of the inverse of the dielectric function is calculated using the relation between the single-scattering EELS spectrum *S(E)* and $Im\left[\frac{-1}{\varepsilon(E)}\right]$,

$$Im\left[\frac{-1}{\varepsilon(E)}\right] = \frac{\pi a_0 m_0 v^2}{2 I_0 t} S(E) \frac{1}{\int_0^{\beta} \frac{\theta d\theta}{\theta^2 + \theta_{\mathrm{E}}^2}} \quad (1)$$

Where I_o represents the zero-loss intensity, t is the thickness of the particle, v is the speed of the incident electron, a_o is the integral of the zero loss peak, m_o is the rest mass of the electron, β is the collection semi-angle, and θ_E is the characteristic scattering angle for an energy loss E (Figure A.3-4). The wavelength dependence of the RI comes from the scattering spectrum S(E) where E represents each energy loss detected from the EELS spectrum which corresponds to the wavelength by the relation $E = h\nu$.To calculate the real part of the dielectric function we used the Kramers-Kronig transformation since the dielectric response function is directly related to the real RI. The equation used to calculate the $Re\left[\frac{1}{\varepsilon(E)}\right]$ is,

$$Re\left[\frac{1}{\varepsilon(E)}\right] = 1 - \frac{2}{\pi} P \int_0^{\infty} Im\left[\frac{-1}{\varepsilon(E')}\right] \frac{E' dE'}{E'^2 - E^2} \quad (2)$$

Where P is the Cauchy principal part of the integral and the weighting function, $\frac{E'}{E'^2 - E^2}$ is the maximum energy loss near the peak E.

The Kramers-Kronig relation was computed using a modified MATLAB KraKro code (http://tem-eels.com) based on the Fourier transform technique elucidated in the book by Egerton [29]. The dielectric function, $\varepsilon(E) = \varepsilon_1 + i\varepsilon_2$ was then calculated from $Re\left[\frac{1}{\varepsilon(E)}\right]$ and

$Im\left[\frac{-1}{\varepsilon(E)}\right]$. Finally, the RI was calculated using the relationship $RI = m - ik = \sqrt{\varepsilon(E)}$. Optical parameters such as absorption efficiency (Q_{abs}), scattering efficiency (Q_{sca}), and single scattering albedo (*SSA*) were calculated using the calculated RI, the measured particle size, and a MATLAB code based on Lorentz-Mie theory [20, 29].

The SSA and asymmetry parameter (g) of the TBs derived from Mie theory were used as inputs to the SBDART model [30] to calculate instantaneous net radiation fluxes at the top of the atmosphere (TOA). Since the Aerosol Optical Depth (AOD) of the TB layer could vary in the real atmosphere, we calculated TOA radiative forcing (TOA RF) using AOD from 0 to 0.1 in steps of 0.01. The SBDART model calculates the instantaneous upwelling ($F^{\uparrow}$) and downwelling ($F^{\downarrow}$) radiation fluxes for a user defined wavelength range of 0.2 – 3 μm based on the input parameters such as zenith angle, spectral optical properties of the layer of aerosols, season, surface albedo, etc. (detailed explanation regarding the input parameters can be found in the Appendix). The instantaneous net fluxes are averaged for 24 hours to calculate daily TOA RFs for aerosols as:

$$RF_{no\_aerosol} = F^{\downarrow}_{no\_aerosol} - F^{\uparrow}_{no\_aerosol} \quad (3)$$

$$RF_{total} = F^{\downarrow}_{total} - F^{\uparrow}_{total} \quad (4)$$

$$\text{TOA } RF_{aerosol} = RF_{total} - RF_{no\_aerosol} \quad (5)$$

Where $F^{\downarrow}_{no\_aerosol}$ and $F^{\uparrow}_{no\_aerosol}$ are the averaged downwelling and upwelling radiation fluxes for the case of no aerosol (i.e., clear sky or cloud layer of thickness 1000 m at an average elevation of 3000 m, for two different scenario), $F^{\downarrow}_{total}$ and $F^{\uparrow}_{total}$ are the upwelling and downwelling radiation fluxes including an aerosol layer of thickness 100 m at an altitude of 2165 m.

3.4 Results and Discussion

3.4.1 Sources, size distribution and chemical composition of carbonaceous particles

The CCSEM/EDX results from Figure 3-1, shows that the area equivalent diameter of particles in the samples ranges from 0.25 to 1.8 μm. The carbonaceous particles for diameters less than 0.75 μm with number of particles ranged from 60% to 80%, and 25% to 45% on the samples collected at 9:00 PM, and 11:00 PM, respectively (Figure 3-1).

Figure A.3-5 shows the emissions from GEOS-Carb CASA-GFED daily wildfire and fuel wood burning emissions 0.5 degree x 0.5 degree produced using the CASA-GFED3 Model [31] and the EDGAR black carbon monthly emissions database [32]. The analysis reveals how the site has been affected by a mixture of sources. At 9PM (Figure A.3-5), carbonaceous material was transported from distant regions to the site including emissions from wildfires in the Iberian Peninsula and wood burning from North Africa with a transport time respectively of 5-6 days and 8 days. Air has then been lifted to the free troposphere before reaching the Mt. Cimone site. The airmass samples at 11PM was influence from the Tyrrhenian Sea surface, has some limited contribution from the Iberian Peninsula and North Africa, and a dominant contribution from fresh wildfires emissions (one day of transport) from Italy and Corsica and three days of transport from Croatia. However, we caution that the residence time in the free troposphere of TBs specifically is not resolved by the model and therefore is still uncertain. The trajectory model suggests that the wildfires represent the most intense contribution to aerosol mass concentration for both episodes, with a total contribution estimated in the range of 0.1-0.5 ug/m^3.

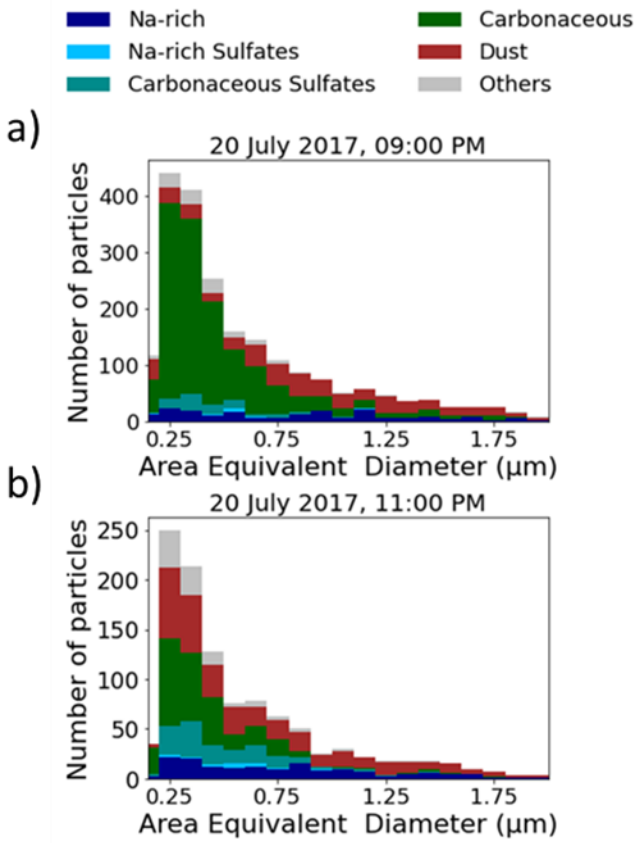

Figure 3-1**:** Number of particles in each class obtained from CCSEM/EDX for samples collected on a) 20 July 2017, 09:00 PM, and b) 20 July 2017, 11:00 PM. The figures show a high fraction of carbonaceous particles, in the lower size bins.

From the tilted view SEM images (from B-films, Figure A.3-6), we observed that out of the total carbonaceous particles, the number fraction of TBs was 55% (218 out of 400) at 9:00 PM, and 38% (53 out of 140) 11:00 PM. On average, the number fraction of TBs was ~50% out of the total carbonaceous particles. Based on the elemental analysis, we classified TBs into two types: (a) inhomogeneously mixed (containing S and K (S+K>0.5%) in addition to C, N, O), and (b) homogeneously mixed (containing only C, N, O and S+K<0.5%) (Figure 3-2). The number fraction of inhomogeneously mixed TBs was about 16%. We hypothesize that inhomogeneously mixed TBs could either have formed through collision of inorganic constituents with liquid tar droplets before they solidified, or organics could have originally condensed onto the inorganic particle before becoming tarry, or the inorganic and liquid tar droplets were emitted almost simultaneously in condensed wildfire smoke [33]. The STXM/NEXAFS analysis shows three prominent peaks (C=C, C-OH and -

COOH) as found by a previous study [34] but different COOH/C=C, and COOH/OH peak ratios. TEM B-film grids were used for STXM/NEXAFS measurement. Based on the peak ratios we observed two different types of TBs, Type 1 TBs with COOH/C=C peak ratio of 2.11 and COOH/COH ratio of 1.57, and Type 2 with a COOH/C=C ratio of 1.19 and COOH/OH ratio of 1.14 (Figure 3-3). Aerosol light absorption properties depend on the fraction of C=C [35]; therefore, the abundance of C=C in different TBs could influence their absorption properties along with other factors such sources and atmospheric transport. TEM lacey film grids were used for STEM/EELS analysis.

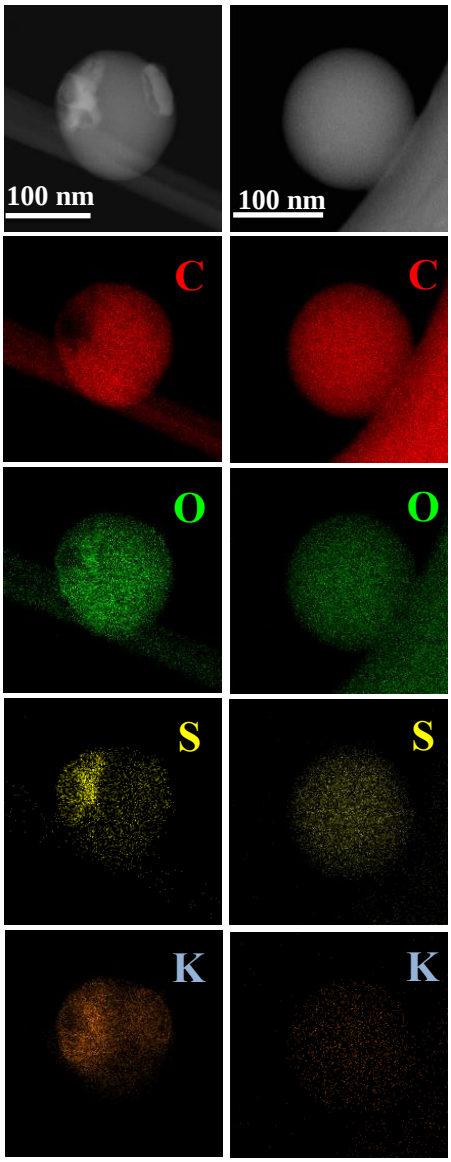

Figure 3-2: Representative STEM/EDX mapping for carbon (C), oxygen (O), Sulfur (S) and Potassium (K) of an inhomogeneously mixed TB (left panel), and b) a homogeneously mixed TB (right panel). The inhomogeneously mixed TB shows heterogeneously distributed S and K within the particle.

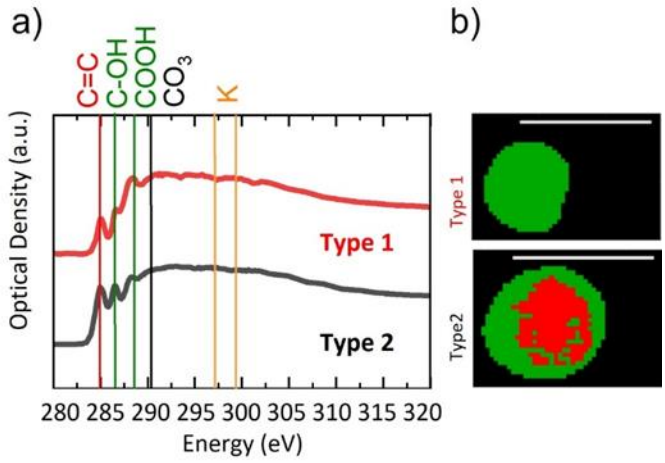

Figure 3-3: a) Representative STXM/NEXAFS spectra showing two types of TBs observed in the sample collected during nighttime. Type 1 TB shows a higher COOH/C=C and COOH/COH peak ratio as compared to type 2 TB. b) Carbon speciation maps. Green represents carboxylic-group rich region and red represents regions with C=C > 35% of total carbon area. The scale bars represent 1 µm.

3.4.2 Refractive index of inhomogeneously and homogeneously mixed TBs

Figure 3-4 (a) shows *m*, for inhomogeneously and homogeneously mixed TBs over the wavelength range from 200 to 1200 nm. We observe only minor differences between inhomogeneously (mean $m = 1.40 \pm 0.05$ at 550 nm) and homogeneously mixed TBs (mean $m = 1.36 \pm 0.07$ at 550 nm). Previously reported values for *m* range from 1.56 [13] to 1.88 [14], significantly higher than what we observed. Our lower values could be due to multiple reasons such as the dry conditions that particles experience under vacuum in STEM [16], variable sources from which the TBs were formed or due to different methods used to estimate the RI of TBs by previous studies. To avoid inaccurate estimation of thickness from the projected area diameter of TBs, we used EELS spectrum along with the Gatan

software to measure the thickness of penetration by the beam. By comparing the thickness of TBs estimated from EELS spectrum to the thickness calculated using the projected area diameter (Figure A.3-7), we observed that when the beam is placed manually at the center of homogeneously and inhomogeneously mixed TBs, errors in the estimated thickness of the TBs are introduced (detailed explanation can be found in Supporting Information).To evaluate the dependence of the refractive index with particle thickness, we calculated the RI by incrementing the thickness of one of the TBs from 131.5 nm (thickness calculated from zero loss peak) to 186 nm (thickness estimated from projected area of the particle) in steps of 10 nm and observed that *m* increases by ~ 3% for a 10 nm increase in thickness (Figure A.3-8). Additionally, since EELs cannot determine the RI of inorganic materials in inhomogeneously mixed TBs we placed the beam away from the inhomogeneous part of the TB and calculated the RI without considering the contribution of S and K rich inclusions. We also estimated the volume averaged RI for inhomogeneously mixed TBs to study the effect of inclusion particle. The volume fraction of TB and potassium sulfate is calculated from the projected area determined using image processing. Considering the inclusions to be potassium sulfate (due to the presence of K and S as in Figure 3-2) (RI = 1.495 – 0i [36]), we estimate an average effective *m* (1.42 ± 0.02) and *k* (0.030 ± 0.002) at 550 nm for inhomogeneously mixed TBs, which are not significantly different from those (*m*=1.40 ± 0.05 and *k*=0.033 ± 0.03) derived directly from EELS away from the inclusion. Hence, from here on we discuss the RI determined from EELS without considering the inclusions.

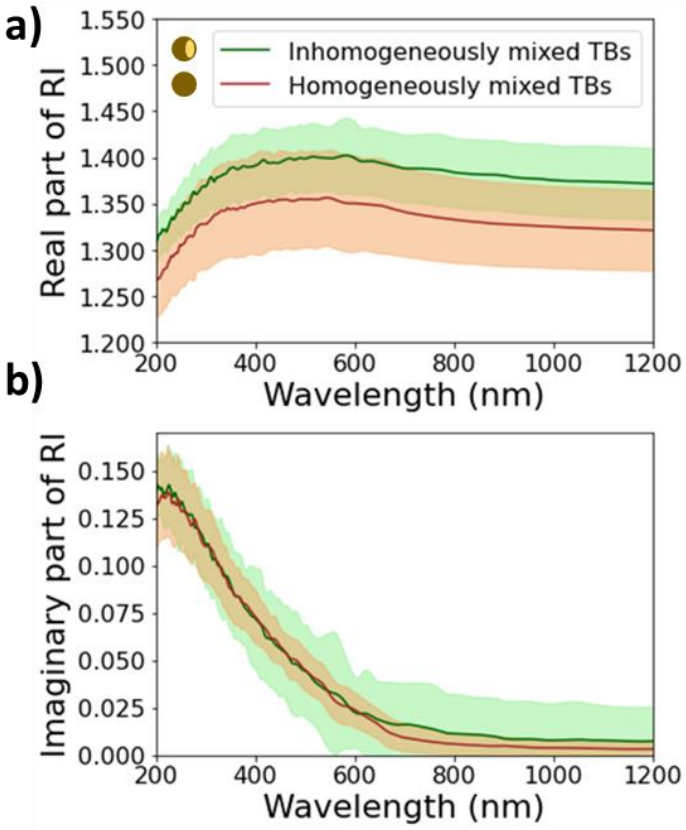

Figure 3-4: Retrieved RI of inhomogeneously and homogeneously mixed TBs. a) The real part of the RI is slightly higher for inhomogeneous TBs as compared to homogeneous TBs. b) The imaginary part of the RI. There are no significant differences between the inhomogeneously and homogeneous TBs. The shaded regions represent 95% confidence intervals of the RI values for all the TBs.

Figure A.3-9 shows the mean dielectric functions Ɛ1 and Ɛ 2 of all the TBs we analyzed, against electron the energy loss as determined using the Kramers-Kronig relationship. The *k* values in the wavelength range from 200 to 1200 nm are shown in Figure 3-4(b). At 550 nm, the averaged *k*, over all inhomogeneously mixed TBs is 0.033 ± 0.03 and for all homogeneously mixed TBs is 0.032 ± 0.02 overlapping within the uncertainty range. Uncertainty represents the 95% confidence intervals of the RI values for all the TBs. Furthermore, the changes in the real and imaginary part of refractive indices for homogeneously and inhomogeneously mixed TBs are not statistically significant, p value from the paired student's t-test is 0.35 for *k* and 0.44 for *m*. This result is consistent with

a previous study where OH aging of β-pinene SOA had no significant effect on *k* due the deactivation of the C-H bonds by adjacent functional groups [37].

Considering the non-significant difference between the RI values of inhomogeneously and homogeneously mixed TBs, from here froward we will focus on averaged RI values. Figure 3-5 compares our overall average *k*, with values reported in previous studies. Alexander et al. used the EELS method to compute *k* for ambient TBs and found a value of ~ 0.28 at 550 nm [16]. Hoffer et al. [17] investigated *k* for laboratory generated TBs from wood tar using European turkey oak and reported a value of 0.21 at 550 nm [17]. In our study, *k* is 0.032 ± 0.02 at 550 nm, 10 times lower than the value reported by Hoffer et al. [17] . The lower *k* found in this study could be due to the different sources from which the TBs were formed or different analytical methods. For instance, the fuel used by Chakrabarty et al [15] was from Boreal forest and the RI were calculated using photoacoustic and nephelometer spectroscopy; Hoffer et al [17] used Turkey oak wood, Black locust, as well as Norway spruce and calculated the RI using nephelometer and continuous light absorption photometer; whereas Li et al[18] used wood tar and calculated RI using broad-band cavity enhanced spectrometer, and Alexander et al. collected TBs from ambient from East Asian-Pacific region and calculated the RI using EELS. Although, it should be noted here that even though Hoffer et al[17] and Chakrabarty et al[15] used similar methods to calculate the RI, their imaginary RI is at least 10 times different. Such large variation in *k* could be due to the different alkene ratios in TBs collected from diverse sources as explained earlier (Figure 3-3).

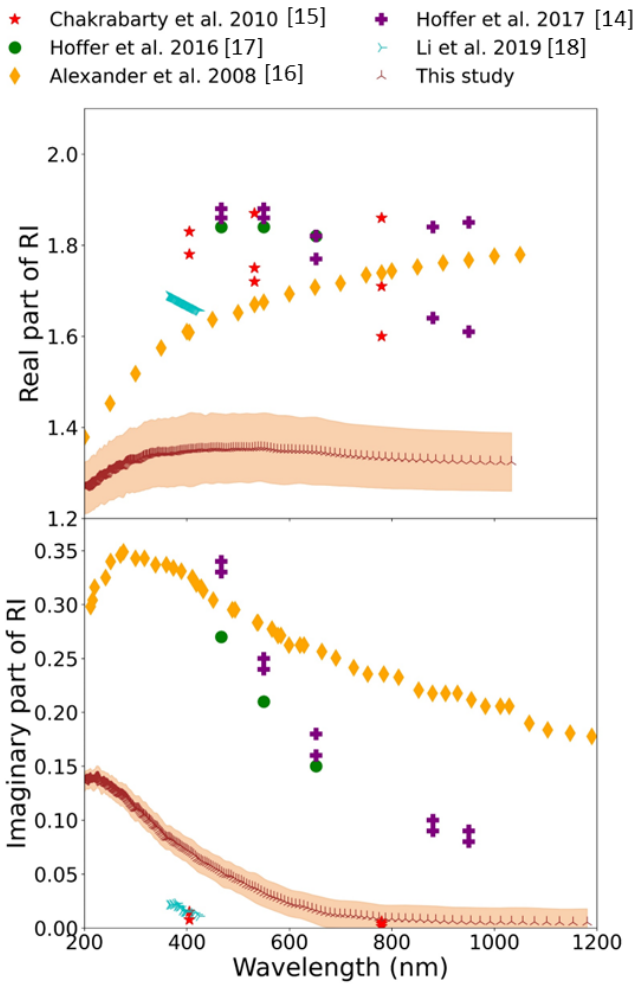

Figure 3-5: Real and imaginary parts of the RI of TBs compared with previously reported values. The *m* reported in our study is lower than, while the *k* is within previously reported values.

3.4.3 Simulated optical properties

To understand the direct effects of TBs in the atmosphere, we used Lorentz-Mie theory to calculate optical parameters such as Q_{abs}, Q_{sca}, AAE, *g*, and SSA. TBs sizes typically range from 50 to 800 nm as reported by previous studies [8, 10, 38, 39] . For example, Tóth et al. found that the mean optical diameter for laboratory generated and ambient TBs is 300 nm [8]. Furthermore, our study shows a maximum SSA for TBs of diameter 350 nm (close to the mean optical diameter). Figure A.3-10 shows the optical parameters calculated assuming a size range from 50 to 800 nm and using our broadband (200-1200 nm) RI values. Q_{abs} is

maximum at 200 nm and decreases very steeply as wavelength increases for all particle diameters (Figure 3-6). At 200 nm Q_{abs} increases from 0.27 for TBs with diameter 50 nm to 1.19 for TB particles with a diameter of 800 nm. A similar trend was observed for BrC particles such as airborne soil organic particles whose absorption efficiency increased from ~ 0.2 for particles with diameter 200 nm to about 1.2 above 800 nm [20].

We also calculated the absorption Ångström exponent (AAE) to be 3.8 in the optical range from λ=380 to 1000 nm, whereas Alexander et al.[16] reported a much lower AAE value of 1.5. Hoffer et al. [17] reported an AAE value ranging between 2.7 and 3.7 for the wavelength range from 467 to 652 nm whereas our AAE was 4.6 over the same wavelength range. The wide range of AAE values underscores the need for further studies to accurately estimate the wavelength dependence of the optical properties of TBs.

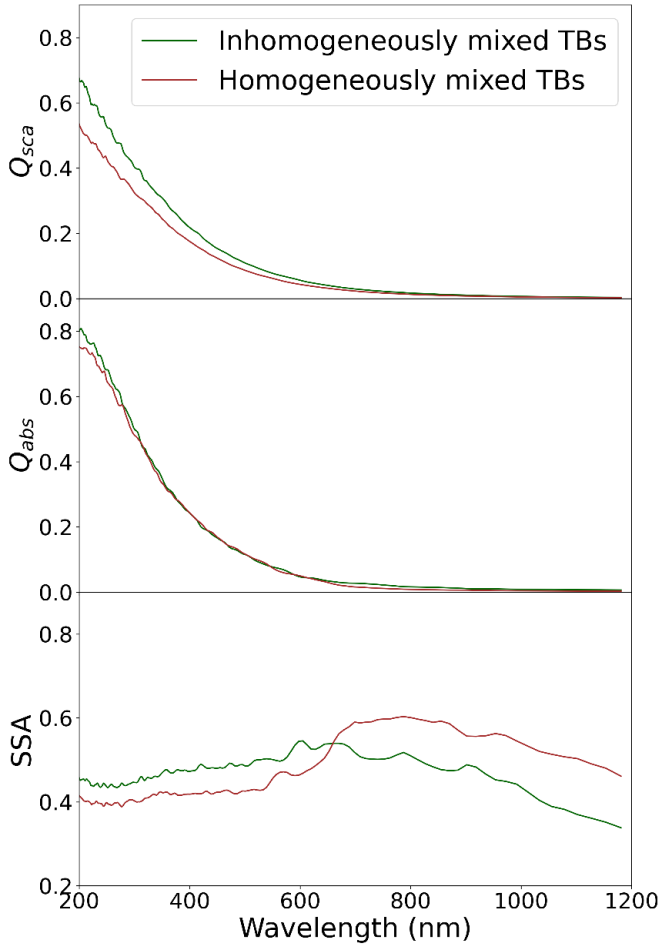

Figure 3-6: Scattering efficiency (Q_{sca}), absorption efficiency (Q_{abs}), and single scattering albedo (SSA) of TBs vs. wavelength calculated using Lorenz-Mie theory for TBs with a diameter of 150 nm.

3.5 Climatic impacts

Several studies observed TBs in the free troposphere with number fractions ranging from 23% [40] to 43% [41]. Qi Yuan et al. studied TBs collected from an elevation of 4276 m a.s.l. on the north slope of the Himalayas and found that TBs could enhance glacier melt due to a positive radiative forcing ranging from +0.01 to 4.06 W/m^2 [42]. Barry et al. investigated ice nucleation properties of TBs from samples collected at an altitude ranging from 3600 m a.s.l to 4600 m a.s.l. and concluded that the presence of TBs could partially explain the enhancement of ice nucleating particle concentrations in many smoke plume passes [40]. Hence, TBs may play a key role in ice nucleation in the free troposphere.

In this study we focus on estimating the direct radiative impacts of aged TBs. To this aim, we calculated the shortwave (0.2 – 4 μm) TOA RF assuming a 100 m thick layer of TBs with a size of 150 nm diameter (equal to the average size of the TBs analyzed in this study) at an altitude of 2165 m. We calculated the TOA RF values for two different surface types (using surface albedo from SBDART for ocean and vegetation [43]) and for clear sky and for two different layerings (TB layer above and below clouds) (Figure 3-7). A 1000 m thick cloud with an optical thickness of 4 was placed at an altitude ranging from 1000 m to 2000 m (for TB layer above cloud) and 3000 m to 4000 m (for TB layer below cloud). Since the aerosol optical depth could vary depending on the emission source, we calculated the TOA RF for optical depth from 0 (representing no aerosol forcing) to 0.1 (high load of TBs) in steps of 0.01.

The TOA RF of TBs above ocean in clear sky conditions ranges from - 0.14 ± 0.03 Wm^{-2} (for an optical depth of 0.01) to - 1 ± 0.32 Wm^{-2} (for an optical depth of 0.1). The uncertainty was calculated from the standard error of RIs of all the 14 individual TBs analyzed in this study. Specifically, upper and lower bounds represent the TOA RFs associated with the optical parameter calculated from the average RI + the standard error, and the average RI - the standard error. We also compared our values with those derived using the refractive indices from Chakrabarty et al. [15] (representing a lower RI bound) and

Alexander et al. [16] (representing an upper RI bound) in the same scenarios. As expected, TBs with the RI from Chakrabarty et al. are more cooling (- 8.9 Wm^{-2} for an optical depth of 0.1) while TBs using the RI from Alexander et al. are more warming (+ 2.4 Wm^{-2} for an optical depth of 0.1). These results underline that the uncertainties in the RI of TBs can lead to large uncertainties in the radiative forcing of TBs and, therefore, on their climatic impacts.

For completeness, we also estimated TOA RF values for cloudy days (Figure 3-7). Regardless of the surface type, we observed that, as expected, clouds below the TB layer increase the warming effect. For instance, above ocean a cloud layer below the TBs layer increased the warming from -1 ± 0.32 (clear sky) to 7.66 ± 0.52 Wm^{-2} (TOA RF calculated using the RI from this study). Also, the case of clouds above TBs, results in enhanced warming, although the effect is milder (+ 4 ± 0.35 Wm^{-2}). Considering the large range of RI values and how these affect not only the value but even the sign of the radiative forcing of TBs, we recommend that further studies should focus on at least two key aspects: (1) compare analytical methods for the calculations of RI on the same TBs population and (2) characterize the optical properties of TBs for specific emission source regions of known and diverse fuel types.

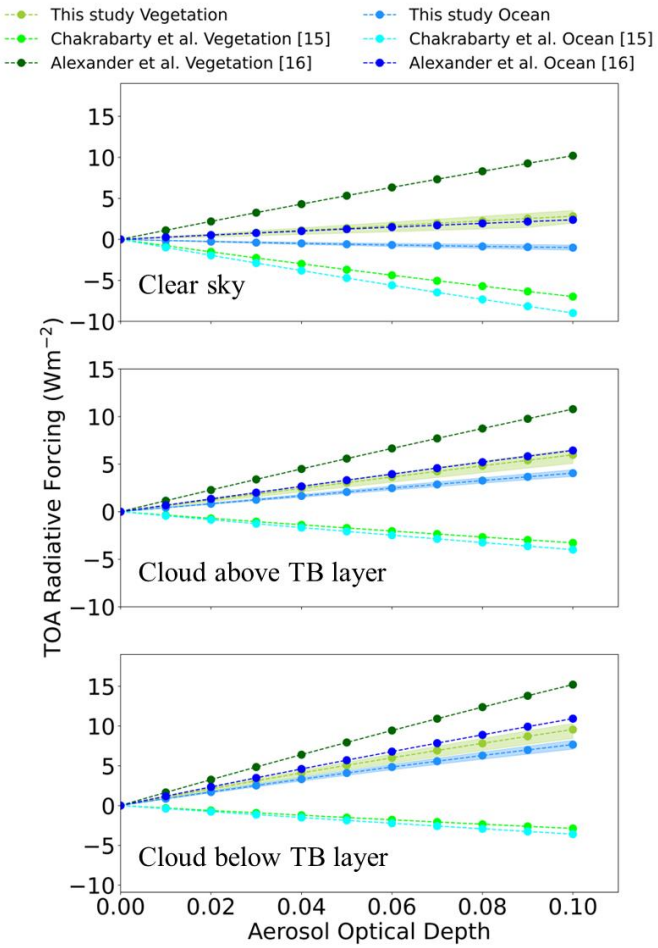

Figure 3-7: TOA RF for an atmosphere with TB layer at an altitude ranging from 2165m to 2265m. TOA RF values were calculated for two surface types (ocean and vegetation). The different lines represent calculations using refractive indices from different studies. The shaded region represents the standard error of TOA RF calculated using the standard error of the RI from our study.

3.6 References

1. Bond, T. C.; Streets, D. G.; Yarber, K. F.; Nelson, S. M.; Woo, J.-H.; Klimont, Z., A technology-based global inventory of black and organic carbon emissions from combustion. *Journal of Geophysical Research: Atmospheres* **2004,** *109*, (D14).
2. Einfeld, W.; Ward, D. E.; Hardy, C., Effects of fire behavior on prescribed fire smoke characteristics: A case study [Chapter 50]. *In: Levine, Joel S., ed. Global biomass burning: Atmospheric, climatic, and biospheric implications. Cambridge, MA: MIT Press. p. 412-419.* **1991**, 412-419.
3. Laskin, A.; Laskin, J.; Nizkorodov, S. A., Chemistry of Atmospheric Brown Carbon. *Chemical Reviews* **2015,** *115*, (10), 4335-4382.
4. Deng, J.; Ma, H.; Wang, X.; Zhong, S.; Zhang, Z.; Zhu, J.; Fan, Y.; Hu, W.; Wu, L.; Li, X.; Ren, L.; Pavuluri, C. M.; Pan, X.; Sun, Y.; Wang, Z.; Kawamura, K.; Fu, P., Measurement report: Optical properties and sources of water-soluble brown carbon in Tianjin, North China – insights from organic molecular compositions. *Atmos. Chem. Phys.* **2022,** *22*, (10), 6449-6470.
5. Zobrist, B.; Marcolli, C.; Pedernera, D. A.; Koop, T., Do atmospheric aerosols form glasses? *Atmos. Chem. Phys.* **2008,** *8*, (17), 5221-5244.
6. Virtanen, A.; Joutsensaari, J.; Koop, T.; Kannosto, J.; Yli-Pirilä, P.; Leskinen, J.; Mäkelä, J. M.; Holopainen, J. K.; Pöschl, U.; Kulmala, M., An amorphous solid state of biogenic secondary organic aerosol particles. *Nature* **2010,** *467*, (7317), 824-827.
7. Liu, J.; Scheuer, E.; Dibb, J.; Ziemba, L. D.; Thornhill, K. L.; Anderson, B. E.; Wisthaler, A.; Mikoviny, T.; Devi, J. J.; Bergin, M.; Weber, R. J., Brown carbon in the continental troposphere. *Geophysical Research Letters* **2014,** *41*, (6), 2191-2195.
8. Tóth, A.; Hoffer, A.; Nyirő-Kósa, I.; Pósfai, M.; Gelencsér, A., Atmospheric tar balls: aged primary droplets from biomass burning? *Atmos. Chem. Phys.* **2014,** *14*, (13), 6669-6675.
9. Pósfai, M.; Gelencsér, A.; Simonics, R.; Arató, K.; Li, J.; Hobbs, P. V.; Buseck, P. R., Atmospheric tar balls: Particles from biomass and biofuel burning. *Journal of Geophysical Research: Atmospheres* **2004,** *109*, (D6).
10. Adachi, K.; Buseck, P. R., Atmospheric tar balls from biomass burning in Mexico. *Journal of Geophysical Research: Atmospheres* **2011,** *116*, (D5).
11. China, S.; Mazzoleni, C.; Gorkowski, K.; Aiken, A. C.; Dubey, M. K., Morphology and mixing state of individual freshly emitted wildfire carbonaceous particles. *Nature Communications* **2013,** *4*.
12. Adachi, K.; Sedlacek, A. J.; Kleinman, L.; Springston, S. R.; Wang, J.; Chand, D.; Hubbe, J. M.; Shilling, J. E.; Onasch, T. B.; Kinase, T.; Sakata, K.; Takahashi, Y.; Buseck, P. R., Spherical tarball particles form through rapid chemical and physical changes of organic matter in biomass-burning smoke. *Proceedings of the National Academy of Sciences* **2019,** *116*, (39), 19336-19341.
13. Hand, J. L.; Malm, W. C.; Laskin, A.; Day, D.; Lee, T.; Wang, C.; Carrico, C.; Carrillo, J.; Cowin, J. P.; Collett Jr., J.; Iedema, M. J., Optical, physical, and chemical properties of tar balls observed during the Yosemite Aerosol Characterization Study. *Journal of Geophysical Research: Atmospheres* **2005,** *110*, (D21).

14. Hoffer, A.; Tóth, Á.; Pósfai, M.; Chung, C. E.; Gelencsér, A., Brown carbon absorption in the red and near-infrared spectral region. *Atmos. Meas. Tech.* **2017,** *10*, (6), 2353-2359.
15. Chakrabarty, R. K.; Moosmüller, H.; Chen, L. W. A.; Lewis, K.; Arnott, W. P.; Mazzoleni, C.; Dubey, M. K.; Wold, C. E.; Hao, W. M.; Kreidenweis, S. M., Brown carbon in tar balls from smoldering biomass combustion. *Atmos. Chem. Phys.* **2010,** *10*, (13), 6363-6370.
16. Alexander, D. T. L.; Crozier, P. A.; Anderson, J. R., Brown carbon spheres in East Asian outflow and their optical properties. *Science* **2008,** *321*, (5890), 833-836.
17. Hoffer, A.; Tóth, A.; Nyirő-Kósa, I.; Pósfai, M.; Gelencsér, A., Light absorption properties of laboratory-generated tar ball particles. *Atmos. Chem. Phys.* **2016,** *16*, (1), 239-246.
18. Li, C.; He, Q.; Schade, J.; Passig, J.; Zimmermann, R.; Meidan, D.; Laskin, A.; Rudich, Y., Dynamic changes in optical and chemical properties of tar ball aerosols by atmospheric photochemical aging. *Atmos. Chem. Phys.* **2019,** *19*, (1), 139-163.
19. Lata, N. N.; Zhang, B.; Schum, S.; Mazzoleni, L.; Brimberry, R.; Marcus, M. A.; Cantrell, W. H.; Fialho, P.; Mazzoleni, C.; China, S., Aerosol Composition, Mixing State, and Phase State of Free Tropospheric Particles and Their Role in Ice Cloud Formation. *ACS Earth and Space Chemistry* **2021,** *5*, (12), 3499-3510.
20. Veghte, D. P.; China, S.; Weis, J.; Kovarik, L.; Gilles, M. K.; Laskin, A., Optical Properties of Airborne Soil Organic Particles. *ACS Earth and Space Chemistry* **2017,** *1*, (8), 511-521.
21. Zhu, J.; Crozier, P. A.; Anderson, J. R., Characterization of light-absorbing carbon particles at three altitudes in East Asian outflow by transmission electron microscopy. *Atmos. Chem. Phys.* **2013,** *13*, (13), 6359-6371.
22. Rinaldi, M.; Santachiara, G.; Nicosia, A.; Piazza, M.; Decesari, S.; Gilardoni, S.; Paglione, M.; Cristofanelli, P.; Marinoni, A.; Bonasoni, P.; Belosi, F., Atmospheric Ice Nucleating Particle measurements at the high mountain observatory Mt. Cimone (2165 m a.s.l., Italy). *Atmospheric Environment* **2017,** *171*, 173-180.
23. Seibert, P.; Frank, A., Source-receptor matrix calculation with a Lagrangian particle dispersion model in backward mode. *Atmos. Chem. Phys.* **2004,** *4*, (1), 51-63.
24. Stohl, A.; Forster, C.; Frank, A.; Seibert, P.; Wotawa, G., Technical note: The Lagrangian particle dispersion model FLEXPART version 6.2. *Atmos. Chem. Phys.* **2005,** *5*, (9), 2461-2474.
25. Laskin, A.; Wietsma, T. W.; Krueger, B. J.; Grassian, V. H., Heterogeneous chemistry of individual mineral dust particles with nitric acid: A combined CCSEM/EDX, ESEM, and ICP-MS study. *Journal of Geophysical Research: Atmospheres* **2005,** *110*, (D10).
26. Moffet, R. C.; Henn, T.; Laskin, A.; Gilles, M. K., Automated Chemical Analysis of Internally Mixed Aerosol Particles Using X-ray Spectromicroscopy at the Carbon K-Edge. *Analytical Chemistry* **2010,** *82*, (19), 7906-7914.
27. Stöger-Pollach, M., Optical properties and bandgaps from low loss EELS: pitfalls and solutions. *Micron* **2008,** *39*, (8), 1092-110.

28. Zhu, J.; Crozier, P. A.; Ercius, P.; Anderson, J. R., Derivation of optical properties of carbonaceous aerosols by monochromated electron energy-loss spectroscopy. *Microscopy and Microanalysis* **2014,** *20*, (3), 748-759.
29. Egerton, R. F., *Electron energy-loss spectroscopy in the electron microscope*. Springer Science & Business Media: 2011.
30. Ricchiazzi, P.; Yang, S.; Gautier, C.; Sowle, D., SBDART: A Research and Teaching Software Tool for Plane-Parallel Radiative Transfer in the Earth's Atmosphere. *Bulletin of the American Meteorological Society* **1998,** *79*, (10), 2101-2114.
31. Ott, L., GEOS-Carb CASA-GFED Daily Fire and Fuel Emissions 0.5 degree x 0.5 degree V3. In Goddard Earth Sciences Data and Information Services Center (GES DISC): Greenbelt, MD, USA, 2020.
32. EDGAR, EDGAR - Emissions Database for Global Atmospheric Research. In 2023.
33. Li, J.; Pósfai, M.; Hobbs, P. V.; Buseck, P. R., Individual aerosol particles from biomass burning in southern Africa: 2, Compositions and aging of inorganic particles. *Journal of Geophysical Research: Atmospheres* **2003,** *108*, (D13).
34. Tivanski, A. V.; Hopkins, R. J.; Tyliszczak, T.; Gilles, M. K., Oxygenated Interface on Biomass Burn Tar Balls Determined by Single Particle Scanning Transmission X-ray Microscopy. *The Journal of Physical Chemistry A* **2007,** *111*, (25), 5448-5458.
35. Bond, T. C.; Bergstrom, R. W., Light Absorption by Carbonaceous Particles: An Investigative Review. *Aerosol Science and Technology* **2006,** *40*, (1), 27-67.
36. Weast, R. C.; Suby, S.; Hodman, C., Handbook of Chemistry and Physics. 64. *Aufl.(CRC-PRESS, Boca Raton, FL, 1985)* **1984**.
37. He, Q.; Tomaz, S.; Li, C.; Zhu, M.; Meidan, D.; Riva, M.; Laskin, A.; Brown, S. S.; George, C.; Wang, X.; Rudich, Y., Optical Properties of Secondary Organic Aerosol Produced by Nitrate Radical Oxidation of Biogenic Volatile Organic Compounds. *Environmental Science & Technology* **2021,** *55*, (5), 2878-2889.
38. Fu, H.; Zhang, M.; Li, W.; Chen, J.; Wang, L.; Quan, X.; Wang, W., Morphology, composition and mixing state of individual carbonaceous aerosol in urban Shanghai. *Atmos. Chem. Phys.* **2012,** *12*, (2), 693-707.
39. Pósfai, M.; Simonics, R.; Li, J.; Hobbs, P. V.; Buseck, P. R., Individual aerosol particles from biomass burning in southern Africa: 1. Compositions and size distributions of carbonaceous particles. *Journal of Geophysical Research: Atmospheres* **2003,** *108*, (D13).
40. Barry, K. R.; Hill, T. C. J.; Levin, E. J. T.; Twohy, C. H.; Moore, K. A.; Weller, Z. D.; Toohey, D. W.; Reeves, M.; Campos, T.; Geiss, R.; Schill, G. P.; Fischer, E. V.; Kreidenweis, S. M.; DeMott, P. J., Observations of Ice Nucleating Particles in the Free Troposphere From Western US Wildfires. *Journal of Geophysical Research: Atmospheres* **2021,** *126*, (3), e2020JD033752.
41. Dzepina, K.; Mazzoleni, C.; Fialho, P.; China, S.; Zhang, B.; Owen, R. C.; Helmig, D.; Hueber, J.; Kumar, S.; Perlinger, J. A.; Kramer, L. J.; Dziobak, M. P.; Ampadu, M. T.; Olsen, S.; Wuebbles, D. J.; Mazzoleni, L. R., Molecular characterization of free tropospheric aerosol collected at the Pico Mountain Observatory: a case study

with a long-range transported biomass burning plume. *Atmos. Chem. Phys.* **2015,** *15*, (9), 5047-5068.
42. Yuan, Q.; Xu, J.; Liu, L.; Zhang, A.; Liu, Y.; Zhang, J.; Wan, X.; Li, M.; Qin, K.; Cong, Z.; Wang, Y.; Kang, S.; Shi, Z.; Pósfai, M.; Li, W., Evidence for Large Amounts of Brown Carbonaceous Tarballs in the Himalayan Atmosphere. *Environmental Science & Technology Letters* **2021,** *8*, (1), 16-23.
43. Chiu, J. C.; Marshak, A.; Knyazikhin, Y.; Wiscombe, W. J., Spectrally-invariant behavior of zenith radiance around cloud edges simulated by radiative transfer. *Atmos. Chem. Phys.* **2010,** *10*, (22), 11295-11303.

4 Haze Processing of Aerosol during Wintertime in the Indo-Gangetic Plains

4.1 Abstract

Haze impacts visibility, health as well as climate. Haze processing of aerosol particles can impact mixing state, phase state and their ability to absorb sunlight. Variability in mixing state of atmospheric aerosols contributes significantly to uncertainties associated with the estimated radiative forcing. In this study, we investigate haze processing of aerosol particles during wintertime from the Indo-Gangetic plain, which is polluted by industries and other household activities. We applied multi-modal micro-spectroscopy techniques to determine single particle composition and bulk mass spectrometry techniques to determine molecular composition of organic aerosols. Single particle analysis revealed an abundance of potassium-rich sulfates. Tilted view imaging showed that most of the organic particles with inorganic inclusion had low viscosity. Organic compounds mixed with inorganic salts within the same particle affect the hygroscopicity of the aerosols and hence impact their ability to act as cloud condensation nuclei.

4.2 Introduction

Haze reduces visibility to less than 10 km due to the high accumulation of fine aerosols [1]. Haze has adverse effects on human health, climate, and the environment [2]. Severe haze is a major concern all around the world such as in France [3], China [4], Mexico city [5], and India [6]. The northern parts of India and China often experience severe haze, typically during winter when particle mass concentrations are as high as several hundred μg/m^3. The Indo-Gangetic plain (IGP) that includes most of the northern regions of the Indian subcontinent (~21% of land area) is one of the most populated and polluted regions in the world [7]. The area is polluted by a wide range of anthropogenic activities such as biomass and fossil fuel burning, industries, transport, mining, agricultural, and urbanization activities [7]. The polluted air can have contributions from the state of Bihar which contains a large number of coal mines, iron and steel industries that lie west and northwest of the sampling location [8]. Haze occurrence during winter increases at a rate of about 2.6 days per year over central India and about 1.7 days per year in the Indo-Gangetic plain (IGP) [9]. Biomass burning,

such as wildfires, agricultural burning, and household burning, is a common pollution source, especially during winter in rural areas. For example, in the city of Kolkata, situated in the IGP, the estimated atmospheric particulate matter ($PM_{2.5}$) is 100 $\mu g/m^3$ during winter, comparable to other highly polluted cities in India such as Delhi [10].

Unraveling the chemical composition of aerosols during winter haze episodes in the IGP region is an active area of research. Several studies highlighted that a major fraction of atmospheric PM consists of carbonaceous and water-soluble inorganic components [11, 12]. Particles are often internally mixed; for example, potassium (K) and sulfur (S) rich particles are coated with organics [13]. Under high relative humidity conditions during haze episodes, the aerosol undergoes both physical and chemical transformations due to aqueous phase chemistry [14]. Enhanced formations of water-soluble secondary inorganic aerosols such as sulfates, nitrates, ammonium, and secondary organic aerosol (SOA) are observed due to meteorological conditions in this region such as low wind speed, frequent temperature inversions, high humidity, and shallow boundary layer [12, 15].

Phase state refers to the aerosol physical characteristic of being solid, semi-solid, or liquid, and it can change depending on environmental conditions like relative humidity and temperature. Inorganic components (e.g., SO_4^{2-}) can increase the hygroscopicity of the particles and at elevated relative humidity, enhance the water uptake of aerosols changing the particle phase state [16]. With increasing relative humidity, the viscosity of organic material decreases and the particles becomes liquid-like [17]. For example, organosulfates (OSs) are important SOA constituents derived from oxidation of biogenic (e.g., α-pinene, isoprene) and anthropogenic (e.g., industrial emissions, biomass burning) volatile organic compounds and with relatively higher water uptake, OSs can influence phase transition of ambient aerosols. The phase state and volatility of the aerosols impact the gas-particle diffusion rates and play a major role in influencing heterogeneous reactions, particle growth, and cloud condensation nuclei concentrations [18], thereby impacting the aerosol optical depth [19].

Most of the studies from the IGP region focused on the chemical composition of bulk aerosols samples collected during haze episodes, but there is only a limited number of studies [20-22] that report size-resolved elemental and molecular composition during winter

haze periods. Given the dense urbanization in the IGP, acidic sulfate (SO_4^{2-}) and nitrate (NO_3^-) are consistently produced via atmospheric oxidation of SO_2 (g) and NO_x emitted from anthropogenic activities such as vehicles' driving, coal/oil refining, and brick kiln production[23]. In particular, 2-methyltetrol diastereomers (2-MTSs) have been extensively observed in isoprene-enriched environments under significant anthropogenic influence, contributing up to 13 % of the organic carbon in aerosols [24-26]. Coupled with IGP's unique topography and meteorological drivers, the regional diversity of emitted pollutants [27, 28] makes the characterization of particulate matter in this region challenging. Additionally, molecular characterization of OSs remains difficult due to the complexity of SOA matrix and analytical challenges in distinguishing OSs from inorganic sulfates [29]. Furthermore, we have limited understanding of the aerosol phase state and volatility distribution under these atmospheric conditions with high aerosol loading. Hence, field observations are needed to understand how atmospheric processing alters the phase state, mixing state, and volatility of the particles and their potential impact on the atmospheric environment [30].

In this study, we investigate the chemical composition of individual particles as well as the molecular composition of bulk organic aerosol from a highly polluted region in the IGP under hazy conditions during wintertime. We utilize multi-modal chemical imaging techniques to probe the chemical composition of individual particles and high-resolution mass spectrometry to investigate the molecular composition of the bulk organic aerosol. While the characterization of molecular formulae (MFs) in ambient aerosols can be challenging due to the complex SOA matrix and lack of authentic standards [31], heated electrospray ionization coupled with high-resolution mass spectrometry (HESI-HRMS) offers broad mass coverage with high accuracy and greater resolution ($>10^6$) [32-35] . Combined chemical imaging and HRMS analysis allow us to investigate the phase state and volatility of the different particle types. The goal of this study is to understand the haze processing of aerosol particles during wintertime, information which can help policy makers to improve the air quality and modelers to improve climate models.

4.3 Experimental methods

4.3.1 Sampling site and sample collection

This study was conducted in the eastern side of the Indo-Gangetic Plain (IGP) (23°24´N, 87°02´E) in West Bengal, India. Samples were collected during the winter season of the year 2018 between January 2 to January 10 using a four-stage Sioutas Cascade Impactor (SKC). Particles were collected on substrates placed on the D stage (< 0.25 µm, aerodynamic diameter) and C stage (0.50- 0.25 µm). Particles were collected on TEM grids (Copper 400 mesh grids coated with Carbon Type-B and lacey films, Ted Pella) and silicon nitride substrates (Silson). This study analyzed a set of seven samples from both stages C and D, a total of 14 samples, noted as S1, S2, S3, S4, S5, S6 and S7. We combined particles from stages C and D for each sample. Furthermore, bulk aerosol samples were collected on Teflon filters during the morning and afternoon of January 09 as a case study. The sampling days (Table B.1-1) were found to be hazy as reported by the nearest meteorological station and according to the Hybrid Single-Particle Lagrangian Integrated Trajectory (HYSPLIT) analysis and meteorological data. The HYSPLIT analysis shows that, the air masses were mainly transported through a foggy atmosphere over the IGP. Hence the particles experienced fog processing as they reached the location where the samples were collected. In addition to the long-range transported aerosols, there should be influences from local sources such as biomass burning from fields, household use of fuels, and vehicular exhausts.

4.3.2 Micro-spectroscopy analysis of particles

The elemental composition and morphology of the particles in each sample were determined using computer-controlled scanning electron microscopy with energy dispersed X-ray analysis (CCSEM/EDX) [36]. The analysis was conducted using an environmental scanning electron microscope (FEI Quanta). The microscope uses an EDAX X-ray spectrometer with a Si(Li) detector with an active area of 10 mm^2 and an ATW2 window. The X-ray spectra acquired using the EDAX detector provided the elemental composition of the particles in the samples. The CCSEM/EDX was operated with a beam current of 500 pA and an accelerating voltage of 20 kV. Based on the elemental composition obtained from CCSEM/EDX, particles were classified into eight groups

(details in SI) such as Na-rich, Na-rich sulfates, Si-rich sulfates, carbonaceous-sulfates, K-rich sulfates, carbonaceous particles, and dust (Figure B.1-1). At least 1000 particles from each sample were analyzed. Overall, we analyzed 16,982 individual particles in this study.

To understand the phase state of individual particles collected each day, we subdivided the organic particles into two categories as (a) particles with inclusion and (b) particles without inclusion (Figure B.1-2). Using tilted angle transmission electron microscopy, the deformation of the particles upon impaction on the substrate was determined by calculating the aspect ratio of the particles [37] calculated as the ratio between the height and the width of each particle (Figure B.1-2). The aspect ratios were calculated for each sample except for S3, and S6 for which images were unavailable because the samples were damaged after initial analysis.

Scanning transmission X-ray microscopy along with near-edge X-ray absorption fine structure spectroscopy (STXM/NEXAFS) was utilized to determine the mixing state and carbon functionalities [38]. The transmitted X-ray beam through the sample was acquired at different energies and converted to an optical density (OD). Based on the observed absorption peak the functional groups of particles in different mixing state groups were identified. We acquired STXM maps at 11 different energies of the carbon K-edge ranging from 278 to 320 eV and carbon spectra were acquired by capturing a stack of images at 111 energies in the same range (278-320 eV).

4.3.3 High-resolution mass spectrometry analysis of aerosol

The molecular composition of aerosol particles was determined using a 12 T Fourier Transform Ion Cyclotron Resonance Mass Spectrometer (FTICR MS; Bruker SolariX) ; the design of the instrument and implementation of the analytical method are described elsewhere [39]. Briefly, HRMS experiments were performed by negative electrospray ionization (ESI). Mass analysis range varied from m/z 100- 1000 with a mass resolution of >450,000 at m/z 400. Other instrumental conditions were: (a) mass injection time of 200 ms, (b) automatic gain control (AGC) set at 10^6, (c) capillary temperature at 275 ℃, and (d) ESI spray voltage at 4.5 kV. Using volatility parameters, individual molecular formulas

were classified as volatile organic carbon (VOC), intermediate VOC (IVOC), semi VOC (SVOC), low VOC (LVOC), or extremely low VOC (ELVOC).

4.4 Results and discussion

4.4.1 Size-resolved particle composition and particle classes during wintertime

Out of total number of particles, we observed a high abundance (40 – 70%) of sulfate-containing particles in most of the samples. K-rich sulfate particles are most dominant (Figure 4-1), followed by Si-rich sulfates, carbonaceous sulfates, and Na-rich sulfates respectively. The number fraction of K-rich sulfates ranges from 10 - 40%. Si-rich sulfates are dominant in larger particle sizes, with 20 – 40% of Si-rich particles in the size range of 1-4 µm. The abundance of K and Si-rich sulfates indicates the contribution of secondary aerosols from biomass burning as well as fossil fuel [40]. K-rich sulfate particles are tracers of biomass burning and fossil fuel emissions. The aerosols emitted from biomass burning were found to be very rich in K^+ and Cl^- ions [41]. These KCl particles present in the fresh smoke plumes of biomass burning transform into K_2SO_4 as part of aging in the atmosphere [42]. Si-rich sulfates could be formed from the hydrated Si-rich minerals reacting with SO_2 emitted from coal combustion or agricultural burning.

Na-rich sulfates are present in smaller particles accounting for 10 to 20% of the total number of particles in all samples except S6 (< 10%). Na is mostly emitted from sea spray and fungal spores, other anthropogenic sources of Na include soil, refuse incineration, oil combustion, coal combustion, car exhaust, and industrial pollution [43]. The presence of carbonaceous sulfates is very low (~ 5%) in S1, S2, S5, and S7 but substantially higher in S3 and S6 accounting for ~ 40 – 50 % of the total particle fraction which indicates secondary organic aerosol formation. Furthermore, in the S3 and S6 samples, the K-rich sulfate is less than 20%. In almost all samples there is a high fraction of K-rich sulfates, with the next most abundant species being carbonaceous particles such as soot, tarballs, and low viscous organic aerosols, with a minor fraction of Na-rich particles and dust (Figure 4-1).

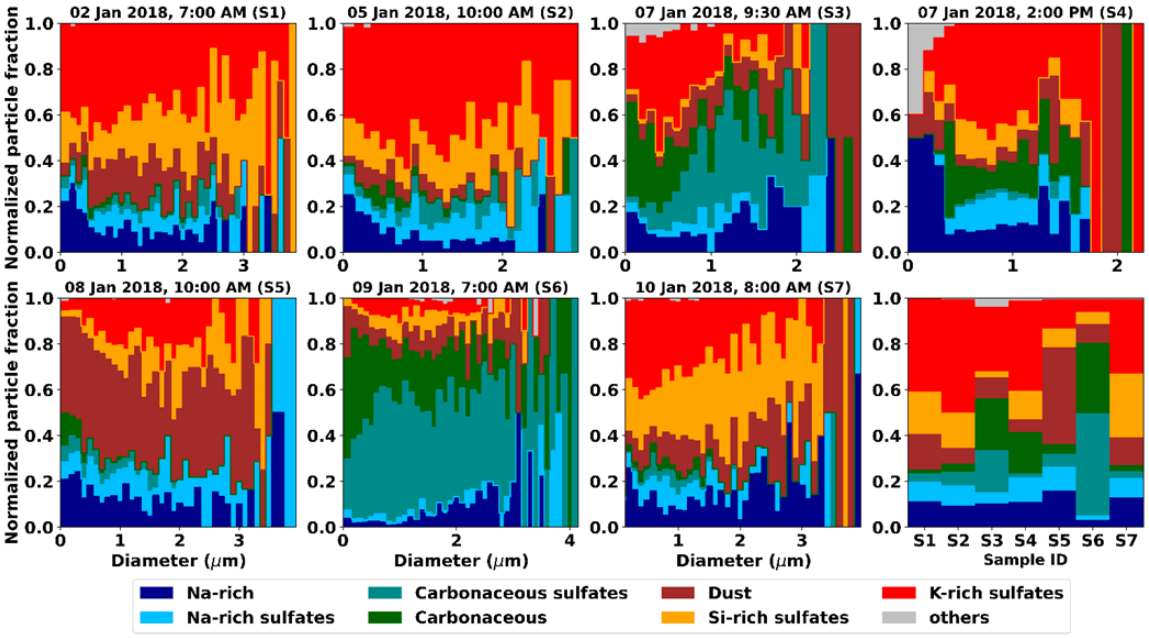

Figure 4-1: Normalized particle number fraction for each particle class with respect to the area equivalent diameter for each sample. The last panel represents a summary plot showing particle fractions averaged over all the diameters.

High sulfate content in the particles is consistent with haze conditions as shown in previous studies [44, 45] that reported enhancements of sulfur from non-hazy to hazy days. For instance, an enhancement ratio of 5.4 was observed for sulfates from a non-hazy to the hazy period over North China [44]. Sulfate formation can be very common under hazy conditions through several pathways, for example, the sulfur oxidation in the aqueous phase by hydrogen peroxide and ozone occurs much more rapidly than oxidation by OH radicals in the gas phase [46]. Metal catalyzed oxidation is another pathway to sulfate formation during haze events, for example, droplets containing dissolved Mn^{2+} absorb SO_2 at the surface and form sulfates [47]. Non-carbonaceous particles absorb water vapor and wet the particle surface. SO_2 emitted from coal combustion is absorbed into the wet layer forming H_2SO_4 [48]. This could lead to the formation of different non-carbonaceous sulfates observed in our samples. The crystalline-shaped Na-rich particles found in the samples could be NaCl or $NaNO_3$ particles formed by the reaction between NaCl and nitric acid. These Na-rich particles react with particulate H_2SO_4 to form Na-rich sulfates [49].

Apart from sulfates, we also observed Na-rich particles which constitute only about 10% of the particle fraction. The particle fraction remains the same throughout the samples (Figure 1). The presence of Na-rich particles could be due to influences from the sea. We also observe about 15 to 20% of dust particles in samples S1, S2, S3, S4, S6, and S7. But in S5, there is a significant increase in the fraction of dust particles to about 40% and very few carbonaceous components (<10%) (Figure 4-1). In sample S5 dust particles are mostly either Si-rich or Fe-rich. The Fe-rich dust particles are smaller in size as compared to Si-rich dust particles. A previous study suggests that the most abundant Fe-bearing particles in East Asia is fly ash which contains combustion-generated refractory material along with a significant amount of Si [50]. As shown in Figure B.1-2, Fe-rich dust particles have very low Si content. Such Fe-rich mineral dust is ubiquitous over East Asia during an Aeolian dust outflow event and can significantly impact the radiative forcing due to its strong absorption according to previous studies [50].

4.4.2 Sulfate formation during haze

This study region is influenced by both agricultural biomass burning and anthropogenic sources. Therefore, we investigated sulfate formation pathways to understand contributions from different sources. In a study by Li et al. haze was classified into two types depending on humidity and source [42]. Type 1 haze was formed from aerosols emitted from agricultural biomass burning and had particles larger than type 2 haze which was formed from anthropogenic sources such as industrial pollution, transportation, and cooking. When they plotted the weight percentage of K against the weight percentage of S, haze formed due to agricultural burning showed a higher percentage of K with respect to S than what was present in laboratory-generated potassium sulfates due to abundant KCl particles present in fresh plumes of biomass burning. Similarly, to understand the major source of haze formation in our samples, we plotted the weight percentage of K against that of S for particles that were classified as potassium sulfate. According to Li et al. study [42] our results suggest that the major source for haze formation in the region of our study is anthropogenic pollution (Figure 4-2) with a high fraction of S.

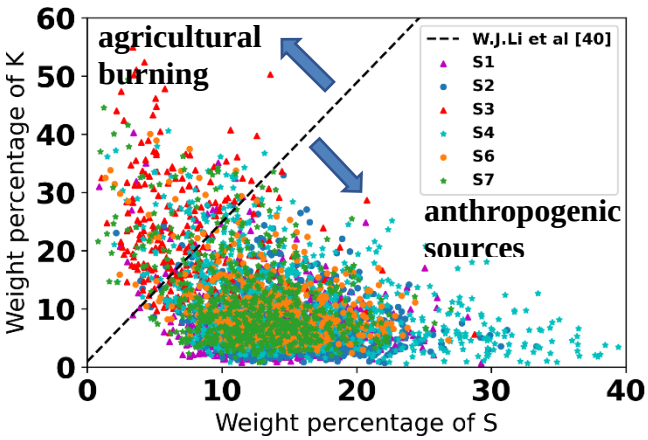

Figure 4-2: Weight percentage of potassium with respect to that of sulfur for particles in the K-rich sulfate class. The dashed line represents the weight percentage of K and S for laboratory-generated K_2SO_4 from Li et al.[42]

K-rich sulfate is the most abundant component in all our samples. Typically K is emitted as potassium chloride (KCl) into the atmosphere from fresh biomass burning plumes and undergo heterogeneous reactions to form potassium sulfates and nitrates, as discussed in the previous section [51]. EDS mapping of particles in our samples shows that K and S are concentrated in small regions of the particles surrounded by carbon, oxygen, and nitrogen elements. This suggests a core-shell mixing state where potassium sulfates are coated by organic material.

Organosulfates (OS) and nitrooxy-OSs are characteristic of severe haze episodes usually originating from anthropogenic precursors [52] . Table B.5-1 summarizes the wide range of reported OS and nitrooxy-OS found in haze during wintertime across urban China and in recent work [35, 52-55]. Figure 4-3 shows van Krevelen plots for the particles' organic fraction characterized by nano-DESI-HRMS from morning and afternoon samples collected under haze conditions. The mass abundance plot corresponding to both sampling periods is shown in Figure B.5-1 (SI). The identified MFs are classified into four groups: CHO, CHOS, CHNO and CHNOS. The inset pie plot in Figure 4-3, reflects the distribution of each MF uniquely found in each sampling condition. Based on the distribution, up to 33% of CHOS and 10% of CHNOS are identified in a total of 5624 MFs in the morning. While, up to 9% of CHOS and 36% of CHNOS are assigned from a total of 1637 MFs in the

afternoon. Given the mass distribution of detected species (Figure S7), organosulfates (OS) were largely present in the morning, while high abundant nitrooxy organosulfates (CHNOS) were mostly observed in the afternoon.

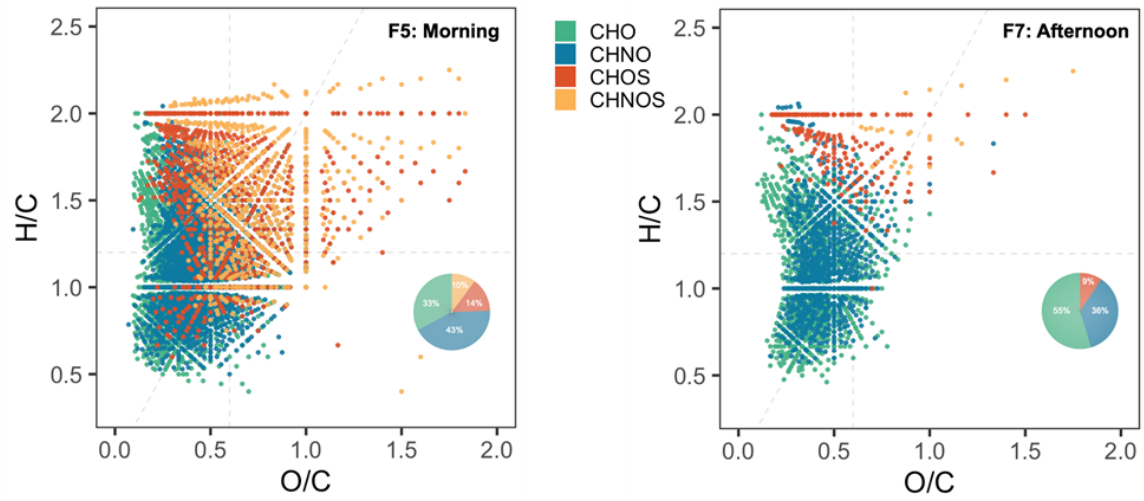

Figure 4-3: Van Krevelen diagrams for unique molecular fractions in each sampling period. The inset pie chart shows distribution of molecular formulae unique to each condition. Marker color distinguishes the class of identified molecular formulae.

Amongst several identified OSs and nitrooxy-OSs, a few showed noticeable trends. In particular, O7S ($C_9H_{15}O_7S^-$) showed high abundance in both morning and afternoon. OS7 is one of the unique OS, which has been previously observed in ambient cloud/fog water and free tropospheric biomass burning organic aerosol [39, 55-57] (Table B.5-1, SI). In the work of Cai et al., O7S was found to be dominant in summertime while Bryant et al. [58] showed an 8-fold enhancement in O7S during wintertime. Since, O7S is predominantly found in daytime in our study, we infer that O7S is originating from photochemical oxidation of monoterpenes [35] (e.g., Limonene or Isoprene).

Nitrooxy-OSs can contribute up to 10% of the organic aerosol fraction [59, 60]. Amongst the nitrooxy-OSs exclusively observed in the morning sample (C10H18NO9S-, $C_{10}H_{16}NO_9S$-, C12H22NO9S- and C12H22NO8S-), C10H16NO9S- was found with the highest peak signal [61]. This monoterpene derived product [35] has been often observed at enhanced levels in urban aerosols during wintertime as well as in fog water samples [58, 62].

Figure 4-4 demonstrates the volatility distribution of the unique MFs for each of our sampling period as a function of m/z. The degree of unsaturation [52] in the identified MFs was explored by examining double bond equivalence (DBE) vs Carbon (C) number as shown in the inset. The volatility distribution shows that up to 3492 species were classified under the extremely low volatile organic compounds (ELVOCs)region in comparison to the 640 MFs for morning and afternoon samples, respectively. Based on the inset DBE plot, the identified CHOS and CHNOS in the morning and afternoon samples contained particles more saturated and likely produced via oxidative atmospheric processing [35]. Additionally, most of the observed CHOS and CHNOS in the morning samples predominantly exist as ELVOCs (Table B.5-1), indicating that S-containing species are likely in the condensed (solid or liquid) phase.

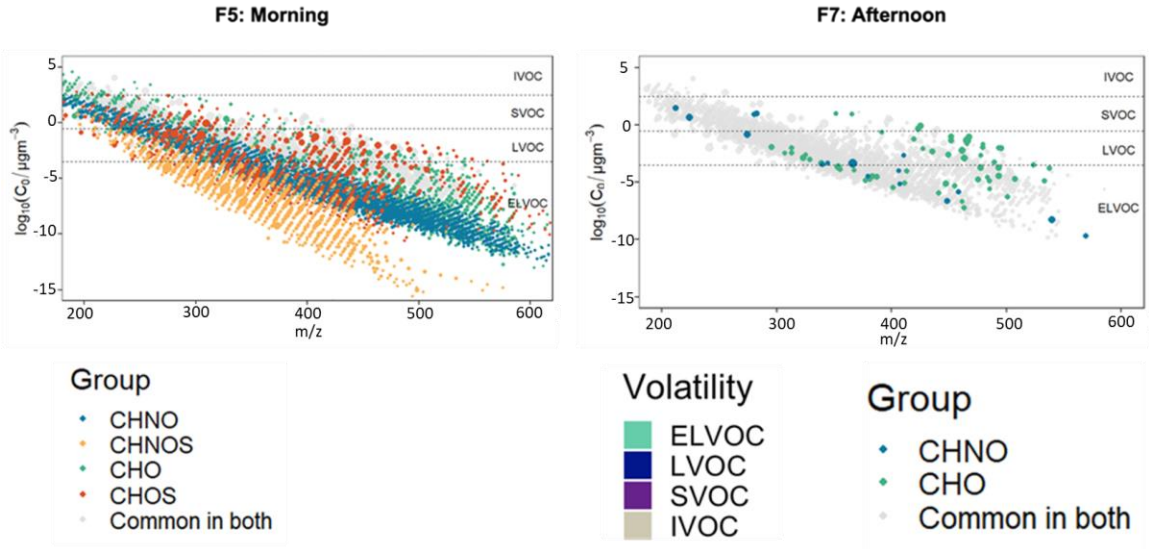

Figure 4-4: Logarithmic distribution of saturation mass concentration (C_0) in the samples against the mass to charge ratio (m/z) for different sampling periods: morning (F5) and afternoon (F7). The color of markers differentiates between functional groups unique in each sample, while grey markers indicate common features amongst both periods. The size of the markers corresponds to the normalized abundance. The insets represent double bond equivalence variation with respect to C number for each of the identified molecular formulae in each sampling period. Datapoints are sized according to their abundance.

4.4.3 Chemical imaging and mixing state of particles.

Overall, carbonaceous particles and K-rich sulfates are the most abundant particle classes during our study. Carbon functionalities of particles are studied using STXM/NEXAFS for two samples (S2 and S7) out of the seven samples due to limited STXM/NEXAFS use time availability. We selected samples S2 and S7 because they contain a significant number of particles from all the identified classes enhancing the probability to capture different types of particles using STXM/NEXAFS. The STXM/NEXAFS analysis was used to understand the influence of inorganic material mixing with carbonaceous particles on their phase state. Figure 4-5 shows representative NEXAFS spectra and maps of particles with four distinct mixing states. The peak at 288.5 eV indicates the presence of the carboxylic functional group, which can take up water and decrease the viscosity of the particles. In the carbon mixing state maps, the red color represents the sp^2, green the organic, and teal the inorganic dominated regions. Out of the total number of particles, in sample S7 OCEC (elemental C mixed with organic mass) accounts for about 35% of the total particle fraction whereas S2 accounts for only 20% of the total particles in the OCEC mixing state (Figure 4-4). An abundance of alkene groups in the particles represents black carbon or soot emitted from fossil fuel or vegetation combustion [36, 37]. Moreover, sample S2 contains about 30 % of particles with the OCInEC (particles containing mixtures of organic mass, elemental carbon and inorganic inclusions) mixing state whereas the S7 contains only less than 20 % of OCInEC. Further analysis to explain the phase state of the particles in different samples is discussed in the following section.

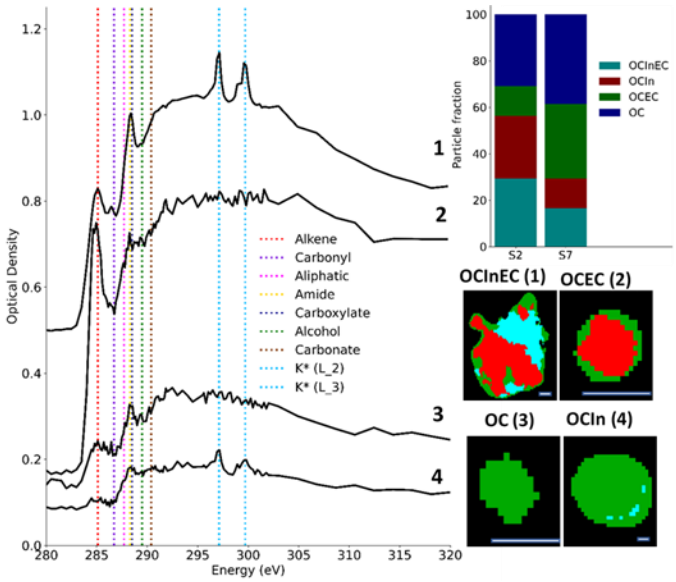

Figure 4-5: Representative STXM/NEXAFS spectra for different particle types. Red represents sp^2 dominated region, the organic region is shown in green, and teal represents the inorganic region. Dotted lines show peaks corresponding to the energies of different functional groups. The scale bar is 0.5 µm.

4.4.4 Phase state of the particles for different mixing states

Atmospheric organic particles exist in solid, semi-solid, or liquid phase states [38]. The viscosity of the particles was studied using tilted view images from SEM. The deformation of a particle upon impact depends on its viscosity and phase state. Solid particles undergo the least deformation as compared to liquid particles [39]. Hence, liquid particles spread on the surface increasing particle width and decreasing the aspect ratio (Figure B.1-2). Based on the aspect ratio boundaries from a previous study, particles were grouped as solid (AR 0.76 to 1), semi-solid (AR between 0.54 and 0.76) and liquid (AR below 0.54) [22].

The tilted view images from SEM show an abundance of liquid-like particles in all the samples. TEM images in Figure 4-6 shows that liquid particles have inclusions while solid particles have no inclusions. Hence, we classified the particles into two groups as with and without inclusions. Particles with inclusions have an aspect ratio of less than 0.3 in most of the samples, suggesting an abundance of liquid particles. Whereas particles without inclusions exist in all three phase states with most of the particles in solid or

semi-solid states. Solid organic particles in the samples were mostly spherical carbonaceous particles with high resistance to the SEM electron beam often referred to as 'tar balls' [40].

We also investigated the phase state of two samples collected at slightly different humidity conditions, S2 (RH 43%), and S7 (RH 38%) using STXM data. The total carbon absorption (TCA) from STXM depends on the pathlength X-ray photons travel through the particle and is used to estimate the particle phase state [41]. The threshold values for TCA to classify the particles into solid, semi-solid, and liquid states were obtained from a previous study [37]. Figure 4-6c shows that organic particles with inorganic mixing (OCInEC and OCIn) are mostly in the liquid state. OCIn and OCInEC account for more than half of the particle fraction (~ 55 %) in S2, whereas they account for only ~35 % of the total particle fraction in S7. Previous laboratory studies suggest that when the inorganics that are hygroscopic are internally mixed with organics, they enhance the overall hygroscopicity of the particle[42, 43]. Moreover, a few field studies also report a decrease in viscosity of the particles due to the presence of inorganics[43, 44]. For instance, a field study by Slade et al. 2019 using the University of Houston Mobile Air Quality Laboratory reports a decrease in viscosity of the particles due to higher sulfate fraction during daytime. Hence, our observation is consistent with previous studies. Even though most of the samples (S1, S2, S3, S5, S6, and S7) show an abundance of low viscous particles, sample S4, collected in the afternoon in a hazy condition (RH 63%), show considerably higher solid and semi-solid particles as compared to other samples. A potential explanation for this observation could be that when organic materials condense on the inorganic component, they form a shell that prevents water uptake by the inorganic component resulting in increased viscosity of the overall particle.

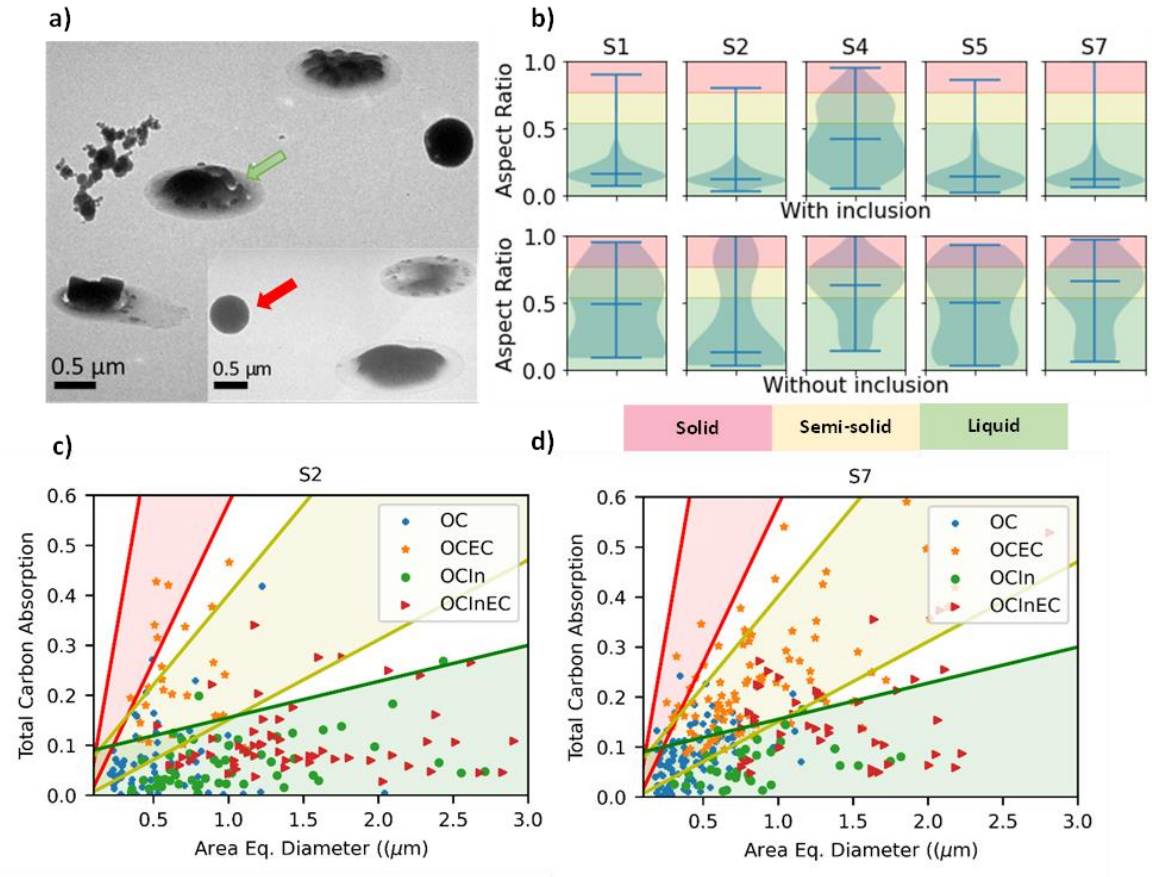

Figure 4-6: a) Tilted view image acquired using TEM showing a liquid-like particle with inclusion (green arrow) (Sample S2) and a spherical particle without inclusion (red arrow) (Sample S4). Particles on S2 collected during daytime show liquid particles with inclusion and particles on S4 collected in the afternoon have spherical and solid particles. b) Particles in each sample are grouped as particles with inclusions and particle without inclusions. The violin plots show the distribution of the aspect ratio values (the blue bars at the end represent the interquartile range) of the particles along with their medians (middle blue bar). The thresholds used to classify the particles into liquid, semi-solid and solid are from Cheng et al. 2021 [22]. The total carbon absorption is plotted against the area equivalent diameter for samples S2 c) and S7 d). Based on the thresholds used in Tomlin et al. 2020, particles with different mixing states (organic mass (OC), organic mass mixed with elemental C (OCEC), organic mass mixed with Inorganic particles (OCIn) and mixture of

organic mass, elemental C and inorganic mass (OCInEC) are also classified into solid, semi-solid, and liquid particles [37].

Along with viscosity, the volatility of the particles also plays a major role in determining the mixing state of the particles during atmospheric aging [45]. VOCs emitted from biomass burning undergo gas-phase oxidation and condense to form secondary organic aerosols (SOA). LVOC can enhance the growth of SOA leading to an increase in cloud condensation nuclei [19].

4.5 Environmental implications

The study was aimed at understanding aerosol processing under haze conditions by determining the chemical composition, morphology, viscosity, and volatility of particles collected during winter from the highly polluted region of the Indo-Gangetic Plain. A major fraction of the aerosols was found to contain K-rich sulfate in most of the samples. Monoterpene derived organosulfates are frequently identified in urban aerosols. Additionally, nitrooxy-OSs are functionalized OSs which are typically found as constituents of atmospheric aqueous media (e.g., cloud, fog, and rain water) [63, 64] . OSs play a crucial role in determining formation pathways of SOA and enhance cloud condensation nuclei activity by affecting particle hygroscopicity. In this study, liquid-like particles with inclusions were found to be abundant in the samples collected during haze [65, 66]. Samples collected in the afternoon showed particles with higher viscosity and smaller size as compared to particles in samples collected in the morning. The composition of low viscosity particles changes as they age due to faster diffusion of pollutants as compared to high viscosity particles. Volatility also plays an important role in determining the chemical composition of particles [18, 46]. Amongst the identified OSs and nitrooxy-OSs, $C_{10}H_{16}NO_9S^-$ is a potential monoterpene derived oxidation product, exclusively found in the morning sample. High volatile particles can dissipate due to photodegradation. When high volatility particles are inside low viscosity particles, they will diffuse out and undergo photodegradation. Whereas highly viscous particles will reduce the photodegradation of internally mixed highly volatile particles as they are not exposed to direct solar radiation and interact with climate for a longer period. Hence studying the chemical composition,

phase state and mixing state properties of aerosols can help better understand their impact on heterogeneous chemistry and evolution of particles and their lifetime in the atmosphere.

4.6 References

1. Fu, H.; Chen, J., Formation, features and controlling strategies of severe haze-fog pollutions in China. *Science of The Total Environment* **2017,** *578*, 121-138.
2. Ding, A. J.; Huang, X.; Nie, W.; Sun, J. N.; Kerminen, V.-M.; Petäjä, T.; Su, H.; Cheng, Y. F.; Yang, X.-Q.; Wang, M. H.; Chi, X. G.; Wang, J. P.; Virkkula, A.; Guo, W. D.; Yuan, J.; Wang, S. Y.; Zhang, R. J.; Wu, Y. F.; Song, Y.; Zhu, T.; Zilitinkevich, S.; Kulmala, M.; Fu, C. B., Enhanced haze pollution by black carbon in megacities in China. *Geophysical Research Letters* **2016,** *43*, (6), 2873-2879.
3. Fortems-Cheiney, A.; Dufour, G.; Hamaoui-Laguel, L.; Foret, G.; Siour, G.; Van Damme, M.; Meleux, F.; Coheur, P.-F.; Clerbaux, C.; Clarisse, L.; Favez, O.; Wallasch, M.; Beekmann, M., Unaccounted variability in NH3 agricultural sources detected by IASI contributing to European spring haze episode. *Geophysical Research Letters* **2016,** *43*, (10), 5475-5482.
4. Guo, S.; Hu, M.; Zamora, M. L.; Peng, J.; Shang, D.; Zheng, J.; Du, Z.; Wu, Z.; Shao, M.; Zeng, L.; Molina, M. J.; Zhang, R., Elucidating severe urban haze formation in China. *Proceedings of the National Academy of Sciences* **2014,** *111*, (49), 17373-17378.
5. Molina, L. T.; Velasco, E.; Retama, A.; Zavala, M., Experience from integrated air quality management in the Mexico City Metropolitan Area and Singapore. *Atmosphere* **2019,** *10*, (9), 512.
6. Mishra, D.; Goyal, P.; Upadhyay, A., Artificial intelligence based approach to forecast PM2.5 during haze episodes: A case study of Delhi, India. *Atmospheric Environment* **2015,** *102*, 239-248.
7. Chen, P.; Kang, S.; Tripathee, L.; Panday, A. K.; Rupakheti, M.; Rupakheti, D.; Zhang, Q.; Guo, J.; Li, C.; Pu, T., Severe air pollution and characteristics of light-absorbing particles in a typical rural area of the Indo-Gangetic Plain. *Environmental Science and Pollution Research* **2020,** *27*, 10617-10628.
8. Nair, V. S.; Moorthy, K. K.; Alappattu, D. P.; Kunhikrishnan, P. K.; George, S.; Nair, P. R.; Babu, S. S.; Abish, B.; Satheesh, S. K.; Tripathi, S. N.; Niranjan, K.; Madhavan, B. L.; Srikant, V.; Dutt, C. B. S.; Badarinath, K. V. S.; Reddy, R. R., Wintertime aerosol characteristics over the Indo-Gangetic Plain (IGP): Impacts of local boundary layer processes and long-range transport. *Journal of Geophysical Research: Atmospheres* **2007,** *112*, (D13).
9. Thomas, A.; Sarangi, C.; Kanawade, V. P., Recent increase in winter hazy days over Central India and the Arabian Sea. *Scientific Reports* **2019,** *9*, (1), 17406.
10. Majumdar, D.; Mondal, R.; Periyasamy, A.; Barman, N.; Dey, S.; Roy, S.; Mandal, P.; Rao, P. S.; Sarkar, U., Characterization and sources of fine carbonaceous aerosol in winter over a megacity on Indo-Gangetic plain. *Urban Climate* **2021,** *39*, 100964.
11. Tripathi, S.; Tare, V.; Chinnam, N.; Srivastava, A. K.; Dey, S.; Agarwal, A.; Kishore, S.; Lal, R.; Manar, M.; Kanawade, V. P., Measurements of atmospheric parameters during Indian Space Research Organization Geosphere Biosphere Programme

Land Campaign II at a typical location in the Ganga basin: 1. Physical and optical properties. *Journal of Geophysical Research: Atmospheres* **2006,** *111*, (D23).
12. Ram, K.; Sarin, M. M.; Tripathi, S. N., A 1 year record of carbonaceous aerosols from an urban site in the Indo-Gangetic Plain: Characterization, sources, and temporal variability. *Journal of Geophysical Research: Atmospheres* **2010,** *115*, (D24).
13. Li, W.; Shao, L., Transmission electron microscopy study of aerosol particles from the brown hazes in northern China. *Journal of Geophysical Research: Atmospheres* **2009,** *114*, (D9).
14. Huang, R.-J.; Zhang, Y.; Bozzetti, C.; Ho, K.-F.; Cao, J.-J.; Han, Y.; Daellenbach, K. R.; Slowik, J. G.; Platt, S. M.; Canonaco, F., High secondary aerosol contribution to particulate pollution during haze events in China. *Nature* **2014,** *514*, (7521), 218-222.
15. Behera, S. N.; Sharma, M., Investigating the potential role of ammonia in ion chemistry of fine particulate matter formation for an urban environment. *Science of The Total Environment* **2010,** *408*, (17), 3569-3575.
16. Liu, Y.; Wu, Z.; Wang, Y.; Xiao, Y.; Gu, F.; Zheng, J.; Tan, T.; Shang, D.; Wu, Y.; Zeng, L., Submicrometer particles are in the liquid state during heavy haze episodes in the urban atmosphere of Beijing, China. *Environmental Science & Technology Letters* **2017,** *4*, (10), 427-432.
17. Zhang, Y.; Sanchez, M.; Douet, C.; Wang, Y.; Bateman, A.; Gong, Z.; Kuwata, M.; Renbaum-Wolff, L.; Sato, B.; Liu, P., Changing shapes and implied viscosities of suspended submicron particles. *Atmospheric Chemistry and Physics* **2015,** *15*, (14), 7819-7829.
18. Xu, W.; Chen, C.; Qiu, Y.; Li, Y.; Zhang, Z.; Karnezi, E.; Pandis, S. N.; Xie, C.; Li, Z.; Sun, J., Organic aerosol volatility and viscosity in the North China Plain: contrast between summer and winter. *Atmospheric Chemistry and Physics* **2021,** *21*, (7), 5463-5476.
19. Estillore, A. D.; Hettiyadura, A. P. S.; Qin, Z.; Leckrone, E.; Wombacher, B.; Humphry, T.; Stone, E. A.; Grassian, V. H., Water Uptake and Hygroscopic Growth of Organosulfate Aerosol. *Environmental Science & Technology* **2016,** *50*, (8), 4259-4268.
20. Singh, N.; Banerjee, T.; Murari, V.; Deboudt, K.; Khan, M. F.; Singh, R. S.; Latif, M. T., Insights into size-segregated particulate chemistry and sources in urban environment over central Indo-Gangetic Plain. *Chemosphere* **2021,** *263*, 128030.
21. Chakraborty, A.; Rajeev, P.; Rajput, P.; Gupta, T., Water soluble organic aerosols in indo gangetic plain (IGP): Insights from aerosol mass spectrometry. *Science of The Total Environment* **2017,** *599-600*, 1573-1582.
22. Izhar, S.; Gupta, T.; Qadri, A. M.; Panday, A. K., Wintertime chemical characteristics of aerosol and their role in light extinction during clear and polluted days in rural Indo Gangetic plain. *Environmental Pollution* **2021,** *282*, 117034.
23. Tiwari, S.; Hopke, P. K.; Thimmaiah, D.; Dumka, U. C.; Srivastava, A. K.; Bisht, D. S.; Rao, P. S.; Chate, D. M.; Srivastava, M. K.; Tripathi, S. N., Nature and sources of ionic species in precipitation across the Indo-Gangetic Plains, India. *Aerosol and Air Quality Research* **2016,** *16*, (4), 943-957.
24. Petters, S. S.; Cui, T.; Zhang, Z.; Gold, A.; McNeill, V. F.; Surratt, J. D.; Turpin, B. J., Organosulfates from dark aqueous reactions of isoprene-derived epoxydiols under cloud and fog conditions: Kinetics, mechanism, and effect of reaction environment on

regioselectivity of sulfate addition. *ACS Earth and Space Chemistry* **2021,** *5*, (3), 474-486.
25. Hettiyadura, A. P. S.; Al-Naiema, I. M.; Hughes, D. D.; Fang, T.; Stone, E. A., Organosulfates in Atlanta, Georgia: anthropogenic influences on biogenic secondary organic aerosol formation. *Atmospheric Chemistry and Physics* **2019,** *19*, (5), 3191-3206.
26. Cui, T.; Zeng, Z.; Dos Santos, E. O.; Zhang, Z.; Chen, Y.; Zhang, Y.; Rose, C. A.; Budisulistiorini, S. H.; Collins, L. B.; Bodnar, W. M., Development of a hydrophilic interaction liquid chromatography (HILIC) method for the chemical characterization of water-soluble isoprene epoxydiol (IEPOX)-derived secondary organic aerosol. *Environmental Science: Processes & Impacts* **2018,** *20*, (11), 1524-1536.
27. Sinha, V.; Kumar, V.; Sarkar, C., Chemical composition of pre-monsoon air in the Indo-Gangetic Plain measured using a new air quality facility and PTR-MS: high surface ozone and strong influence of biomass burning. *Atmospheric Chemistry and Physics* **2014,** *14*, (12), 5921-5941.
28. Mogno, C.; Palmer, P. I.; Knote, C.; Yao, F.; Wallington, T. J., Seasonal distribution and drivers of surface fine particulate matter and organic aerosol over the Indo-Gangetic Plain. *Atmos. Chem. Phys.* **2021,** *21*, (14), 10881-10909.
29. Bondy, A. L.; Craig, R. L.; Zhang, Z.; Gold, A.; Surratt, J. D.; Ault, A. P., Isoprene-derived organosulfates: Vibrational mode analysis by Raman spectroscopy, acidity-dependent spectral modes, and observation in individual atmospheric particles. *The Journal of Physical Chemistry A* **2018,** *122*, (1), 303-315.
30. Shrivastava, M.; Cappa, C. D.; Fan, J.; Goldstein, A. H.; Guenther, A. B.; Jimenez, J. L.; Kuang, C.; Laskin, A.; Martin, S. T.; Ng, N. L.; Petaja, T.; Pierce, J. R.; Rasch, P. J.; Roldin, P.; Seinfeld, J. H.; Shilling, J.; Smith, J. N.; Thornton, J. A.; Volkamer, R.; Wang, J.; Worsnop, D. R.; Zaveri, R. A.; Zelenyuk, A.; Zhang, Q., Recent advances in understanding secondary organic aerosol: Implications for global climate forcing. *Reviews of Geophysics* **2017,** *55*, (2), 509-559.
31. Huang, R.-J.; Cao, J.; Chen, Y.; Yang, L.; Shen, J.; You, Q.; Wang, K.; Lin, C.; Xu, W.; Gao, B., Organosulfates in atmospheric aerosol: synthesis and quantitative analysis of PM 2.5 from Xi'an, northwestern China. *Atmospheric Measurement Techniques* **2018,** *11*, (6), 3447-3456.
32. Gao, K.; Zhu, T., Analytical methods for organosulfate detection in aerosol particles: current status and future perspectives. *Science of the Total Environment* **2021,** *784*, 147244.
33. O'Brien, R. E.; Laskin, A.; Laskin, J.; Rubitschun, C. L.; Surratt, J. D.; Goldstein, A. H., Molecular characterization of S-and N-containing organic constituents in ambient aerosols by negative ion mode high-resolution nanospray desorption electrospray ionization mass spectrometry: CalNex 2010 field study. *Journal of Geophysical Research: Atmospheres* **2014,** *119*, (22), 12,706-12,720.
34. Tao, S.; Lu, X.; Levac, N.; Bateman, A. P.; Nguyen, T. B.; Bones, D. L.; Nizkorodov, S. A.; Laskin, J.; Laskin, A.; Yang, X., Molecular characterization of organosulfates in organic aerosols from Shanghai and Los Angeles urban areas by nanospray-desorption electrospray ionization high-resolution mass spectrometry. *Environmental Science & Technology* **2014,** *48*, (18), 10993-11001.

35. Cai, D.; Wang, X.; Chen, J.; Li, X., Molecular characterization of organosulfates in highly polluted atmosphere using ultra-high-resolution mass spectrometry. *Journal of Geophysical Research: Atmospheres* **2020,** *125*, (8), e2019JD032253.
36. Bondy, A. L.; Bonanno, D.; Moffet, R. C.; Wang, B.; Laskin, A.; Ault, A. P., The diverse chemical mixing state of aerosol particles in the southeastern United States. *Atmospheric chemistry and physics* **2018,** *18*, (16), 12595-12612.
37. Cheng, Z.; Sharma, N.; Tseng, K.-P.; Kovarik, L.; China, S., Direct observation and assessment of phase states of ambient and lab-generated sub-micron particles upon humidification. *RSC advances* **2021,** *11*, (25), 15264-15272.
38. Hopkins, R. J.; Tivanski, A. V.; Marten, B. D.; Gilles, M. K., Chemical bonding and structure of black carbon reference materials and individual carbonaceous atmospheric aerosols. *Journal of Aerosol Science* **2007,** *38*, (6), 573-591.
39. Cook, R. D.; Lin, Y. H.; Peng, Z.; Boone, E.; Chu, R. K.; Dukett, J. E.; Gunsch, M. J.; Zhang, W.; Tolic, N.; Laskin, A.; Pratt, K. A., Biogenic, urban, and wildfire influences on the molecular composition of dissolved organic compounds in cloud water. *Atmos. Chem. Phys.* **2017,** *17*, (24), 15167-15180.
40. Murari, V.; Kumar, M.; Singh, N.; Singh, R.; Banerjee, T., Particulate morphology and elemental characteristics: variability at middle Indo-Gangetic Plain. *Journal of Atmospheric Chemistry* **2016,** *73*, 165-179.
41. Chantara, S.; Thepnuan, D.; Wiriya, W.; Prawan, S.; Tsai, Y. I., Emissions of pollutant gases, fine particulate matters and their significant tracers from biomass burning in an open-system combustion chamber. *Chemosphere* **2019,** *224*, 407-416.
42. Li, W.; Shao, L.; Buseck, P., Haze types in Beijing and the influence of agricultural biomass burning. *Atmospheric Chemistry and Physics* **2010,** *10*, (17), 8119-8130.
43. China, S.; Burrows, S. M.; Wang, B.; Harder, T. H.; Weis, J.; Tanarhte, M.; Rizzo, L. V.; Brito, J.; Cirino, G. G.; Ma, P.-L., Fungal spores as a source of sodium salt particles in the Amazon basin. *Nature communications* **2018,** *9*, (1), 4793.
44. Wang, Y.; Zhang, Q.; Jiang, J.; Zhou, W.; Wang, B.; He, K.; Duan, F.; Zhang, Q.; Philip, S.; Xie, Y., Enhanced sulfate formation during China's severe winter haze episode in January 2013 missing from current models. *Journal of Geophysical Research: Atmospheres* **2014,** *119*, (17), 10,425-10,440.
45. Li, G.; Bei, N.; Cao, J.; Huang, R.; Wu, J.; Feng, T.; Wang, Y.; Liu, S.; Zhang, Q.; Tie, X., A possible pathway for rapid growth of sulfate during haze days in China. *Atmospheric Chemistry and Physics* **2017,** *17*, (5), 3301-3316.
46. Ervens, B., Modeling the processing of aerosol and trace gases in clouds and fogs. *Chemical reviews* **2015,** *115*, (10), 4157-4198.
47. Wang, W.; Liu, M.; Wang, T.; Song, Y.; Zhou, L.; Cao, J.; Hu, J.; Tang, G.; Chen, Z.; Li, Z., Sulfate formation is dominated by manganese-catalyzed oxidation of SO2 on aerosol surfaces during haze events. *Nature communications* **2021,** *12*, (1), 1993.
48. Wang, W.; Shao, L.; Guo, M.; Hou, C.; Xing, J.; Wu, F., Physicochemical properties of individual airborne particles in Beijing during pollution periods. *Aerosol and Air Quality Research* **2017,** *17*, (12), 3209-3219.

49. Liu, X.; Van Espen, P.; Adams, F.; Cafmeyer, J.; Maenhaut, W., Biomass burning in southern Africa: Individual particle characterization of atmospheric aerosols and savanna fire samples. *Journal of Atmospheric Chemistry* **2000,** *36*, 135-155.
50. Moteki, N.; Adachi, K.; Ohata, S.; Yoshida, A.; Harigaya, T.; Koike, M.; Kondo, Y., Anthropogenic iron oxide aerosols enhance atmospheric heating. *Nature communications* **2017,** *8*, (1), 15329.
51. Engling, G.; Lee, J. J.; Tsai, Y.-W.; Lung, S.-C. C.; Chou, C. C.-K.; Chan, C.-Y., Size-resolved anhydrosugar composition in smoke aerosol from controlled field burning of rice straw. *Aerosol Science and Technology* **2009,** *43*, (7), 662-672.
52. Han, Y.; Zhang, X.; Li, L.; Lin, Y.; Zhu, C.; Zhang, N.; Wang, Q.; Cao, J., Enhanced Production of Organosulfur Species during a Severe Winter Haze Episode in the Guanzhong Basin of Northwest China. *Environmental Science & Technology* **2023,** *57*, (23), 8708-8718.
53. Glasius, M.; Thomsen, D.; Wang, K.; Iversen, L. S.; Duan, J.; Huang, R.-J., Chemical characteristics and sources of organosulfates, organosulfonates, and carboxylic acids in aerosols in urban Xi'an, Northwest China. *Science of The Total Environment* **2022,** *810*, 151187.
54. Zheng, Y.; Chen, Q.; Cheng, X.; Mohr, C.; Cai, J.; Huang, W.; Shrivastava, M.; Ye, P.; Fu, P.; Shi, X.; Ge, Y.; Liao, K.; Miao, R.; Qiu, X.; Koenig, T. K.; Chen, S., Precursors and Pathways Leading to Enhanced Secondary Organic Aerosol Formation during Severe Haze Episodes. *Environmental Science & Technology* **2021,** *55*, (23), 15680-15693.
55. Ning, C.; Gao, Y.; Zhang, H.; Yu, H.; Cao, R.; Chen, J., Urban particulate water-soluble organic matter in winter: Size-resolved molecular characterization, role of the S-containing compounds on haze formation. *Science of The Total Environment* **2023,** *875*, 162657.
56. Pitts, M. C.; Poole, L. R.; Gonzalez, R., Polar stratospheric cloud climatology based on CALIPSO spaceborne lidar measurements from 2006 to 2017. *Atmos. Chem. Phys.* **2018,** *18*, (15), 10881-10913.
57. Schum, S. K.; Zhang, B.; Džepina, K.; Fialho, P.; Mazzoleni, C.; Mazzoleni, L. R., Molecular and physical characteristics of aerosol at a remote free troposphere site: implications for atmospheric aging. *Atmos. Chem. Phys.* **2018,** *18*, (19), 14017-14036.
58. Bryant, D. J.; Nelson, B. S.; Swift, S. J.; Budisulistiorini, S. H.; Drysdale, W. S.; Vaughan, A. R.; Newland, M. J.; Hopkins, J. R.; Cash, J. M.; Langford, B., Biogenic and anthropogenic sources of isoprene and monoterpenes and their secondary organic aerosol in Delhi, India. *Atmospheric Chemistry and Physics* **2023,** *23*, (1), 61-83.
59. Pei, Q.; Saikawa, E.; Kaspari, S.; Widory, D.; Zhao, C.; Wu, G.; Loewen, M.; Wan, X.; Kang, S.; Wang, X.; Zhang, Y.-L.; Cong, Z., Sulfur aerosols in the Arctic, Antarctic, and Tibetan Plateau: Current knowledge and future perspectives. *Earth-Science Reviews* **2021,** *220*, 103753.
60. Tolocka, M. P.; Turpin, B., Contribution of Organosulfur Compounds to Organic Aerosol Mass. *Environmental Science & Technology* **2012,** *46*, (15), 7978-7983.
61. Wang, Y.; Hu, M.; Guo, S.; Wang, Y.; Zheng, J.; Yang, Y.; Zhu, W.; Tang, R.; Li, X.; Liu, Y., The secondary formation of organosulfates under interactions between

biogenic emissions and anthropogenic pollutants in summer in Beijing. *Atmospheric Chemistry and Physics* **2018,** *18*, (14), 10693-10713.
62. LeClair, J. P.; Collett, J. L.; Mazzoleni, L. R., Fragmentation analysis of water-soluble atmospheric organic matter using ultrahigh-resolution FT-ICR mass spectrometry. *Environmental science & technology* **2012,** *46*, (8), 4312-4322.
63. Liggio, J.; Li, S.-M., Organosulfate formation during the uptake of pinonaldehyde on acidic sulfate aerosols. *Geophysical Research Letters* **2006,** *33*, (13).
64. Surratt, J. D.; Gómez-González, Y.; Chan, A. W. H.; Vermeylen, R.; Shahgholi, M.; Kleindienst, T. E.; Edney, E. O.; Offenberg, J. H.; Lewandowski, M.; Jaoui, M.; Maenhaut, W.; Claeys, M.; Flagan, R. C.; Seinfeld, J. H., Organosulfate Formation in Biogenic Secondary Organic Aerosol. *The Journal of Physical Chemistry A* **2008,** *112*, (36), 8345-8378.
65. Nguyen, T. B.; Lee, P. B.; Updyke, K. M.; Bones, D. L.; Laskin, J.; Laskin, A.; Nizkorodov, S. A., Formation of nitrogen- and sulfur-containing light-absorbing compounds accelerated by evaporation of water from secondary organic aerosols. *Journal of Geophysical Research: Atmospheres* **2012,** *117*, (D1).
66. Staudt, S.; Kundu, S.; Lehmler, H.-J.; He, X.; Cui, T.; Lin, Y.-H.; Kristensen, K.; Glasius, M.; Zhang, X.; Weber, R. J.; Surratt, J. D.; Stone, E. A., Aromatic organosulfates in atmospheric aerosols: Synthesis, characterization, and abundance. *Atmospheric Environment* **2014,** *94*, 366-373.

5 Conclusions

Aerosols scatter and absorb incoming solar radiation having a radiative forcing (RF) on Earth's atmosphere and hence cooling or warming the climate [1]. The light absorption and scattering coefficients of aerosols depend on several factors such as the chemical composition [2], size [3], concentration, mixing state, shape, [4] and residence time in the atmosphere [5]. However, there are large uncertainties associated with the RF values of different types of aerosols [6]. For instance, the top of the atmosphere RF (TOA-RF) values reported for sulfate aerosols are in the range of -0.6 to -0.2 Wm^{-2} with an average value of -0.4 Wm^{-2} whereas the reported TOA RF value for secondary organic aerosols are in the range of -0.27 to 0.2 Wm^{-2} with an average value of -0.03 Wm^{-2} [6]. The TOA RF of absorbing aerosols such as black carbon is even wider ranging from 0.05 to 0.8 Wm^{-2} [6] whereas the TOA RF of moderately to strongly absorbing BrC ranges from 0.04 to 0.11 Wm^{-2} [7, 8]. The uncertainties are caused by factors such as emission factors, sources, changes in chemical composition, phase and mixing state of aerosols during atmospheric transport, shape, interaction with clouds, and meteorological conditions [9]. For instance, the vast diversity of organic aerosols along with their complex physical and chemical processes in converting gas phase organics to aerosols leads to uncertainty in the sink and chemistry of secondary organic aerosols [10, 11]. Furthermore, recent studies have shown that organic aerosols undergo nucleation of new particles in the presence of sulfuric acid and condensable organic matter. Hence, ignoring the size distribution from the new particle formation due to organics and sulfur will lead to underestimation of TOA RF by 33% [12].

Through this dissertation we addressed three main scientific questions:

1) What is the impact of meteorological factors and the chemical composition of aerosols with respect to altitude on the top of the atmosphere radiative forcing? (Chapter 2)
2) What is the complex refractive index of tar balls at an elevated site in the free troposphere and how does the large range of tar balls refractive index values reported in the literature impact the value and sign of the top of the atmosphere radiative forcing of these abundant particles? (Chapter 3)

3) What happens to the chemical composition of carbonaceous aerosols on a humid day in a highly polluted region and what are the implications on climate? (Chapter 4)

In chapter 2, we focused on the vertical distribution of aerosol properties measured at the Southern Great Plains (SGP) site of the Department of Defense Atmospheric Radiation Measurements program (ARM). On a humid day (25 Feb) there was a higher fraction of sulfates in the atmosphere leading to high single scattering albedo (SSA) values. In our study even though we had other types of aerosols such as Na-rich, carbonaceous, and different types of dust particles, the average RF calculated using the optical properties of all these aerosols is -0.3 Wm^{-2} with an uncertainty range of -0.2 to -0.4 Wm^{-2} which is close the range of the globally averaged RF values reported for sulfates in the IPCC report. Moreover, on 18 April when there was higher fraction of carbonaceous aerosols the calculated average RF value was -0.08 Wm^{-2} with an uncertainty range of 0.19 to -0.06 Wm^{-2} which is close to the range of reported globally averaged RF for secondary organic aerosols in the IPCC report [6]. Hence, from this study we can conclude that the chemical composition of aerosols and the abundance of a particular type of aerosols play a major role in determining the direct RF values and models need to account for the chemical composition of aerosols at specific regions to better understand the climate and weather patterns.

In chapter 2, we reviewed the observed range of the refractive index values of tarballs (a type of absorbing aerosols) reported in the literature and compared them to the values we measured on single particles collected at an elevated sites in the Apennines in Northern Italy. The imaginary part of the refractive index (k) from our study lays between the maximum and minimum k values reported in previous studies. We observed that the large variability in k not only affects the RF values but even the sign which determines if these particles cool or warm the climate. Studies have reported the number fraction of tarballs ranging from 23% [13] to 43% [14], in the free troposphere; hence, it is essential to constrain the refractive index of tar balls or apportion it based on factors such as source (fuel),

residence time in the atmosphere, and chemical composition that can be measured or modeled in future studies.

In Chapter 3, we discussed the phase state of organic aerosols that are internally mixed with sulfate aerosols collected during a hazy period. We also discussed the volatility of the aerosols. Both viscosity and volatility are key in understanding the chemical composition of aerosols because low aerosol viscosity allow for faster diffusion of pollutants into the particle and high volatile aerosols can volatilize due to photodegradation [15, 16]. However, when highly volatile particles are internally mixed with low viscous aerosols due to faster diffusion into the particle, the residence time in the atmosphere of high volatile particles increases. In our study, we found that highly volatile and hygroscopic aerosols such as sulfates were internally mixed with organic aerosols lowering the viscosity of the internally mixed aerosols. Hence, region specific chemical composition, optical properties and phase state needs to be accounted for in chemical transport, climate, and weather models to better estimate the impact of aerosols.

5.1 References

1. Coakley Jr, J. A.; Cess, R. D.; Yurevich, F. B., The effect of tropospheric aerosols on the Earth's radiation budget: A parameterization for climate models. *Journal of Atmospheric Sciences* **1983,** *40*, (1), 116-138.
2. Andreae, M. O.; Schmid, O.; Yang, H.; Chand, D.; Zhen Yu, J.; Zeng, L.-M.; Zhang, Y.-H., Optical properties and chemical composition of the atmospheric aerosol in urban Guangzhou, China. *Atmospheric Environment* **2008,** *42*, (25), 6335-6350.
3. Ysard, N.; Jones, A.; Demyk, K.; Boutéraon, T.; Koehler, M., The optical properties of dust: the effects of composition, size, and structure. *Astronomy & Astrophysics* **2018,** *617*, A124.
4. Mishra, S. K.; Tripathi, S., Modeling optical properties of mineral dust over the Indian Desert. *Journal of Geophysical Research: Atmospheres* **2008,** *113*, (D23).
5. Liu, J.; Lin, P.; Laskin, A.; Laskin, J.; Kathmann, S. M.; Wise, M.; Caylor, R.; Imholt, F.; Selimovic, V.; Shilling, J. E., Optical properties and aging of light-absorbing secondary organic aerosol. *Atmos. Chem. Phys.* **2016,** *16*, (19), 12815-12827.

6. Ramaswamy, V.; Collins, W.; Haywood, J.; Lean, J.; Mahowald, N.; Myhre, G.; Naik, V.; Shine, K. P.; Soden, B.; Stenchikov, G.; Storelvmo, T., Radiative Forcing of Climate: The Historical Evolution of the Radiative Forcing Concept, the Forcing Agents and their Quantification, and Applications. *Meteorological Monographs* **2019,** *59*.
7. Wu, G.-M.; Cong, Z.-Y.; Kang, S.-C.; Kawamura, K.; Fu, P.-Q.; Zhang, Y.-L.; Wan, X.; Gao, S.-P.; Liu, B., Brown carbon in the cryosphere: Current knowledge and perspective. *Advances in Climate Change Research* **2016,** *7*, (1), 82-89.
8. Feng, Y.; Ramanathan, V.; Kotamarthi, V. R., Brown carbon: a significant atmospheric absorber of solar radiation? *Atmos. Chem. Phys.* **2013,** *13*, (17), 8607-8621.
9. Ma, Y.; Xin, J.; Zhang, W.; Gong, C.; Wen, T.; Wu, X.; Wang, Y.; Wang, L.; Wu, F.; Ding, X., Uncertainties of Simulated Aerosol Direct Radiative Effect Induced by Aerosol Chemical Components: A Measurement-Based Perspective From Urban-Forest Transition Region in East China. *Journal of Geophysical Research: Atmospheres* **2021,** *126*, (8), e2020JD033688.
10. Lin, G.; Penner, J.; Sillman, S.; Taraborrelli, D.; Lelieveld, J., Global modeling of SOA formation from dicarbonyls, epoxides, organic nitrates and peroxides. *Atmospheric Chemistry and Physics* **2012,** *12*, (10), 4743-4774.
11. Lin, G.; Sillman, S.; Penner, J.; Ito, A., Global modeling of SOA: the use of different mechanisms for aqueous-phase formation. *Atmospheric Chemistry and Physics* **2014,** *14*, (11), 5451-5475.
12. Lin, G. Global Modeling of Secondary Organic Aerosol Formation: From Atmospheric Chemistry to Climate. 2013.
13. Barry, K. R.; Hill, T. C. J.; Levin, E. J. T.; Twohy, C. H.; Moore, K. A.; Weller, Z. D.; Toohey, D. W.; Reeves, M.; Campos, T.; Geiss, R.; Schill, G. P.; Fischer, E. V.; Kreidenweis, S. M.; DeMott, P. J., Observations of Ice Nucleating Particles in the Free Troposphere From Western US Wildfires. *Journal of Geophysical Research: Atmospheres* **2021,** *126*, (3), e2020JD033752.
14. Dzepina, K.; Mazzoleni, C.; Fialho, P.; China, S.; Zhang, B.; Owen, R. C.; Helmig, D.; Hueber, J.; Kumar, S.; Perlinger, J. A.; Kramer, L. J.; Dziobak, M. P.; Ampadu, M. T.; Olsen, S.; Wuebbles, D. J.; Mazzoleni, L. R., Molecular characterization of free tropospheric aerosol collected at the Pico Mountain Observatory: a case study with a long-range transported biomass burning plume. *Atmos. Chem. Phys.* **2015,** *15*, (9), 5047-5068.
15. Xu, W.; Chen, C.; Qiu, Y.; Li, Y.; Zhang, Z.; Karnezi, E.; Pandis, S. N.; Xie, C.; Li, Z.; Sun, J., Organic aerosol volatility and viscosity in the North China Plain: contrast between summer and winter. *Atmospheric Chemistry and Physics* **2021,** *21*, (7), 5463-5476.
16. Ervens, B., Modeling the processing of aerosol and trace gases in clouds and fogs. *Chemical reviews* **2015,** *115*, (10), 4157-4198.

A Appendix

A.1 SBDART program

The Santa Barbara DISORT (DIScrete Ordinate Radiative Transfer) model (SBDART) is a software that can be used to compute instantaneous direct upwelling and downwelling radiation fluxes for a variety of scenarios. The main input file is called INPUT. The outputs are generated from the values provided for all the variables in the input file. A detailed description of all the variables can be found in the user guide of SBDART. (http://irina.eas.gatech.edu/EAS8803_Fall2007/User_guide_SBDART_input.pdf).

Different scenarios and input values that we used for TOA RF calculations are as follows:

1) Input file for retrieving upwelling and downwelling fluxes for clear sky with no aerosol:

for times at 00.0 01.0 02.0 03.0 04.0 05.0 06.0 07.0 08.0 09.0 10.0 11.0 12.0 13.0 14.0 15.0 16.0 17.0 18.0 19.0 20.0 21.0 22.0 23.0 ; do // For loop to get the flux values for 24 hours

```
echo "
&INPUT
 time=$time
 idatm=2
 wlinf=0.2
 wlsup=4
 iday=201
 alat=44.19
 alon=10.70
 isalb=6
 zout=0,100
iout=10
/" > INPUT
 ./sbdart >> Output filename
 done
```

In the above file, *idatm* specifies the type of atmosphere. Value 2 computes mid latitude summer fluxes. *wlinf* and *wlsup* are the lowest and highest wavelength values over which the fluxes are integrated. *iday* is used to input day and month. January 1st is given by *iday* = 1. Here *iday* = 201 implies the day of sample collection (20th July). *alat* and *alon* are the latitude and longitude of the location. *isalb* provides surface type. *isalb* equals 6 is for vegetation. *zout* is the upper and lower altitude for which the net fluxes are calculated. Finally, *iout* detemines the output type. For instance, *iout* = 10 outputs the integrated flux values for the wavelength range between *wlinf* and *wlsup*.

2) Input file for retrieving upwelling and downwelling fluxes for a layer of aerosol without clouds:

for times at 00.0 01.0 02.0 03.0 04.0 05.0 06.0 07.0 08.0 09.0 10.0 11.0 12.0 13.0 14.0 15.0 16.0 17.0 18.0 19.0 20.0 21.0 22.0 23.0 ; do // For loop to get the flux values for 24 hours

```
echo "
&INPUT
 time=$time
 idatm=2
 wlinf=0.2
 wlsup=4
 iday=201
 alat=44.19
 alon=10.70
 isalb=6

iaer=5
tbaer=0.1
zbaer=2.165, 2.265
wlbaer=0.2 0.3 0.4 0.5 0.6 0.7 0.8 0.9 1
```

```
gbaer=.73 .51 .27 .16 .11 .08 .06 .05 .04
wbaer=0.432 0.422 0.450 0.474 0.543 0.641 0.684 0.695 0.689
qbaer=1.3 0.78 0.39 0.18 0.08 0.03 0.02 0.01 0.007

zout=0,100
iout=10
/" > INPUT
 ./sbdart >> Output filename
 done
```

The only addition for the above file to the first scenario are the aerosol optical parameters. *iaer* is used to provide the type of aerosol. *iaer* = 5 allows to input user defined aerosol properties. *tbaer* is the optical depth of the layer of aerosol, *zbaer* gives the upper and lower altitude of the layer of aerosol in km. *gbaer*, *wbaer*, and *qbaer* are the asymmetry parameters, single scattering albedo and extinction efficiency for each wavelength specified by the variable *wlbaer*.

3) Input file for retrieving upwelling and downwelling fluxes for a layer of aerosol with clouds:

```
for times at 00.0 01.0 02.0 03.0 04.0 05.0 06.0 07.0 08.0 09.0 10.0 11.0 12.0 13.0 14.0 15.0
16.0 17.0 18.0 19.0 20.0 21.0 22.0 23.0 ; do // For loop to get the flux values for 24 hours

echo "
&INPUT
 time=$time
 idatm=2
 wlinf=0.2
 wlsup=4
 iday=201
 alat=44.19
```

```
 alon=10.70
 isalb=6

zcloud=3,-4
tcloud=4,1
nre=6,6

iaer=5
tbaer=0.1
zbaer=2.165, 2.265
wlbaer=0.2 0.3 0.4 0.5 0.6 0.7 0.8 0.9 1
gbaer=.73 .51 .27 .16 .11 .08 .06 .05 .04
wbaer=0.432 0.422 0.450 0.474 0.543 0.641 0.684 0.695 0.689
qbaer=1.3 0.78 0.39 0.18 0.08 0.03 0.02 0.01 0.007

zout=0,100
iout=10
/" > INPUT
 ./sbdart >> Output filename
 done
```

To include clouds, the only additions to the previous case are *zcloud*, *tcloud*, and *nre*. Where *zcloud* indicates the lower and upper altitude of the cloud layer altitudes in km separated by a comma. *tcloud* provides the cloud optical thickness and *nre* is used for the droplet size from the lower altitude to the upper altitude of the cloud layer. The variable *nre* equals (6,6) implies the cloud layer has uniform droplet size.

A.2 Electron energy loss spectroscopy analysis

Electron energy loss spectra (EELS) were acquired by a Gatan EELS spectrometer controlled by the Digital Micrograph software. A narrow beam of 80 KeV with an energy dispersion of 0.025 eV/channel was transmitted near the center of homogeneously mixed TBs to acquire EELS spectra. The inhomogeneously mixed TBs were selected in such a

way that the mixing constituents were away from the center so that the beam can transmit near the center of the TBs without hitting the mixing constituents. Hence, the RI for inhomogeneously mixed TBs is without considering the S and K rich inclusions.

From the EELS spectra, we used the low loss region (0 – 10 eV) to derive the optical constants of inhomogeneously and homogeneously mixed TBs. Initially, we removed the zero-loss peak (ZLP) and obtained the single scattering distribution function S(E) (Figure S2) which was then used in the Kramer-Kronig relationship to retrieve the RI. Since the beam produces a symmetric peak, to extract ZLP from EELs spectra we had to fit it with a "logarithmic tail" and adjust the width of the fit such that the zero loss was mostly contained inside the fitted curve [1]. Other methods used to fit ZLP are: Gaussian, Gaussian and Lorentzian, Reflected tail method and using ZLP acquired from vacuum measurements [2]. After removing ZLP, we removed the multiple scattering using a Fourier-log deconvolution method to extract the S(E) of the TB [3]. Figure S3 shows the S(E) of all the inhomogeneously and homogeneously mixed particles. The S(E) of inhomogeneously and homogeneously mixed TBs do not overlap with each other which introduces uncertainty in the measurement of RI.

To calculate the RI using the Kramer-Kronig relationship, we need to know the thickness of the particle and the ZLP height. The ZLP can be recorded directly from EELS spectra after extraction. To find the thickness, we used two different methods. In the first method, we measured the diameter of TBs using a built-in scale in the Gatan software from 2-D image captured by the transmission electron microscope (TEM) (the diameters measured using this method will be referred as "measured diameters" from here on). Since TBs are spherical, the diameter of its 2-D image can be considered as the thickness of the particle. However, if the beam does not pass exactly through the center, the thickness would be less than the diameter of the particle. Hence, to calculate the exact thickness that the beam passed through the TBs, we used the EELs spectra and determined the absolute thickness from the Gatan software (referred to as "absolute thickness" from here on). The absolute thickness significantly underestimates the measured thickness (Figure S5).

Hence, the uncertainty in the thickness can result in an underestimate of the RI. For instance, the thickness of particle P2 estimated as the area equivalent diameter is 186 nm, while the absolute thickness is 131.5 nm. From figure S5, the RI decreases from 1.34 (obtained from the absolute thickness) to 1.30 when the thickness used is increased to 141.5 nm. Using the projected area thickness of 186 nm for particle P2 would result in an RI of 1.21.

A.3 Figures

a)

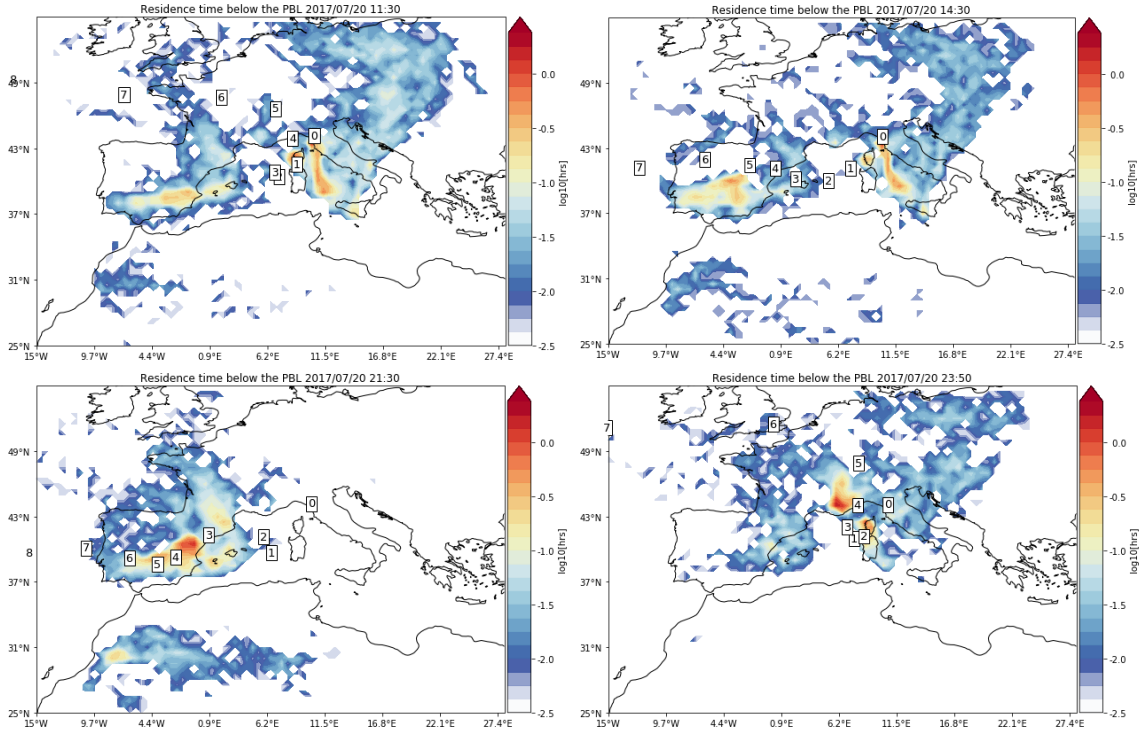

b)

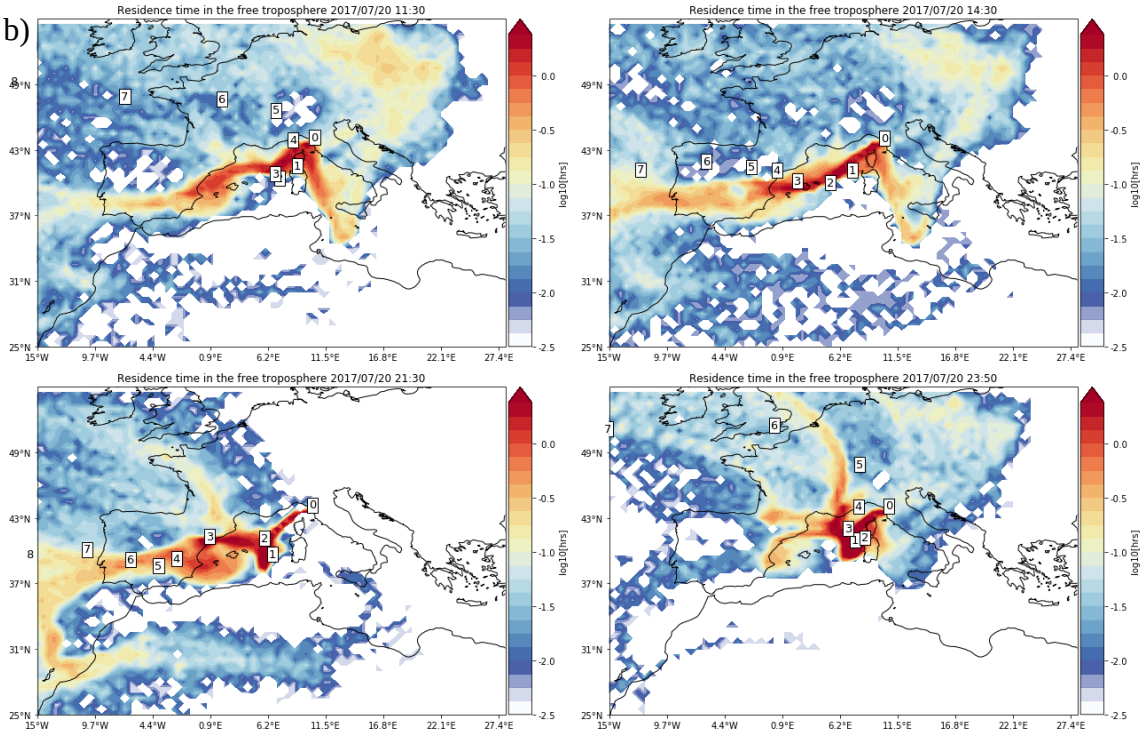

Figure A.3-1:7-days back trajectories starting at the time the day- and night-time samples were collected (11:30 AM, 2:30 PM, 9:00 PM and 11:00 PM on July 20th, 2017). The colors represent the log in base 10 of the "residence time" which has units of hours indicating how long the air masses spent over each geographical bin. In the plots, we show only the residence time of the air masses originating from below the PBL, hence the ones that are most likely influenced by surface emissions. The white boxes indicate the age of the air masses (in days) along the center of mass of the back trajectory plumes. b) Air masses being transported in the free troposphere.

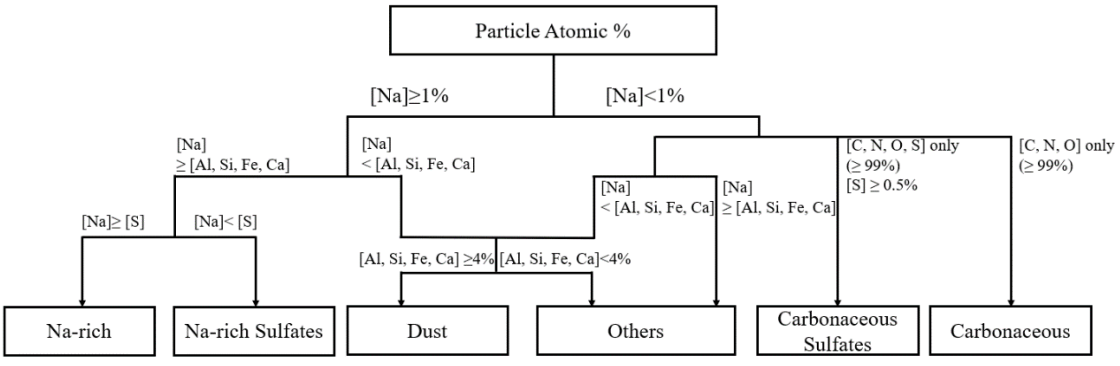

Figure A.3-2: Flow chart showing the threshold values based on atomic percentage of individual elements for the classification of aerosols.

a) b)

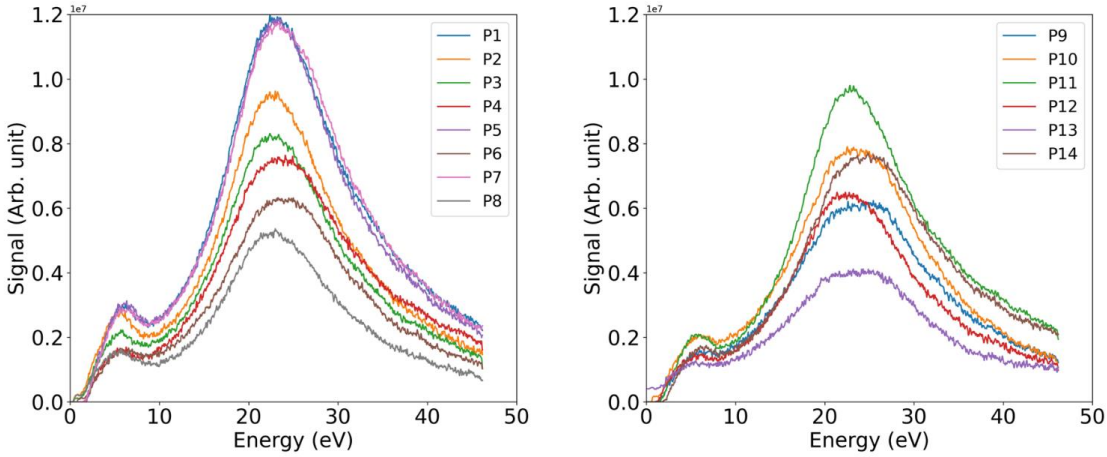

Figure A.3-3: Deconvolved single scattering distribution function for a) homogeneously mixed TBs and b) Inhomogeneously mixed TBs. P1, P2, P3 to P14 refer to four examples of individual particles out of the 20 particles analyzed.

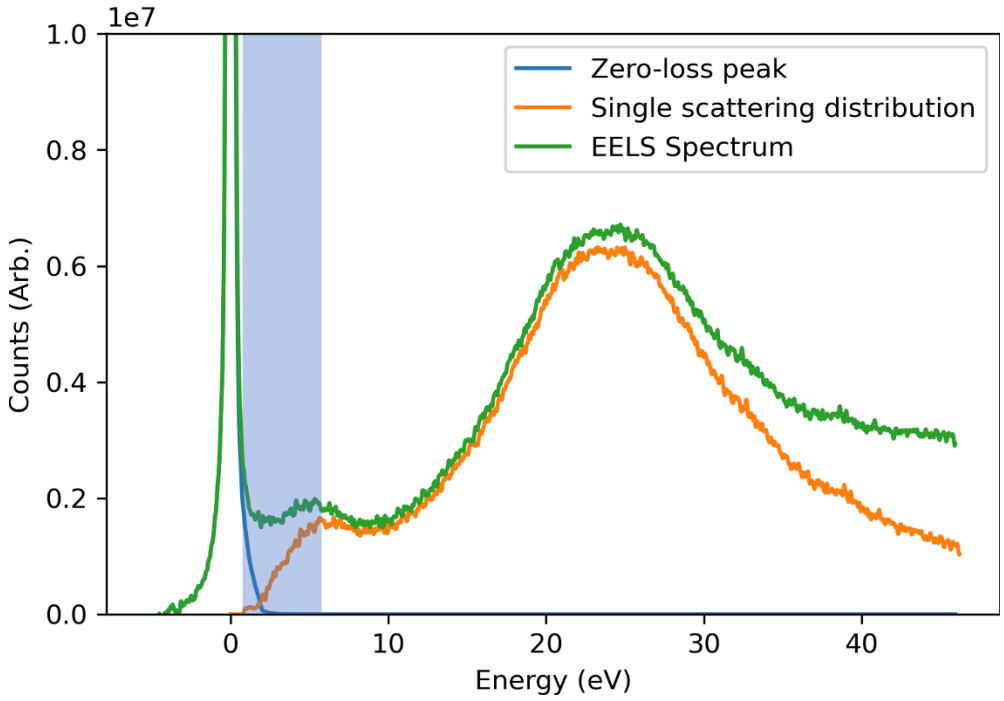

Figure A.3-4: An example of the raw EELS spectrum (green), the extracted zero loss peak (blue) and the multiple scattering corrected single scattering distribution spectrum

after removing the zero loss (orange). The shaded energy region corresponds to the wavelength range from 200 to 1200 nm.

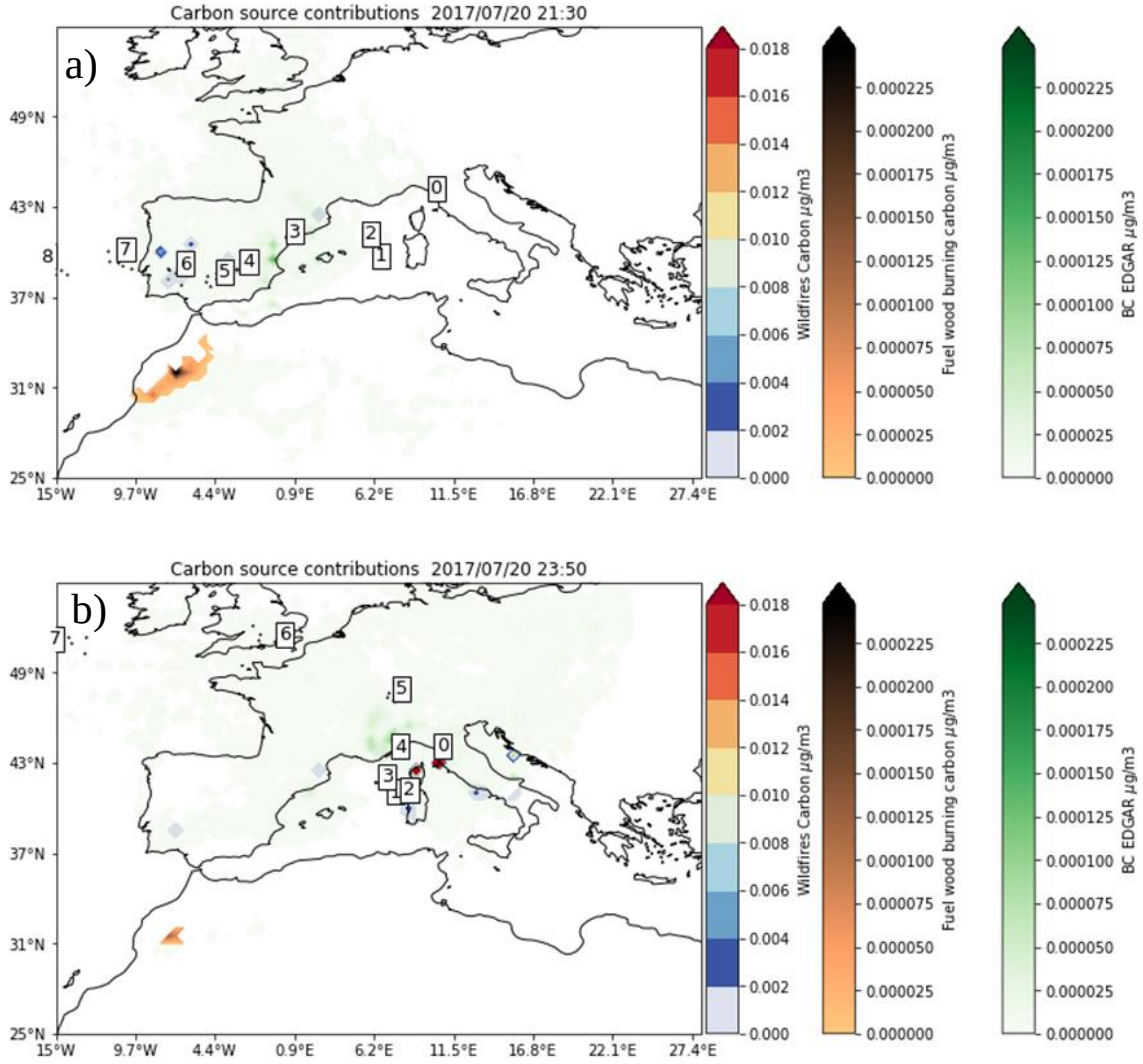

Figure A.3-5: Source contribution, computed from the 7-days back trajectories released at (a) 9:00 PM and (b) 11:00 PM coupled with carbonaceous emissions database for wildfire (colored shades, from GFED), fuel wood fires (brown shades, from GFED) and transport, domestic, waste, industrial and agricultural BC emissions (in green, from EDGAR). The white boxes indicate the age of the air masses (in days), along the center of mass of the back-trajectory plumes.

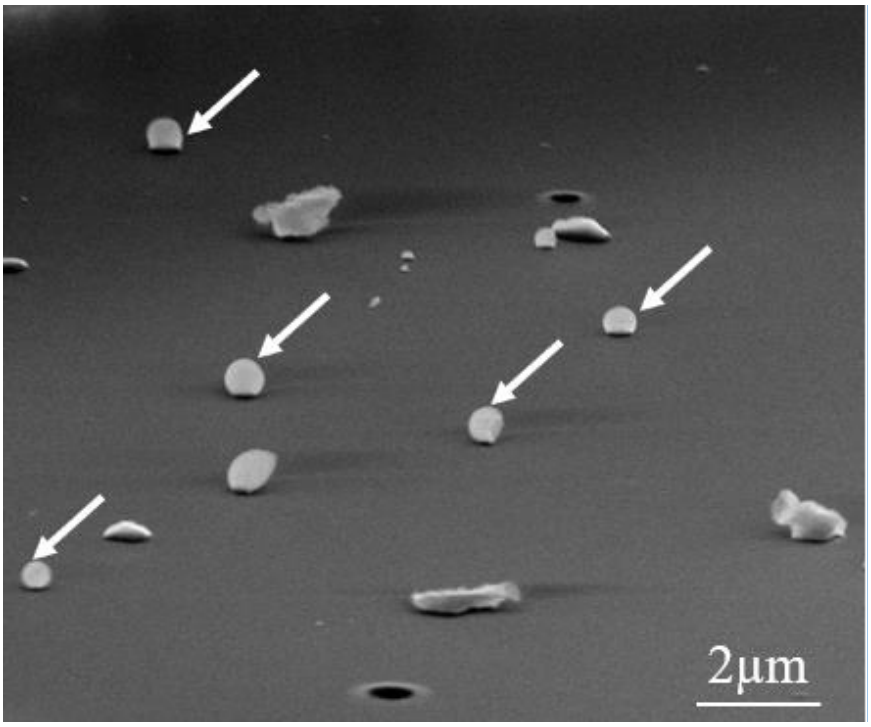

Figure A.3-6: Example of tilted view (75 degree) SEM image (11 PM sample). Tar ball particles are indicated by arrows.

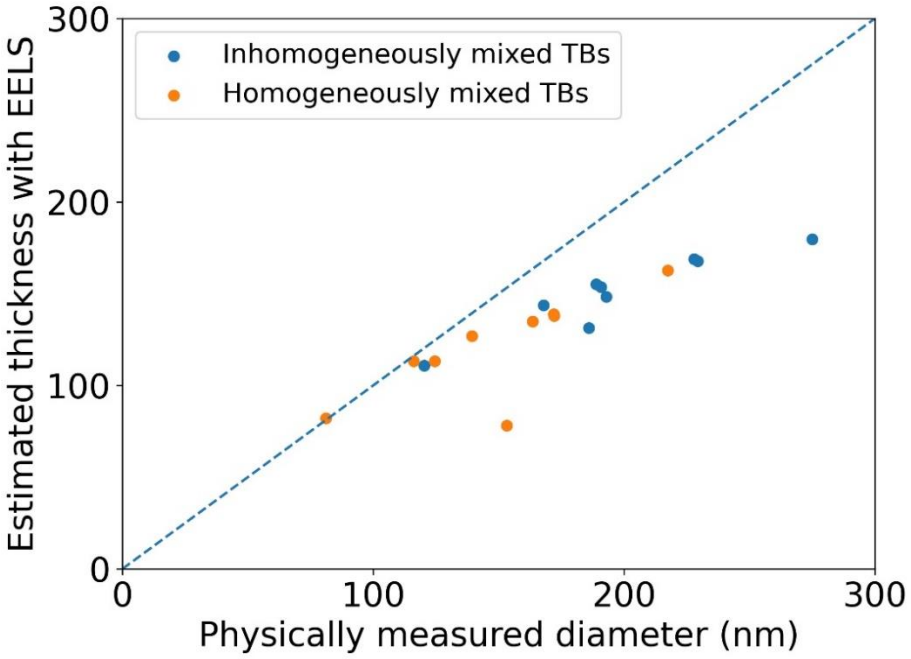

Figure A.3-7: Estimated thickness from EELS spectra plotted against the thickness estimated from the projected area. The dashed line indicates the 1:1 line. The physically measured thickness is greater than the absolute thickness.

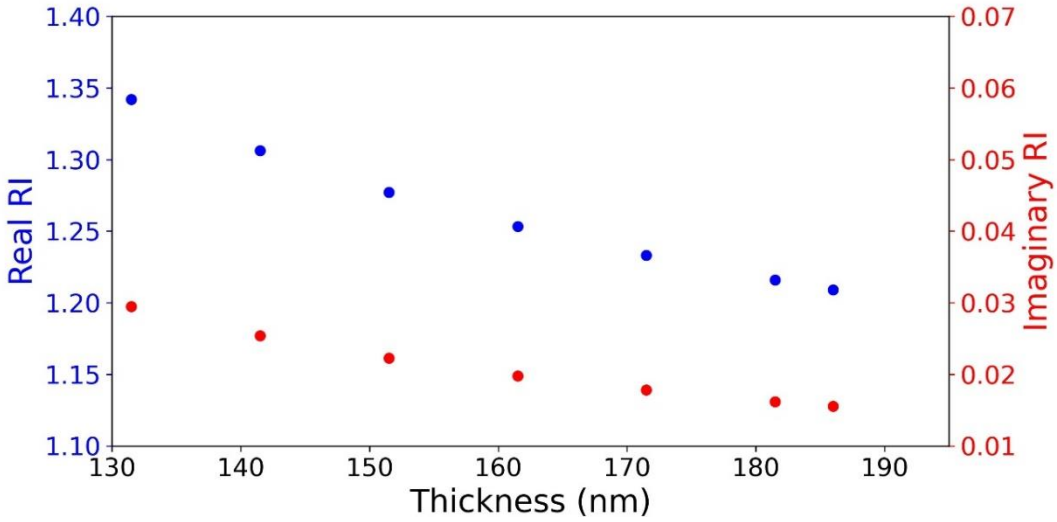

Figure A.3-8: Dependence of the real and imaginary RI on the thickness for a thickness range from 131.5 nm (thickness estimated from EELS spectra) to the maximum value of 186 nm (thickness estimated from the projected area of the particle) for an increment of 10 nm.

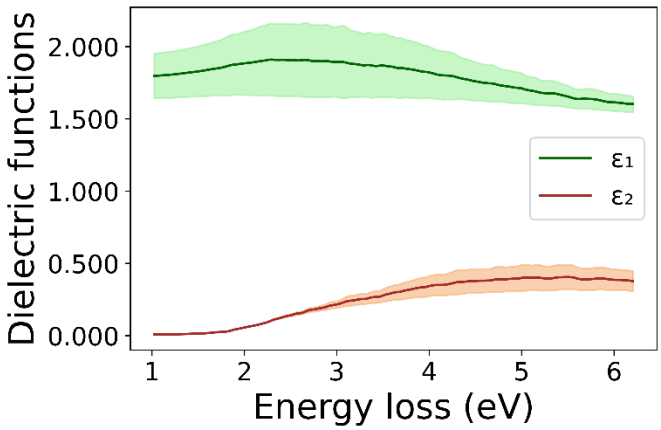

Figure A.3-9: Mean dielectric functions Ɛ1 and Ɛ 2 for all the TBs we analyzed, against the electron energy loss.

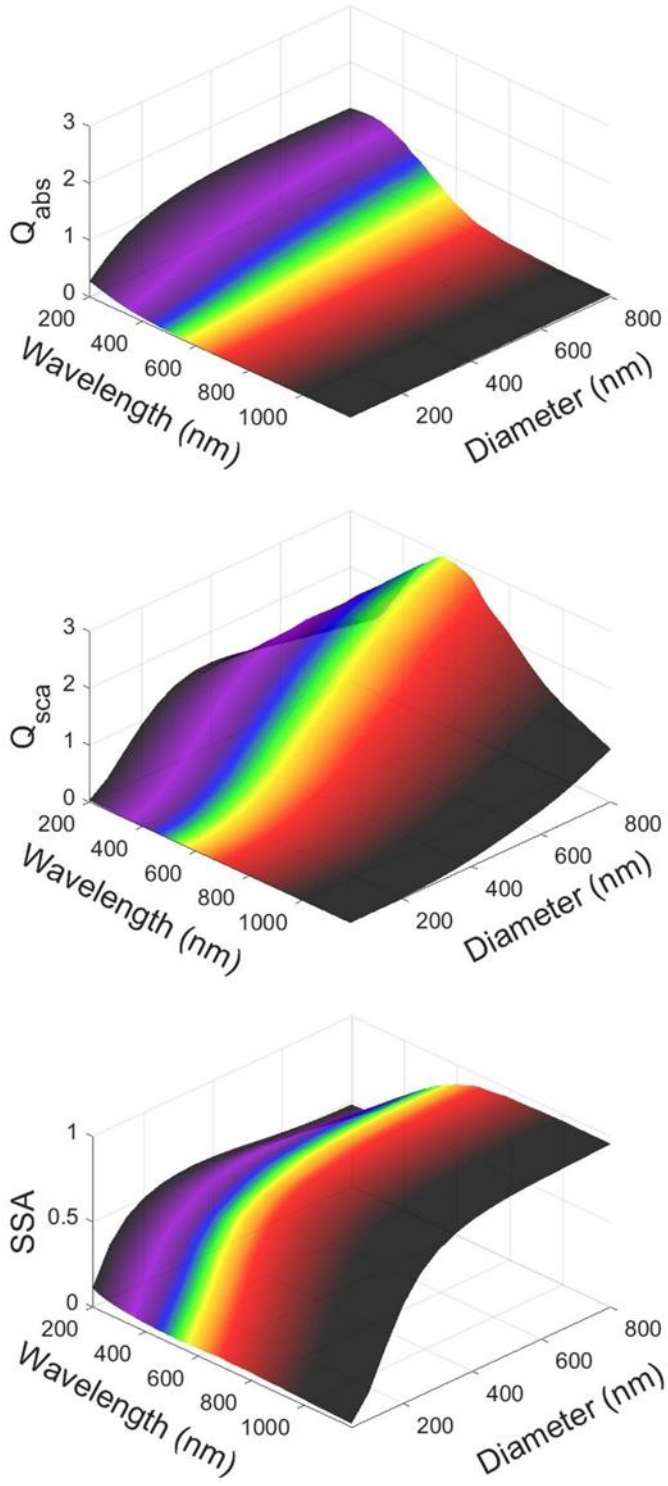

Figure A.3-10: 3D plot of absorption efficiency (Q_{abs}), scattering efficiency (Q_{sca}), and single scattering albedo (SSA) calculated using Lorenz-Mie theory and averaged RI of

inhomogeneously and homogeneously mixed TBs. The colors represent different wavelength regions.

B Appendix: Haze processing of aerosol during wintertime in the Indo-Gangetic Plains

B.1 Sample collection

Table B.1-1: Meteorological parameters of each sample from the nearest airport (Netaji Subhas Chandra Bose International airport station) from the sampling site.

Sample name	Date	Time	Temperature (°K)	Dew Point (°K)	Humidity (%)	Condition
S1	2 Jan 2018	7:00 AM	297	287	53	Hazy
S2	5 Jan 2018	10:00 AM	295	282	43	Non-Hazy
S3	7 Jan 2018	9:30 AM	295	277	31	Hazy
S4	7 Jan 2018	2:00 PM	289	282	63	Hazy
S5	8 Jan 2018	10:00 AM	294	280	40	Hazy
S6	9 Jan 2018	7:00 AM	293	280	46	Non-Hazy
S7	10 Jan 2018	8:00 AM	295	280	38	Non-Hazy
F5	9 Jan 2018	6:00 AM	295	280	52	Smoke
F7	9 Jan 2018	2:00 PM	297	283	78	Haze

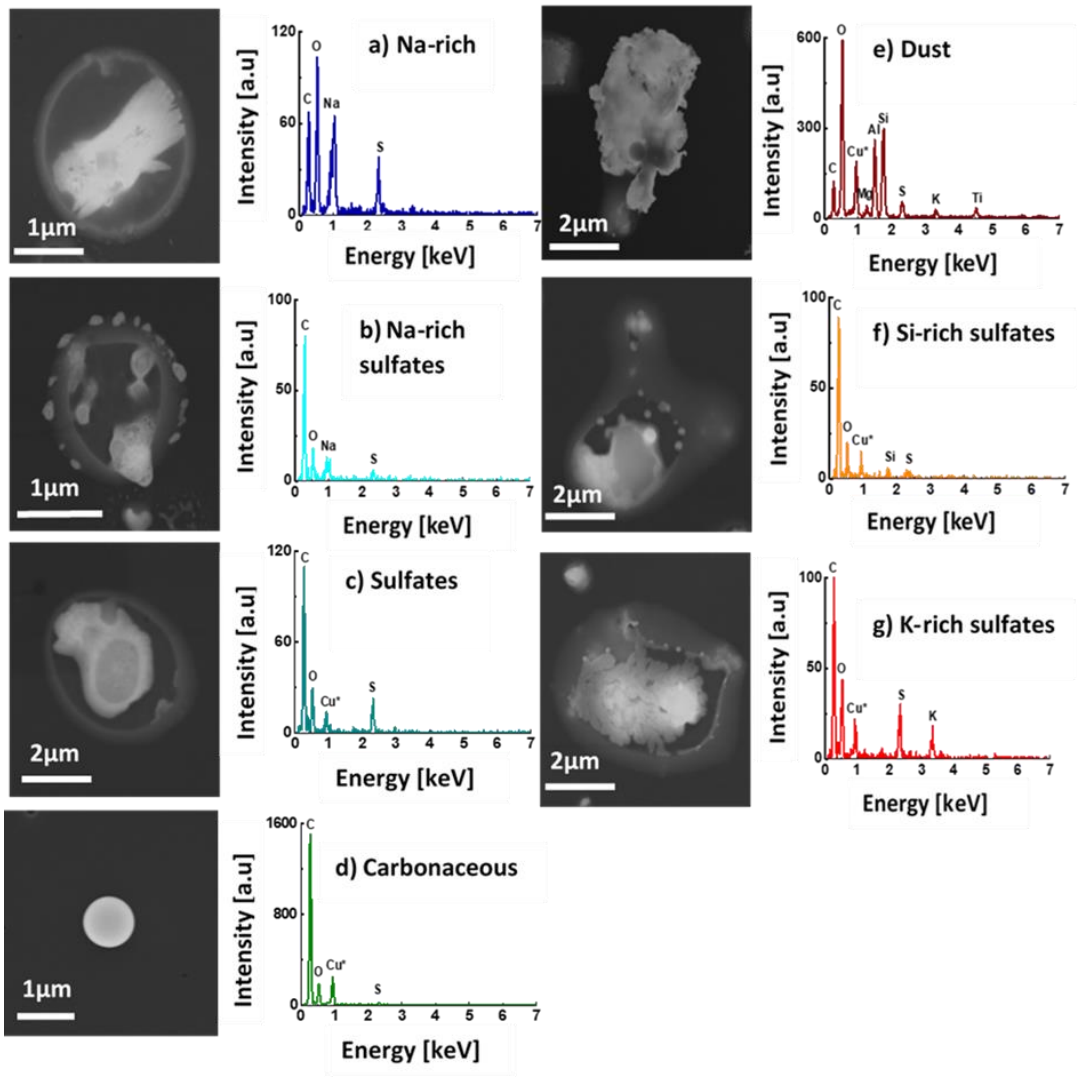

Figure B.1-1: SEM images of representative particles for each class and their spectra collected using energy-dispersive X-ray spectrometry (EDS): a) rod-like Na-rich particle, b) Na-rich sulfate, c) Carbonaceous sulfates, d) Tar ball, e) Dust particle, f) Si-rich sulfates, g) K-rich sulfates.

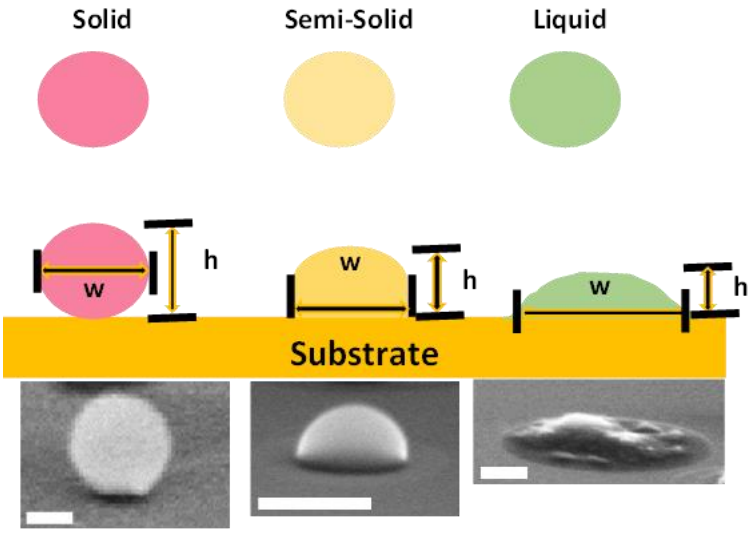

Figure B.1-2: Aspect ratio is calculated as the ratio between the width of the particle (w) to the height of the particle (h). The lower panel shows a representative image of solid, semi-solid, and liquid particles. The size bar in the image equals 1 µm.

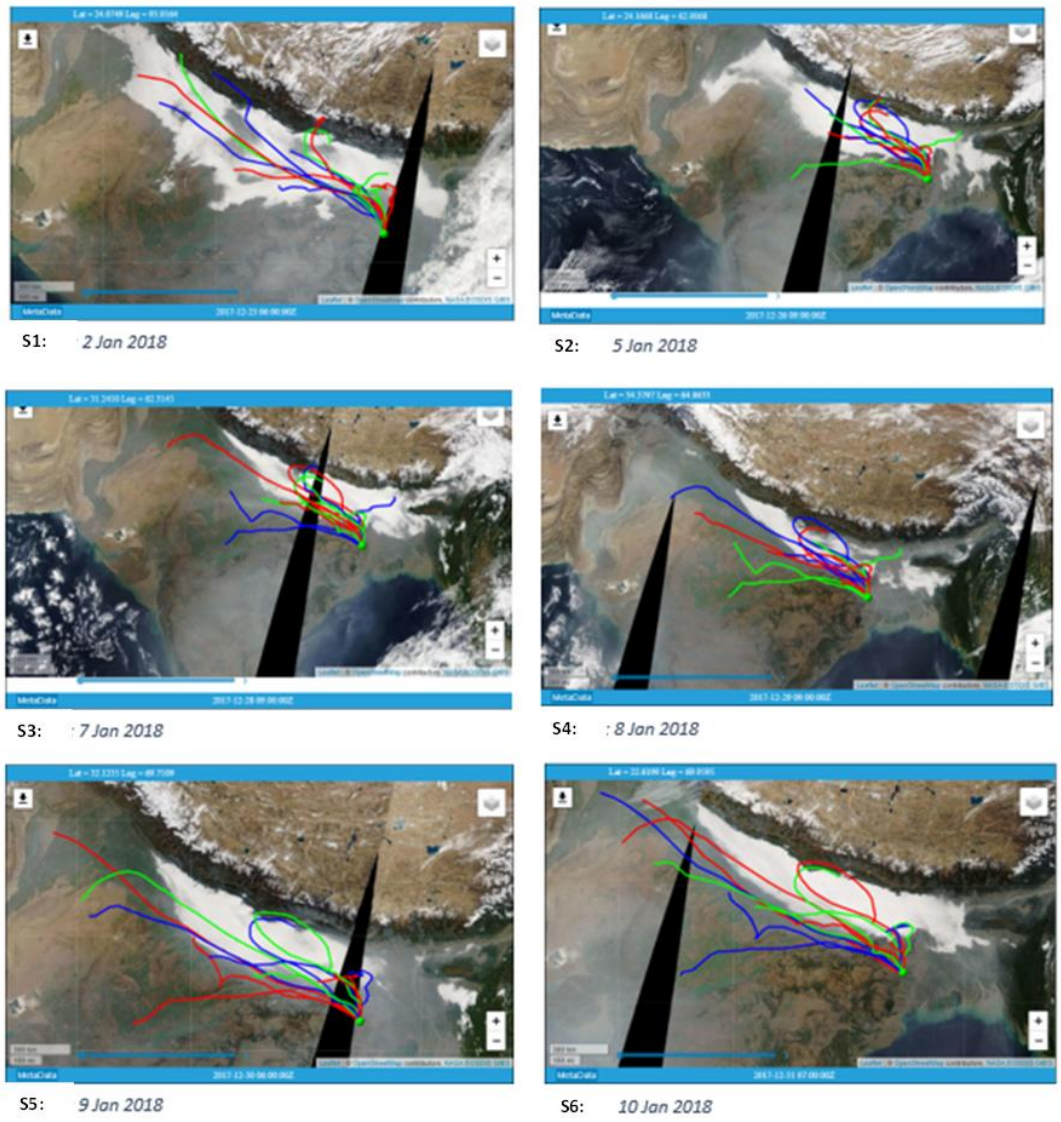

Figure B.1-3: Figure shows the MODIS image of the HYSPLIT back trajectory analysis for a duration of 72 hrs with each color representing a new trajectory with a time interval of 24 hrs. We observe haze at the sampling site as well as along the trajectory of the air parcel for samples S1-S6. The trajectory starts at an altitude of about 2000 m and ends at an altitude of 500 m at the sampling site.

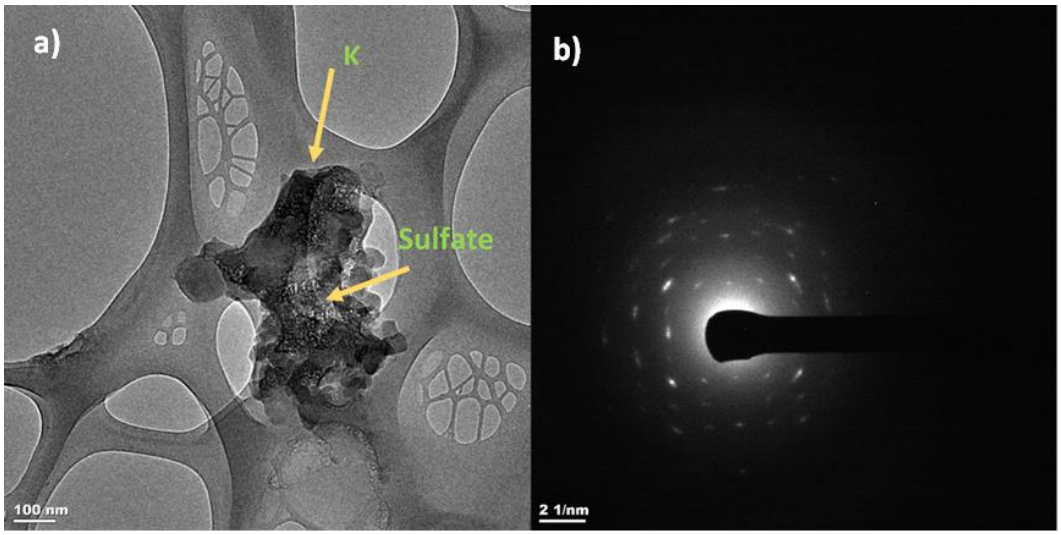

Figure B.1-4: a) TEM image showing mixing of potassium-rich sulfates and b) the diffraction pattern for potassium crystal.

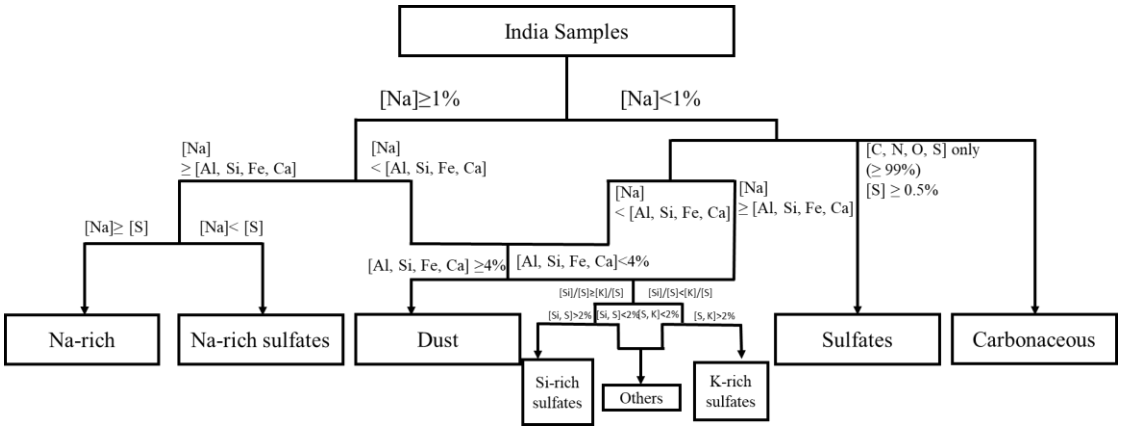

Figure B.1-5: Particles were classified into eight classes based on the elemental composition of C, N, O, Na, Mg, Al, Si, P, S, Cl, K, Ca, Mn, Fe, Zn of each particle. The Figure shows the classification criteria.

B.2 Transmission electron microscopy

FEI Titan Environmental Transmission Electron Microscope operated at 300 kV were used to image and heat particles at different temperatures. A furnace double tilt holder was used to heat the particles. The particles were heated from T_{MEMS} = 35°C to 700°C and the effective temperature that the particles experience was calculated. The particles in the images were classified into three classes highly viscous, highly viscous with attached

particles, and low viscous particles. The deformation in the particles at different temperatures was measured using ImageJ software and the remaining volume fraction at each temperature was determined to understand the volatility of the particles in the samples.

B.3 Scanning transmission x-ray microscopy

To identify the carbon functional groups of individual particles we used STXM-NEXAFS spectroscopy at beamline 5.3.2.2 of the Advanced Light Source (ALS) at the Lawrence Berkley National Laboratory. Only two samples (S2 and S7) were selected due to time constraints for the analysis. The sample was rastered under a focused X-ray beam from the synchrotron light source and an image was recorded based on the transmitted intensity. The total carbon absorption (TCA) to classify particles into solid, semi-solid, and liquid phases was calculated using the equation:

$$TCA = OD_{320} - OD_{278},$$

Where, OD is the optical density calculated as:

$$OD = - \ln(I/I_0) = \mu\rho t,$$

Where I_0 is the incident beam intensity, I is the transmitted beam intensity, μ is the mass absorption coefficient ($cm^2\ g^{-1}$), ρ is the density ($g\ cm^{-3}$) and t is the thickness of the particle (cm). Since TCA depends on the thickness of the particle, it is used as an indicator of the phase state of the particles[4, 5]. We assume each particle as a mixture of elemental carbon (EC), organic carbon (OC), and inorganic component (In). The thickness of OC, In, and EC is calculated from the OD value at pre-edge (320 eV), post-edge (278 eV), and the sp^2 peak (285.4 eV). Further, particles are classified into four classes based on the volume fraction of OC, EC and In as: 1) OC (OC > 96% and (EC + In) < 2%), 2) EC (EC > 96%

and (OC + In) < 2%), 3) OCEC (OC+EC > 2% and In <2%), 4) OCInEC (OC, EC, inorganics >2%).

B.4 Phase state calculation

We divided the organic particles into two categories as 'particles with inclusion' and 'without inclusion'. Using the Scanning Electron Microscopy image of the sample tilted at an angle of 75°, we measured the width and height of each particle using ImageJ software. The width and height of at least 150 particles of each sample were recorded into an excel sheet. Finally, the ratio between width and height was calculated for each particle. The thresholds of aspect ratio for liquid, semi-solid, and solid particles were adopted from a previous study [6].

B.5 High resolution mass spectrometry analysis

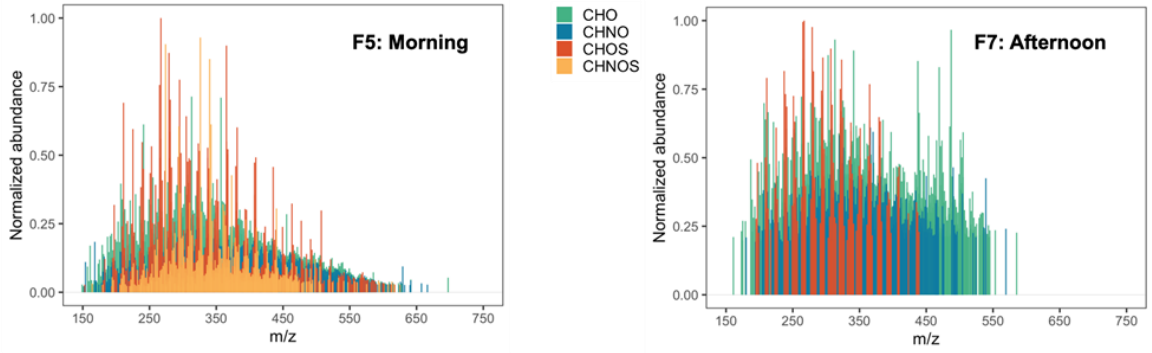

Figure B.5-1: Mass abundance plots for unique molecular features identified in sampling periods: F5 (morning) and F7 (afternoon).

Table B.5-1: Literature reported molecular formulae and their corresponding m/z values for a wide range of Organosulfates and Nitrooxy-Organosulfates

Molecular formula	(m/z) $[M-H]^-$	Study	potential precursors	Sample
$C_{10}H_{15}O_7S^-$	279.0545	Ning et al 2023 [7] Cai et al 2020 [8]	α/β-Pinene, Limonene α/γ-Terpinene	F5, F7
$C_{10}H_{17}O_7S^-$	281.0700		α/β-Pinene, α-	F5, F7

			Terpinene, Limonene, Terpinolene Decalin, Cyclodecane	
$C_{11}H_{17}O_8S^-$	309.0649		n/a	F5, F7
$C_{10}H_{18}NO_9S^-$	328.0707		Limonene	F5
$C_{10}H_{16}NO_7S^-$	294.0653	Cai et al 2020 [8]	α/β-Pinene, α-Terpinene, Terpinolene	F5
$C_{10}H_{19}O_5S^-$	251.0959		Cyclodecane	F5, F7
$C_{10}H_{17}O_5S^-$	249.0802	Cai et al 2020 [8]	α/β-Pinene, Terpinolene Limonene, Cyclodecane	F5, F7
$C_8H_{15}O_4S^-$	207.0697	Cai et al 2020 [8] Wang et al. 2021 [9] Blair et al. 2017 [10]	Diesel vapors	F5
$C_7H_{13}O_5S^-$	209.0489	Cai et al 2020 [8]	Dodecane	F5, F7
$C_9H_{13}O_6S^-$	249.0438	Cai et al 2020 [8]	Terpinolene, Limonene Isoprene	F5, F7
$C_8H_{11}O_7S^-$	251.0231	Cai et al 2020 [8]	Isoprene	F5, F7
$C_8H_{13}O_7S^-$	253.0388	Cai et al 2020 [8]	Isoprene, α-Terpinene	F5, F7
$C_{10}H_{17}O_6S^-$	265.0751	Cai et al 2020 [8]	α-Pinene, Terpinolene, α-Terpinene, Cyclodecane,	F5, F7

			Decalin	
$C_{11}H_{21}O_5S^-$	265.1116	Cai et al 2020 [8]	n/a	F5, F7
$C_9H_{15}O_7S^-$	267.0549	Cai et al 2020 [8]	Limonene, Isoprene	F5, F7
$C_{10}H_{17}O_8S^-$	297.0650	Cai et al 2020 [8]	-Pinene, α-Terpinene Decalin	F5, F7
$C_{10}H_{16}NO_{10}S^-$	342.0499	Cai et al 2020 [8]	α/β-Pinene, α/γ-Terpinene	F5
$C_{12}H_{22}NO_9S^-$	356.1019	Cai et al 2020 [8]	n/a	F5
$C_{12}H_{22}NO_8S^-$	340.1070	Cai et al 2020 [8]	n/a	F5
$C_{10}H_{16}NO_9S^-$	326.0551	Cai et al 2020 [8]	β-Pinene, Limonene, Terpinolene, Decalin	F5
$C_{10}H_{18}NO_8S^-$	312.075844	Cai et al 2020 [8] M Bao 2023 [11]	Limonene, monoterpene	F5

C Copyright documentation

C.1 Permission for Chapter 3

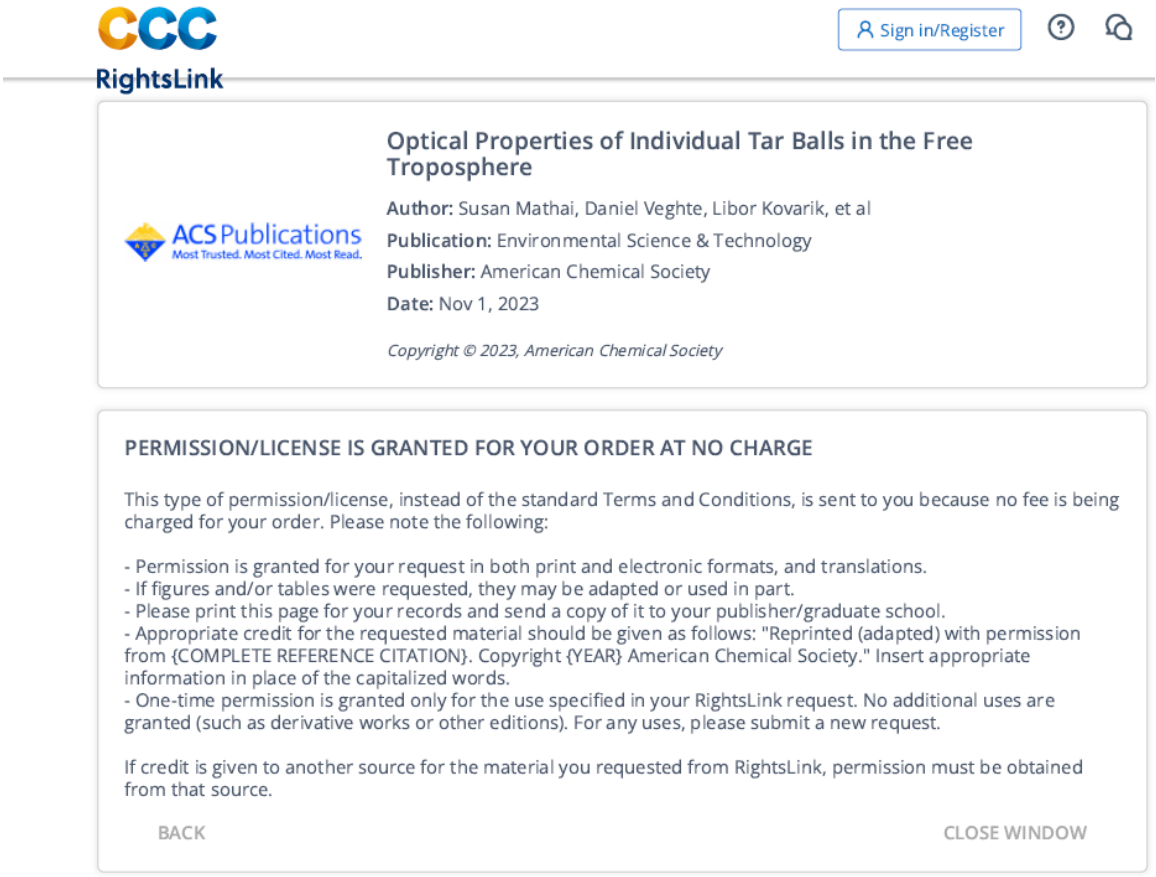

CCC RightsLink

Sign in/Register

Optical Properties of Individual Tar Balls in the Free Troposphere

ACS Publications
Most Trusted. Most Cited. Most Read.

Author: Susan Mathai, Daniel Veghte, Libor Kovarik, et al
Publication: Environmental Science & Technology
Publisher: American Chemical Society
Date: Nov 1, 2023

Copyright © 2023, American Chemical Society

PERMISSION/LICENSE IS GRANTED FOR YOUR ORDER AT NO CHARGE

This type of permission/license, instead of the standard Terms and Conditions, is sent to you because no fee is being charged for your order. Please note the following:

- Permission is granted for your request in both print and electronic formats, and translations.
- If figures and/or tables were requested, they may be adapted or used in part.
- Please print this page for your records and send a copy of it to your publisher/graduate school.
- Appropriate credit for the requested material should be given as follows: "Reprinted (adapted) with permission from {COMPLETE REFERENCE CITATION}. Copyright {YEAR} American Chemical Society." Insert appropriate information in place of the capitalized words.
- One-time permission is granted only for the use specified in your RightsLink request. No additional uses are granted (such as derivative works or other editions). For any uses, please submit a new request.

If credit is given to another source for the material you requested from RightsLink, permission must be obtained from that source.

BACK CLOSE WINDOW

References:

1. Egerton, R. F., *Electron energy-loss spectroscopy in the electron microscope*. Springer Science & Business Media: 2011.
2. Zhu, J.; Crozier, P. A.; Ercius, P.; Anderson, J. R., Derivation of optical properties of carbonaceous aerosols by monochromated electron energy-loss spectroscopy. *Microscopy and Microanalysis* **2014,** *20*, (3), 748-759.
3. Johnson, D.; Spence, J. C. H., Determination of the single-scattering probability distribution from plural-scattering data. *Journal of Physics D: Applied Physics* **1974,** *7*, (6), 771.
4. O'Brien, R. E.; Neu, A.; Epstein, S. A.; MacMillan, A. C.; Wang, B.; Kelly, S. T.; Nizkorodov, S. A.; Laskin, A.; Moffet, R. C.; Gilles, M. K., Physical properties of ambient and laboratory-generated secondary organic aerosol. *Geophysical Research Letters* **2014,** *41*, (12), 4347-4353.
5. Tomlin, J. M.; Jankowski, K. A.; Rivera-Adorno, F. A.; Fraund, M.; China, S.; Stirm, B. H.; Kaeser, R.; Eakins, G. S.; Moffet, R. C.; Shepson, P. B., Chemical imaging of fine mode atmospheric particles collected from a research aircraft over agricultural fields. *ACS Earth and Space Chemistry* **2020,** *4*, (11), 2171-2184.
6. Cheng, Z.; Sharma, N.; Tseng, K.-P.; Kovarik, L.; China, S., Direct observation and assessment of phase states of ambient and lab-generated sub-micron particles upon humidification. *RSC advances* **2021,** *11*, (25), 15264-15272.
7. Ning, C.; Gao, Y.; Zhang, H.; Yu, H.; Cao, R.; Chen, J., Urban particulate water-soluble organic matter in winter: Size-resolved molecular characterization, role of the S-containing compounds on haze formation. *Science of The Total Environment* **2023,** *875*, 162657.
8. Cai, D.; Wang, X.; Chen, J.; Li, X., Molecular characterization of organosulfates in highly polluted atmosphere using ultra-high-resolution mass spectrometry. *Journal of Geophysical Research: Atmospheres* **2020,** *125*, (8), e2019JD032253.
9. Wang, Y.; Zhao, Y.; Wang, Y.; Yu, J.-Z.; Shao, J.; Liu, P.; Zhu, W.; Cheng, Z.; Li, Z.; Yan, N., Organosulfates in atmospheric aerosols in Shanghai, China: seasonal and interannual variability, origin, and formation mechanisms. *Atmospheric Chemistry and Physics* **2021,** *21*, (4), 2959-2980.
10. Blair, S. L.; MacMillan, A. C.; Drozd, G. T.; Goldstein, A. H.; Chu, R. K.; Paša-Tolić, L.; Shaw, J. B.; Tolić, N.; Lin, P.; Laskin, J., Molecular characterization of organosulfur compounds in biodiesel and diesel fuel secondary organic aerosol. *Environmental Science & Technology* **2017,** *51*, (1), 119-127.
11. Bao, M.; Zhang, Y. L.; Cao, F.; Hong, Y.; Lin, Y. C.; Yu, M.; Jiang, H.; Cheng, Z.; Xu, R.; Yang, X., Impact of fossil and non-fossil fuel sources on the molecular compositions of water-soluble humic-like substances in PM2.5 at a suburban site of Yangtze River Delta, China. *Atmos. Chem. Phys.* **2023,** *23*, (14), 8305-8324.